Advanced metrology for few-cycle mid-IR pulses

Ph.D. Thesis

Author

Máté Kurucz

Supervisor

Dr. Bálint Kiss
Research fellow
ELI-ALPS Laser Research Institute

Advisor

Prof. Eric Cormier
Professor
Laboratoire Photonique, Numérique et Nanosciences
Université de Bordeaux

Doctoral School of Physics
Department of Optics and Quantum Electronics
Faculty of Science and Informatics
University of Szeged
Szeged

2021

Table of contents

Acronyms

AGS silver thiogallate

AGSe silver selenogallate

AOPDF acousto-optical programmable dispersive filters

AR anti-reflection

ARR-PCF antiresonant-guiding photonic crystal fiber

BBO beta barium borate

CPA chirped pulse amplification

CW continuous wave

CEO carrier-envelope offset

CEP carrier-envelope phase

DFG difference frequency generation

DFT dispersive Fourier transform

EM electromagnetic

FPGA field-programmable gate array

FROG frequency-resolved optical gating

FT Fourier transform

FTIR Fourier transform infrared spectroscopy

FTL Fourier transform limit

FFT fast Fourier transform

FWHM full width at half maximum

GDD group delay dispersion

GV group velocity

GVD group velocity dispersion

HHG high harmonic generation

IFFT inverse fast Fourier transform

IR infrared

IPN integrated phase noise

KTP potassium titanyl phosphate

LN lithium niobate

LWIR long-wavelength infrared

mid-IR mid-infrared

near-IR near infrared

NOPA noncollinear optical parametric amplification

OP orientation-patterned

OPA optical parametric amplifier

OPCPA optical parametric chirped pulse amplification

OPO optical parametric oscillator

OR optical rectification

OSA optical spectrum analyzer

PPLN periodically-poled lithium niobate

PSD power spectral density

PP periodically poled

QPM quasi-phase-matching

RMS root mean square

SCG supercontinuum generation

SFG sum frequency generation

SH second harmonic

SHG second harmonic generation

SH-SRI second harmonic assisted spectrally resolved interferometry

SPM self-phase modulation

SRI spectrally resolved interferometry

STOD specific third order dispersion

SWIR short-wavelength infrared

TOD third order dispersion

TOUCAN temporal dispersion based one-shot ultrafast carrier envelope phase analysis

UV ultraviolet

VIS visible

WLC white-light continuum

YAG yttrium aluminum garnet

ZDWL zero-dispersion wavelength

ZGP zinc germanium phosphide

I. Introduction and goals

In recent decades, we have been witnessing the rapid development of mid-IR laser sources. This revolution has been fueled by the numerous applications for mid-IR radiation such as strong-field physics in solid-state media [1], time-resolved spectroscopy [2], remote sensing [3,4], just to name a few. One of the promising applications for high intensity mid-IR pulses is attosecond science [5]. Attosecond pulse generation is based on high-harmonic generation (HHG) driven by a few-cycle driving laser pulse. HHG is a strongly nonlinear process during which a target is ionized by an intense laser pulse, generating free electrons. Due to the sign change of the oscillating optical electric field, the returning electron recombines with the parent ion generating harmonic radiation. The maximum achievable photon energy depends on the ponderomotive energy, the quiver energy of the ionized electron in the laser field, which scales quadratically with the driving wavelength [6]. As a results, a high wavelength driving laser can produce a broader HHG spectrum, which allows for the generation of even shorter attosecond pulses [7,8]. However, high harmonic generation efficiency falls drastically with increasing wavelength [8]. To generate a broad HHG spectrum with sufficient yield, few-cycle, high energy, CEP stable mid-IR systems are required.

Today, the most common solid state lasers use neodymium (Nb^{3+}), ytterbium (Yb^{3+}), or titanium (Ti^{3+}) dopants, emitting in the near infrared wavelength range. Femtosecond mid-IR lasers started to appear only at the turn of the century. Common laser components such as dispersive mirrors, high-reflective coatings, acousto-optic modulators, etc. have less favorable parameters compared to their near-IR counterparts. They are also more expensive, and are manufactured only by a few companies. Another issue is that the assortment of detection and diagnostic devices for mid-infrared lasers is also limited. The aforementioned near-IR femtosecond lasers can use detection technologies based on silicon, the most common material in the semiconductor industry. However, silicon is not suitable for mid-infrared detection, so InAsSb, or HgCdTe compounds are used as base materials for semiconductor detectors, which generally increases production costs. Furthermore, detector arrays or cameras for mid-infrared radiation are prohibitively expensive. For this reason, a large number of diagnostic tools for femtosecond mid-infrared lasers utilize workaround methods. As part of my research, my aim was to expand the palette of these diagnostic tools and develop cost-effective simple methods for the mid-IR spectral region.

In my dissertation I mainly focus on ultrafast (fs $=10^{-15}$ s) optical processes in the mid-IR spectral region. In Chapter II, I detail the scientific background of my research. First I present the wave theory mid-IR laser pulse in Chapter II.1. Then in Chapter II.2 linear optical interactions between light and matter are presented, i.e. light absorption and dispersion. In Chapter II.3 nonlinear optical interactions are detailed, with major emphasis on the SHG and SPM processes, as they serve as the basis for the new scientific methodologies presented in this dissertation. Then in Chapter II.4 interferometry is described with a more detailed analysis of spectrally resolved interferometry (SRI), and second harmonic assisted spectrally resolved interferometry (SH-SRI), because the newly developed dual-band SRI described in Chapter III.2 is based on these methods. In Chapter II.5, carrier envelope metrologies are examined, which gives historical context to the TOUCAN method described in Chapter III.1. I also give an outlook on ultrafast mid-IR laser systems in Chapter II.6.

In Chapter III, I present my own research, showcasing several new techniques developed for ultrafast mid-IR sources. For most of these experiments, the state-of-the-art MIR laser system [9] of ELI-ALPS was used. The laser system provides close to 4-cycle pulses with a central wavelength of around 3.2 μm at 100 kHz repetition rate. The average output power of the laser is 14 W, which means each pulse has 3.3 GW peak power, hence noble gases can be ionized with tight focusing even at atmospheric pressure. The combination of high peak power and long wavelength makes the system uniquely fit for specialized experiments, some of which have already been completed and published in scientific journals [10–13]. This dissertation contains three different techniques and their experimental verification. First, Chapter III.1 presents the TOUCAN method, which is an elegant solution for improving one of the most crucial diagnostic devices for the laser. This method can be used to measure the carrier-envelope phase of the laser shot to shot at 100 kHz, faster than any commercially available technology. The second technique presented in Chapter III.2 is a new spectral phase shift measuring technique for optical components, named dual-band SRI, which is uniquely suited for broadband few-cycle lasers. The main selling point of this method is that it is capable of measurements at two spectral bands simultaneously. Finally, since the dynamics of light-induced atomic interactions heavily depends on the duration of the driving laser pulse, further improvement can be achieved on the MIR laser by the post-compression of the pulses after the last OPA stage, which is presented in Chapter III.3. This way the spectrum can be further broadened and the pulses can be temporally compressed, without the need to decrease the efficiency of the OPA stages. While the technique is well known, it is the first time it was applied for a mid-IR laser source with more than 10 W average power.

The experiments discussed in my dissertation were performed in the laboratories of ELI-ALPS Laser Research Institute (ELI-HU Non-Profit Ltd.). A preliminary experiment was performed for the TOUCAN method at the University of Bordeaux with the supervision of Prof. Eric Cormier. The TIPTOE method (tunneling ionization with a perturbation for the time-domain observation of an electric field) was developed at the Gwangju Institute of Science and Technology, which provided us with a useful reference measurement for the temporal characterization of the post-compressed pulses.

II. Scientific background

II.1. Wave theoretical description of mid-IR laser pulses

In most cases, light can be described as a transverse electromagnetic wave. As such it can be characterized by its wavelength, which can be the basis to assign light to different subcategories. The human eye is only sensitive to a very narrow wavelength region of light – called visible light – between roughly 400 and 700 nm. Longer wavelength light waves are called infrared radiation up to 1 mm, and shorter wavelength light is called ultraviolet up to 10 nm. The infrared region can be subdivided into further categories: near-infrared, mid-infrared, long-wavelength infrared and far infrared. There is no consensus in the scientific community about the boundaries between these regions. To avoid confusion, hereafter I will use the definitions summarized in Table 1.

Division name	Wavelength
Ultraviolet (UV)	0.01–0.4 µm
Visible (VIS)	0.4–0.7 µm
Near-infrared (near-IR)	0.7–1.4 µm
Short-wavelength infrared (SWIR)	1.4–3 µm
Mid-infrared (mid-IR)	3–8 µm
Long-wavelength infrared (LWIR)	8–15 µm
Far infrared (FIR)	15–1000 µm

Table 1. Wavelength divisions of infrared light

Infrared light (IR) was first discovered by William Herschel in the early 19th century [14]. As part of his investigation, he dispersed sunlight into its spectral components with a prism, and discovered an increase in temperature, caused by radiation beyond the visible red part of the spectrum. This scientific breakthrough was quite revolutionary at the time, the discovery of new light that is not visible by the naked eye. There is no doubt that in the past two centuries the concept of infrared light has become "mainstream" thanks to its numerous everyday applications like fiber-optic communication, remote controls, and handheld infrared thermometers. (The latter became especially widespread during the COVID-19 pandemic.)

While there is no fundamental difference between IR light and visible light, there are still many differences when interaction of light with matter is considered. Many molecules transmit visible light, while absorbing specific bands in the IR, which is the basis for Fourier transform infrared spectrometry [15]. The opposite is true for some semiconductor materials that transmit mid-IR radiation unhindered, while absorbing most of the visible. For this reason, many detectors and devices designed for visible light do not function with mid-IR radiation, which can hinder the further development of mid-IR technologies.

II.1.1. The electromagnetic wave

Since the discoveries of Michael Faraday and James Clerk Maxwell, we have known that light is electromagnetic (EM) wave. Based on this theory, we can derive many properties for light and light-matter interaction using a set of partial differential equations called Maxwell equations [16]. The EM field can be represented by two vectors: **E** (electric vector) and **B** (magnetic induction). The bold letters indicate that a quantity is a vector. To describe the effect of the EM field on materials, we have to introduce a second set of vectors: **D** electric displacement, **H** magnetic vector, **J** electric current density, and the scalar property ρ, which stands for charge density. Using these quantities, the Maxwell equations take the following form:

$$\nabla \cdot \mathbf{D} = \rho\,, \tag{II-1}$$

$$\nabla \cdot \mathbf{B} = 0\,, \tag{II-2}$$

$$\nabla \times \mathbf{E} = -\frac{\partial \mathbf{B}}{\partial t}\,, \tag{II-3}$$

$$\nabla \times \mathbf{H} = \mathbf{J} + \frac{\partial \mathbf{D}}{\partial t}\,. \tag{II-4}$$

To uniquely determine the electromagnetic field distribution, additional equations are required. The dynamic responses of material interacting with the EM field can be summarized in the so called material equations (or constitutive relations)

$$\mathbf{D} = \varepsilon \mathbf{E}\,, \tag{II-5}$$

$$\mathbf{B} = \mu \mathbf{H}\,, \tag{II-6}$$

$$\mathbf{J} = \sigma \mathbf{E}\,, \tag{II-7}$$

where, ε called permittivity (dielectric constant), μ is called magnetic permeability, and σ is called specific conductivity. We can rewrite Equations (II-5) and (II-6) to emphasize that the internal field of the material is generated not only by the outside EM field, but also by the polarization and magnetization in the atoms and molecules. This will result in equations

$$\mathbf{D} = \varepsilon \mathbf{E} = \varepsilon_0 \mathbf{E} + \mathbf{P}\,, \tag{II-8}$$

$$\mathbf{B} = \mu \mathbf{H} = \mu_0 \mathbf{H} + \mathbf{M}\,, \tag{II-9}$$

where **P** is the polarization vector and **M** is the magnetization vector, while ε_0, and μ_0 are the permittivity and permeability of free space. In free space, where no material is present, the **P** and **M** vectors are equal to the **0** vector. In this case the ε and μ quantities become ε_0 and μ_0, respectively.

To solve these equations, first we make simplifying assumptions. The medium of the material is uniform and isotropic, which means that permittivity and permeability do not depend on the position or direction of propagation. Furthermore, let us assume that the material is non-conducting (**J**=0) and free from charge (ρ=0). Based on these assumption, we can use the simplified Maxwell equations:

$$\nabla \times (\nabla \times \mathbf{E}) = \nabla \times \left(-\frac{\partial \mathbf{B}}{\partial t}\right) = -\frac{\partial (\nabla \times \mathbf{B})}{\partial t} = -\frac{\partial}{\partial t}\left(\varepsilon \mu \frac{\partial \mathbf{E}}{\partial t}\right). \tag{II-10}$$

We can use a vector algebra to rewrite the curl of a curl of a vector field and simplify the left side of equation (II-10). This results in equation

$$\nabla \times (\nabla \times \mathbf{E}) = \nabla \times (\nabla \cdot \mathbf{E}) - \nabla^2 \mathbf{E} = \nabla^2 \mathbf{E} = -\frac{\partial}{\partial t}\left(\varepsilon\mu \frac{\partial \mathbf{E}}{\partial t}\right). \tag{II-11}$$

Furthermore, if we assume that the material's permittivity and permeability are not time dependent (no dispersion occurs), further simplifications can be made to Equation (II-11):

$$\nabla^2 \mathbf{E} = -\varepsilon\mu \frac{\partial^2 \mathbf{E}}{\partial t^2}. \tag{II-12}$$

This is the wave equation. As the divergence of the electric field is zero, only transverse waves are solution to the Equation (II-12). The simplest solution for this differential equation is the monochromatic plane wave with ω angular frequency traveling in the direction of the **k** wavenumber vector. We can express this in in the following way:

$$\mathbf{E}(t, \mathbf{r}) = \mathbf{E}_0 \cos(\omega t - \mathbf{k} \cdot \mathbf{r} + \varphi), \tag{II-13}$$

where **r** is the position vector, and φ is the temporal phase. Even though the electric field is a real quantity, it is generally more convenient to use complex representation [17], where the real part is equal to Equation (II-13)

$$\mathbf{E}(t, \mathbf{r}) = \mathbf{E}_0 e^{i(\omega t - \mathbf{k}\cdot\mathbf{r} + \varphi)}. \tag{II-14}$$

The velocity of the traveling wave can be calculated from permittivity and permeability

$$v = \frac{\omega}{|\mathbf{k}|} = \frac{1}{\sqrt{\varepsilon\mu}}. \tag{II-15}$$

When light propagates through vacuum, the velocity of the traveling wave reaches its maximum, the speed of light, and permittivity and permeability are reduced to the permittivity and permeability of free space

$$c = \frac{1}{\sqrt{\varepsilon_0 \mu_0}}. \tag{II-16}$$

The slowdown, when light travels through a medium, can be expressed by the refractive index, which is the ratio between the speed of the traveling EM wave in a medium compared to the speed of the EM wave traveling in vacuum

$$n = \frac{c}{v} = \sqrt{\frac{\varepsilon\mu}{\varepsilon_0 \mu_0}}. \tag{II-17}$$

The electric field vector can be expressed in the Descartes coordinate system

$$\mathbf{E}(t, \mathbf{r}) = E_x(t, \mathbf{r}) + E_y(t, \mathbf{r}) + E_z(t, \mathbf{r}). \tag{II-18}$$

Hereafter we will assume that the light wave is linearly polarized, and only one component remains in a properly chosen coordinate system. The wave equation for the scalar electric field is called scalar wave equation, and it can be expressed with the Laplace operator as follows

$$\Delta E = -\varepsilon\mu \frac{\partial^2 E}{\partial t^2}. \tag{II-19}$$

The solution for this is called the scalar wave equation, and it is quite similar to Equation (II-14)

$$E(t, \mathbf{r}) = E_0 e^{i(\omega t - \mathbf{k}\cdot\mathbf{r} + \varphi)}, \tag{II-20}$$

where the real part of this equation is equal to the scalar electric field strength.

II.1.2. Optical pulse

Let us now consider a non-monochromatic solution to the wave equation. In all cases we can express the solution as the superposition of an infinite number of monochromatic waves with different frequencies, based on the Fourier integral theorem. Let us ignore the spatial dimension and formulate the relation as a purely time domain function

$$E(t) = \int_0^\infty A(f)e^{i(2\pi ft + \varphi(f))}df, \tag{II-21}$$

where f stands for frequency, which is equal to ω angular frequency divided by 2π. A(f) is the spectral amplitude function, and φ(f) is the spectral phase of the monochromatic components. As f frequency can only be positive, we can extend the integration to the negative infinity, as it will have zero contribution to the overall integral. The advantage of this mathematical feat is that the result can be interpreted as an inverse Fourier transform [18]

$$E(t) = \int_{-\infty}^{\infty} A(f)e^{2\pi ift}e^{i\varphi(f)}df = \mathcal{F}^{-1}\{A(f)e^{i\varphi(f)}\}(t)\,. \tag{II-22}$$

The resulting complex electric field can be transformed back to acquire the electric field as the function of frequency

$$E(f) = \mathcal{F}\{E(t)\}(f) = A(f)e^{i\varphi(f)}\,. \tag{II-23}$$

Spectral and temporal intensities can be determined by multiplying the complex electric field with its complex conjugate to obtain a real quantity and multiplying it by some physical constants derived from the Poynting theorem of electrodynamics [17]

$$I(f) = 2n\varepsilon_0 c\left(E(f)\overline{E(f)}\right) = 2n\varepsilon_0 c|E(f)|^2\,, \tag{II-24}$$

$$I(t) = 2n\varepsilon_0 c\left(E(t)\overline{E(t)}\right) = 2n\varepsilon_0 c|E(t)|^2\,, \tag{II-25}$$

where the vinculum above the electric field stands for its complex conjugation, and the unit of intensity is W/m^2 or W/cm^2. Unfortunately, this is a one-way operation as the real value intensity function does not contain any information about the phase. For this reason, it is not straightforward to determine the phase of the electric field as most detection techniques are only sensitive to the intensity of the field. The relations between the electric field and the intensity in the spectral and temporal domains are summarized in Fig. 1.

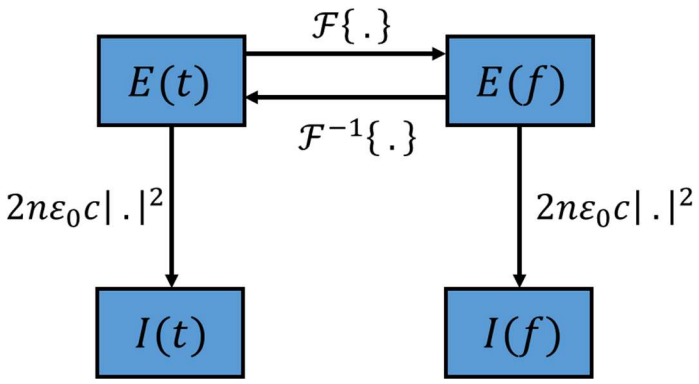

Fig. 1. The relationship between the complex electric field and intensity in the frequency and time domains.

These monochromatic waves can constructively and destructively interfere, meaning they can strengthen or extinguish each other at different moments in time, depending on their relative difference in phase and polarization, which process is detailed in Chapter II.4. If the constructive interference is localized to a temporal region we call the result a wave packet, or in other words, an optical pulse. The electric field of an optical pulse can be separated into two parts: its envelope where the electromagnetic energy is localized and its carrier wave with an angular central frequency of ω_0. We can express the temporal evolution of the electric field as

$$E(t) = A(t) \cdot \cos(\omega_0 t + \varphi(t) + \varphi_{CE}), \tag{II-26}$$

where $\varphi(t)$ is the temporal phase and φ_{CE} is the carrier envelope phase or CEP for short. The CEP is the phase difference between the global maximum of the envelope and the carrier wave. When the optical pulse contains only a few cycles, the CEP value significantly determines the shape of the pulse, displayed in Fig. 2, and consequently, the outcome of extreme nonlinear optical processes. Therefore, monitoring the time evolution of the CEP and the CEP stabilization of the laser system is essential in these experiments, which will be described in Chapter II.5.

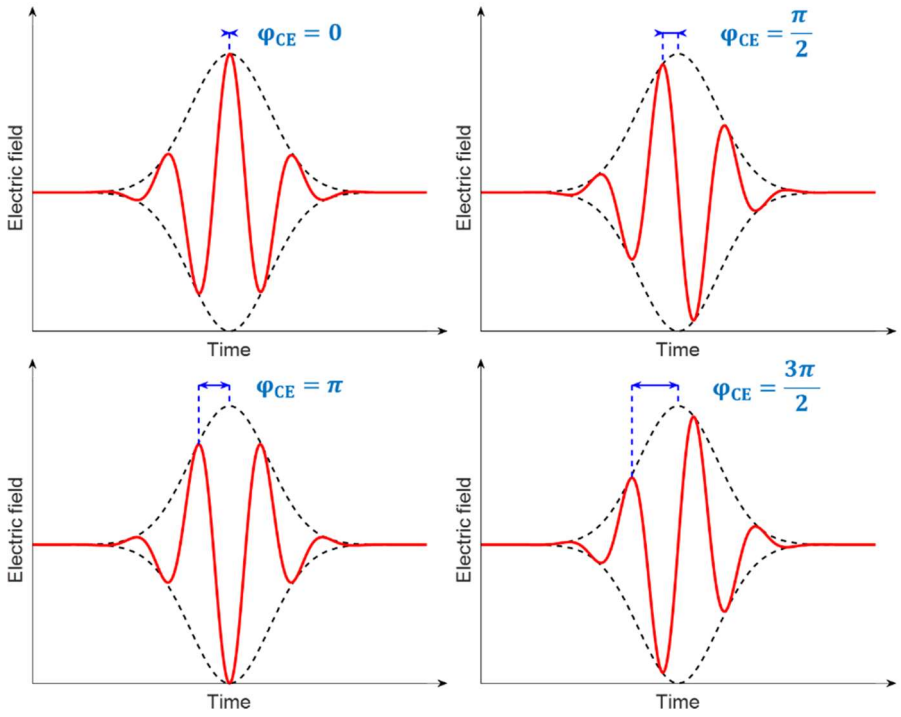

Fig. 2. The electric field (solid) and its envelope (dashed) vs time. All the pulses have different CEP values (displayed in blue).

Optical pulses are most often generated through Q-switching and mode-locking [19]. In these processes, the generated pulses follow one another at equal distances, and are called a pulse train. A laser system producing a pulse train can be characterized by its repetition rate, or in other words, by the number of pulses it generates during one second of operation, measured in Hz. A fixed repetition rate, mode-locked laser emits a pulse train where the spectrum consists of almost monochromatic waves with equidistantly spaced frequencies, called frequency comb. While the intensity of these components can vary, their spacing is equal to the repetition rate frequency of the laser. The frequency of the monochromatic wave components can be written as

$$f = f_{CEO} + nf_{rep}\,, \tag{II-27}$$

where f_n is the n^{th} frequency component, f_{rep} is the repetition rate, and f_{CEO} is the carrier-envelope offset frequency [20]. For every pulse in this pulse train the CEP can have a different value, and this pulse-to-pulse CEP change is directly related to the carrier-envelope offset frequency

$$f_{CEO} = \frac{\Delta\varphi_{CE} \bmod 2\pi}{2\pi} f_{rep}\,. \tag{II-28}$$

This carrier-envelope offset frequency can also be measured and even stabilized, as described in Chapter II.5.1, but for a CEO frequency stabilized laser the CEP will still change from pulse to pulse with a constant amount.

There are further important laser parameters one can derive from the description of a laser pulse shown in Equation (II-26). The central angular frequency of the carrier wave can be defined as the weighted average of the monochromatic frequencies, where the weight is the spectral intensity distribution

$$\omega_0 = \frac{\int_0^\infty \omega \cdot |A(\omega)|^2 \mathrm{d}\omega}{\int_0^\infty |A(\omega)|^2 \mathrm{d}\omega}\,. \tag{II-29}$$

All the energy contained in a single optical pulse, called pulse energy, can be determined from the intensity of its electric field. To present this relation, once again spatial dimension must be included. Let us consider a plane wave with spatial dimensions x and y, which are perpendicular to the propagation direction of the wave, following common convention [21]

$$\text{Energy} = \iiint_{-\infty}^{\infty} I(x,y,t)\,\mathrm{dx}\,\mathrm{dy}\,\mathrm{dt} = \iiint_{-\infty}^{\infty} I(x,y,f)\,\mathrm{dx}\,\mathrm{dy}\,\mathrm{df}\,. \tag{II-30}$$

As the equation states, energy can also be calculated from the time and frequency domain integral. We can define the instantaneous pulse power too as

$$P(t) = \iint_{-\infty}^{\infty} I(x,y,t)\,\mathrm{dx}\,\mathrm{dy}\,. \tag{II-31}$$

There are many definitions for pulse duration, but here we will use the most common one: FWHM pulse duration, which is the full width at half maximum of the instantaneous pulse power. Furthermore, we can define two quantities for the pulse train: the average power, which is the time average of the instantaneous pulse power during a period much longer than that of the pulse train. This quantity equals the pulse energy multiplied the repetition rate. The other quantity is peak power, which is the global maximum of the instantaneous pulse power. Even at a relatively low average power the peak power for ultrashort pulses can even reach PW (10^{15} W) level [22], which is a great advantage in comparison to continuously operating lasers. The shorter the pulse duration for the same pulse energy, the higher the increase in peak power. If the pulse duration is sufficiently short, it can be characterized by the number of cycles in the electric field. We can calculate this by multiplying the pulse duration by the central frequency of the pulse

$$N_{cycles} = \frac{\omega_0 \tau_{FWHM}}{2\pi}\,. \tag{II-32}$$

II.2. Linear propagation of light

I have shown in Equation (II-17) that the speed of the EM wave traveling through material is the speed of light divided by the refractive index of the material. The refractive index is not only material dependent; it also depends on the frequency, intensity of the EM wave. The intensity dependence will be discussed in Chapter II.3. In this chapter we disregard the spatial inhomogeneity of materials and the intensity dependence of the refractive index, and only focus on frequency dependence. The frequency dependence of the refractive index results in different frequency components of an optical pulse traveling at different velocities, which causes the dispersion of the pulse. During light propagation not only dispersion can occur but also absorption, which is also dependent on the frequency of the EM wave. Frequency dependent dispersion and the absorption functions are deeply intertwined. Based on the Kramers–Kronig relations, the refractive index spectrum can be calculated if the entire absorption spectrum is known, or vice versa [23]. These functions can be used to characterize light propagation in a medium at low optical intensities.

II.2.1. Material absorption

Photons are the smallest undividable quanta of the electromagnetic field, and they can be absorbed by the medium as they propagate through it. In this case, the photon energy transforms into the internal energy of the medium material. The energy of one photon can be calculated from its frequency based on the formula [21]

$$E = hf = \frac{hc}{\lambda}, \tag{II-33}$$

where f is the frequency of the photon; λ is the wavelength of the photon; h is the Planck constant equal to $6.62607015 \cdot 10^{-34}$ J·s. Photon energy is usually given in units of eV (1 eV = $1.602 \cdot 10^{-19}$ J). The absorption of a single photon is a stochastic process, but for an optical pulse containing a large number of photons, the pulse energy attenuates deterministically as it propagates through the medium. The absorption of photons can originate from a large number of diverse physical and chemical processes characteristic of the absorbing material's structure and composition [24]. These absorption sources have a characteristic resonance frequency, and absorption increases as the frequency of light approaches this frequency. The possible sources of solid-state material absorption are plotted as the function of photon energy and the corresponding photon wavelength in Fig. 3.

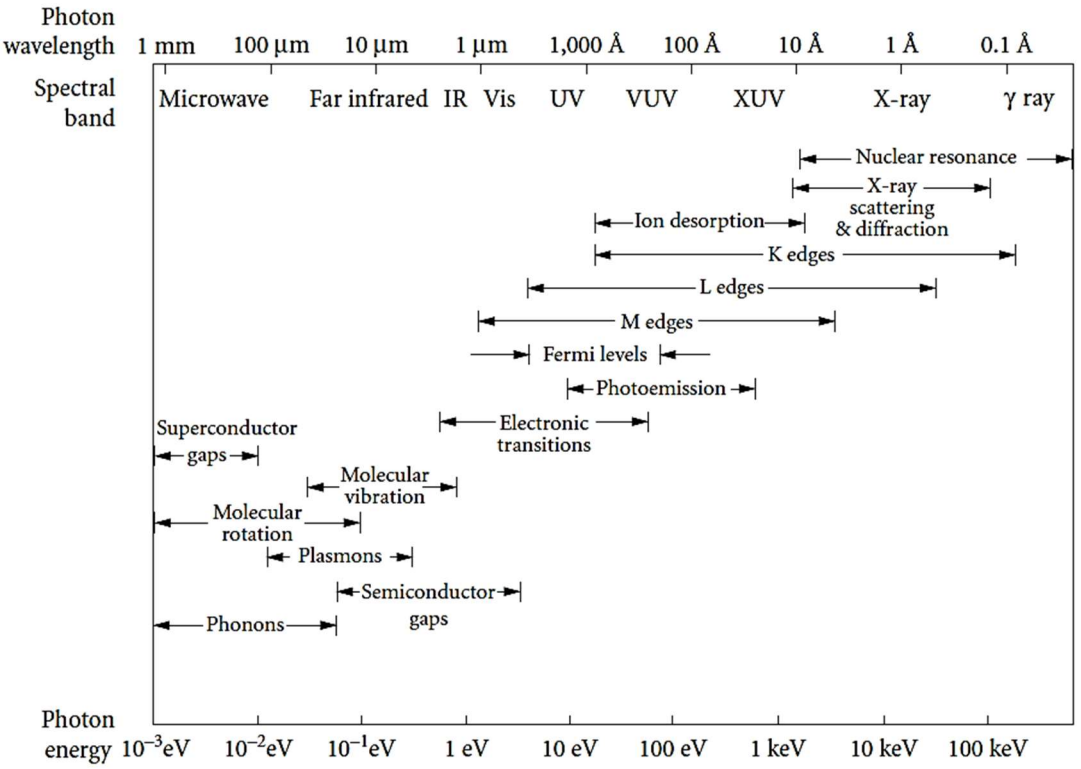

Fig. 3. The electromagnetic spectrum and material absorption bands separated by underlying physical phenomena as a function of photon energy [24]

We can add up all the absorption sources to create an effective absorption spectrum, which shows the probability of the absorption of a photon based on its frequency. This way we can observe which materials transmit at certain frequency regions. This picture can help us identify materials that transmit in the mid-IR, where everyday intuitions about transparent materials no longer apply. First let us investigate single electron transitions, one of the main contributors to absorption in the VIS and IR spectral regions [24]. Quantum theory predicts that an electron can only have discrete energy levels [25]. These electron energy levels in a solid-state material form energy bands, any other energy state is forbidden for electrons to occupy. The average level to which the energy bands are filled with electrons is called the Fermi level, and it can be located in the forbidden band. The highest energy band below the Fermi level is called the valence band, and the lowest energy band above the Fermi level is called conduction band. This band structure can be used to differentiate and categorize materials. When the conduction and valence bands overlap, we call the material metal, while in nonmetallic solids these bands are separated by a forbidden band. The energy difference between the bottom of the conduction band and the top of the valence band is called bandgap, and it is also measured in eV. Materials with a small band gap are called semiconductors (e.g. < 4 eV), while materials with large band gaps are called dielectrics or insulators (e.g. > 4 eV). However, this distinction is arbitrary, as there is no clear boundary between them. The band structure of solid state materials is displayed in Fig. 4.

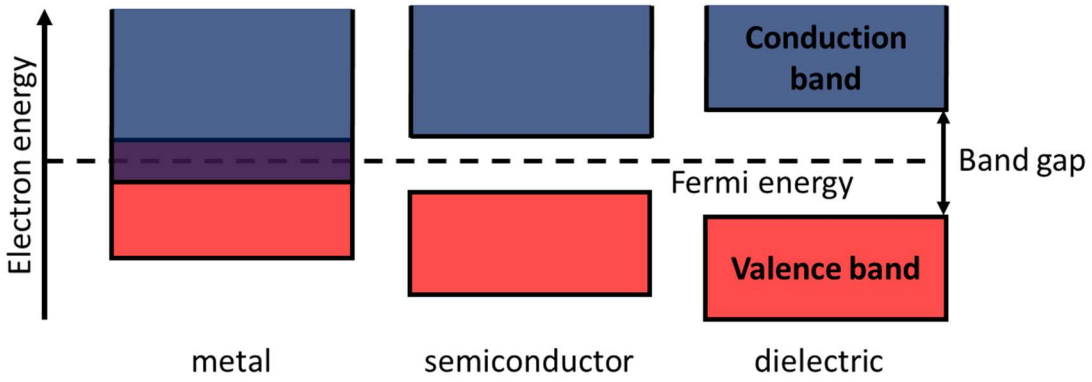

Fig. 4. The energy-band structure of solid state materials

Bandgap energy is also the minimum energy required to excite an electron from the valence band to occupy an electron vacancy in the conduction band. This means that photons can only be absorbed if they possess lower wavelengths than $hc/E_{band\ gap}$. For this reason, the narrower the band gap the longer the wavelength where the material transmits light. For semiconductors with a band gap less than 1.57 eV this cutoff wavelength lies outside the VIS spectral region, in the IR spectral range. Two notable examples for such semiconductors are silicon (Si) and germanium (Ge). Si has an indirect band gap of 1.12 eV (1.1 µm) [26] and germanium has an indirect band gap of 0.796 eV (1.55 µm) [26], which means they absorb VIS light but transmit mid-IR radiation.

On the other hand, the bandgap of dielectrics is higher than 4 eV, which means that their cutoff wavelengths are smaller, so absorption in the mid-IR can only be associated with other physical processes. Dielectrics can be further separated into two categories: glasses and crystals. Most glasses contain molecules with an OH group, as a byproduct of glass melting [27]. The OH group's absorption band is around 3 µm, which makes these glasses unsuitable for mid-IR application. The development of glass manufacturing has led to the appearance of new types of glass, which can transmit mid-IR light, like fluorides, tellurites, and chalcogenides glasses.

On the other hand, there are quite a few dielectric crystals which can transmit in the IR region. Out of these we have to mention fluoride crystals: CaF_2, BaF_2, MgF_2, LiF. They possess very broad bandgaps, so they can be used for IR, VIS and UV applications as well. Sapphire also transmits IR up to 5 µm, and because of its hardness and good thermal conductivity it is often employed as a laser crystal host (e.g.: Ti:sapphire). The YAG crystal is transparent up to 5 µm, and it is commonly used in nonlinear optics in the VIS and IR ranges. Most of these crystals are isotropic, which means that they refract light regardless of polarization. Notable exceptions are the uniaxial MgF_2 and sapphire crystals.

Gases possess no bandgap structure, and absorption stems from rotation-vibration transitions and ionization. When gas is ionized, it loses electrons from the outermost orbital of their atoms. These ionization potentials are generally high: 12 eV (103 nm) in case of oxygen, and 15.6 eV (79 nm) in case of nitrogen, both of which lie within the UV region. This means that single photon ionization cannot occur for VIS and IR light; a single photon can only be absorbed through the rotation-vibration transitions of molecules. Air mostly consists of nitrogen and oxygen molecules (99%), but there are other molecules at much lower concentrations, such as noble gases (Ar, Ne…), CO_2, and water vapor. Noble gases do not form molecules in the air, which means they do not possess rotation-vibration transitions. On the other hand, CO_2 and

water molecules have characteristic absorption lines in the infrared spectral region, which is the reason for their contribution to the greenhouse effect [28]. There are some wavelength ranges in the IR – called infrared atmospheric windows – where there is no atmospheric absorption. Such windows can be found between 2.7 μm and 4.3 μm and between 8 μm and 14 μm, respectively. Lasers emitting in these wavelength ranges are free from linear absorptions of the air, although nonlinear absorption through multi-photon ionization can still occur at high optical intensities.

II.2.2. Material dispersion

Dispersion is a phenomenon that occurs when different frequency light waves propagate at different velocities. For ultrashort pulses the effect of dispersion can be quite significant, as it can alter the temporal shape. In the spectral domain dispersion only changes the spectral phase of a propagating pulse without affecting the spectral intensity, but in the temporal domain both the amplitude and phase will change. It is useful to expand the phase into a Taylor series around ω_0 central angular frequency [23], as we will see that different components of the series affect the optical pulse differently. The first derivative of the spectral phase around ω_0 is called group delay (GD)

$$\mathrm{GD} = \left(\frac{\mathrm{d}\varphi(\omega)}{\mathrm{d}\omega}\right)_{\omega=\omega_0}. \tag{II-34}$$

The second order derivative of the phase is called group delay dispersion (GDD)

$$\mathrm{GDD} = \left(\frac{\mathrm{d}^2\varphi(\omega)}{\mathrm{d}\omega^2}\right)_{\omega=\omega_0}. \tag{II-35}$$

The third order derivative of the phase is called third order dispersion (TOD)

$$\mathrm{TOD} = \left(\frac{\mathrm{d}^3\varphi(\omega)}{\mathrm{d}\omega^3}\right)_{\omega=\omega_0}. \tag{II-36}$$

The fourth order derivative of the phase is called fourth order dispersion (FOD)

$$\mathrm{FOD} = \left(\frac{\mathrm{d}^4\varphi(\omega)}{\mathrm{d}\omega^4}\right)_{\omega=\omega_0}. \tag{II-37}$$

Further derivation yields even higher order phase derivatives, which in most cases can be ignored. Now we can use these derivative values to express the Taylor expansion of the spectral phase around ω_0 and arrive at the expression of

$$\varphi(\omega) = \varphi(\omega_0) + \mathrm{GD}\cdot(\omega_0-\omega) + \frac{1}{2}\mathrm{GDD}\cdot(\omega_0-\omega)^2 + \\ + \frac{1}{6}\mathrm{TOD}\cdot(\omega_0-\omega)^3 + \frac{1}{24}\mathrm{FOD}\cdot(\omega_0-\omega)^4 \ldots \tag{II-38}$$

The first two components are the constant and the linear phases. Constant phase does not affect the temporal shape, while the linear phase, i.e. group delay only delays it in time. When a pulse propagates in vacuum, the added spectral phase is linear, meaning that higher order phase derivatives do not change. When the second and higher order derivatives are zero, the corresponding pulse duration will be the shortest for any given spectral intensity distribution. Such an optical pulse with only constant and linear spectral phase terms is called Fourier transform limited (FTL). The FTL pulse duration can be calculated from the spectrum using

Fourier transform, as it describes a hypothetic pulse duration of a pulse with the given spectrum, which has only constant and linear phase terms. FTL values for a given spectrum can be calculated using the following formula

$$PD_{FTL} = FWHM\left(\left|FFT\left(\sqrt{I_n(f)}\right)\right|^2\right), \tag{II-39}$$

where FFT stands for fast Fourier transform, I_n is the spectral distribution, and PD_{FTL} is the FTL pulse duration. Second and higher order phase derivatives modify the temporal shape of the pulse, by stretching it and decreasing the peak power. The effect of the phase derivatives on an optical pulse is visualized in Fig. 5.

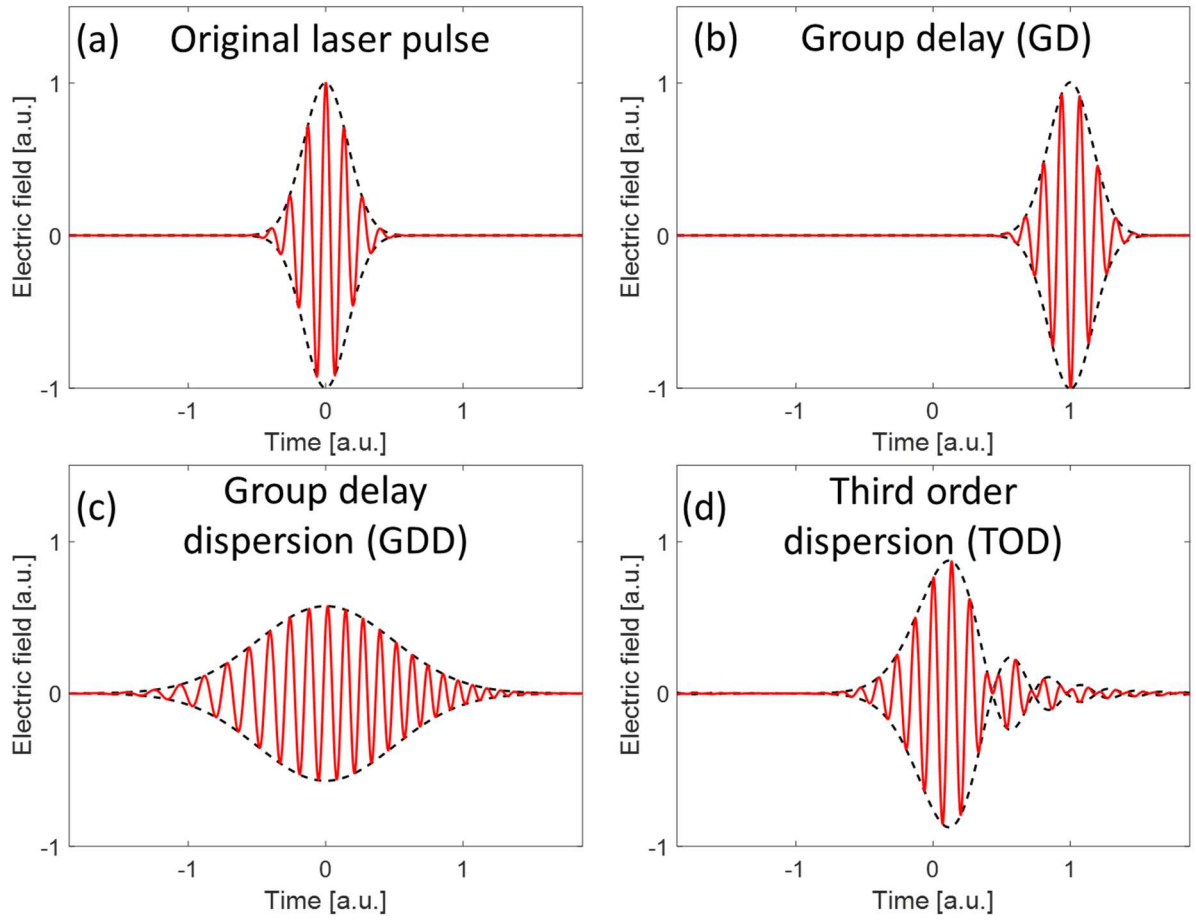

Fig. 5. The effect of spectral phase derivatives on the laser pulse. (a) The temporal evolution of the electric field of the original laser pulse without any dispersion effect. (b) The effect of GD on the original pulse is displayed, showing the pulse temporally delayed. (c) The pulse is stretched in time by GDD and the chirp effect can also be observed. (d) TOD affects the pulse in a way that pre- or post-pulses emerge next to the main pulse.

When light propagates through any material, dispersion effects will manifest, altering the spectral phase. If we assume that the material is homogenous, the spectral phase shift between the entering and exiting beams can be written as follows

$$\varphi(\omega) = d \cdot k(\omega) = \frac{d \cdot n(\omega) \cdot \omega}{c}, \tag{II-40}$$

where d is the thickness of the material, ω is the angular frequency, k is the angular frequency dependent wavenumber, c is the speed of light, and n is the refractive index dependent on the angular frequency. As the spectral phase shift relates to thickness linearly, it is useful to

introduce material dispersion parameters, which are independent from material thickness. This can be achieved by simply dividing the phase derivatives with the thickness. For the first three phase derivatives the following metrics can be introduced

$$\frac{1}{\mathrm{GV}} = \frac{\mathrm{GD}}{\mathrm{d}} = \frac{\partial \mathrm{k}(\omega)}{\partial \omega}, \tag{II-41}$$

$$\mathrm{GVD} = \frac{\mathrm{GDD}}{\mathrm{d}} = \frac{\partial^2 \mathrm{k}(\omega)}{\partial \omega^2}, \tag{II-42}$$

$$\mathrm{STOD} = \frac{\mathrm{TOD}}{\mathrm{d}} = \frac{\partial^3 \mathrm{k}(\omega)}{\partial \omega^3}, \tag{II-43),}$$

where GV is called group velocity, GVD is group velocity dispersion and STOD is the specific third order dispersion.

All dispersion parameters can be calculated using the numerical derivation of the measured refractive index spectrum. Unfortunately, raw measurement data of the refractive index usually have small measurement errors, but these deviations become significant when high order derivatives are calculated. To circumvent this issue, the semi-empirical Sellmeier formula is often employed to create a fit function for the measured refractive index spectrum. The Sellmeier formula expresses the square of the refractive index as follows:

$$\mathrm{n}^2(\lambda) = \mathrm{A} + \sum_\mathrm{i} \frac{\mathrm{B_i}\lambda^2}{\lambda^2 - \mathrm{C_i}}, \tag{II-44}$$

where λ is the wavelength and A, B_i, C_i are positive real coefficients of the Sellmeier equation. The C_i coefficients are squares of the absorption resonance wavelengths [23]. At $\lambda^2=C_i$, absorption reaches the maximum and the refractive index function becomes a singularity. The closest the wavelengths are to these singularities the larger the effect they have on the refractive index. In practice, only the closest 2 to 4 singularities affect the refractive index, all other components can be neglected as their contribution is minimal. For the refractive indices of VIS and near-IR transmitting materials these singularities usually stem from UV, LWIR and FIR absorptions. Let us take BK7 borosilicate glass [29] as an example, transmitting in the visible and near-IR. The C_i coefficients of the Sellmeier equation of this material are the following: $C_1 = 6.00 \cdot 10^{-3}$ μm^2; $C_2 = 2.00 \cdot 10^{-2}$ μm^2; $C_3 = 103.56$ μm^2, which corresponds to absorptions at 77.46 nm, 141.48 nm and 10176.5 nm, respectively. The value of GVD monotonously decreases between singularities with the increase of wavelength. Usually there exists a wavelength, where the sign of the GVD flips. This wavelength, where the GVD equals zero, is called the zero-dispersion wavelength (ZDWL). Most glasses and dielectrics have their ZDWL in the SWIR spectral region, while for semiconductors it lies within the mid-IR or the LWIR regions.

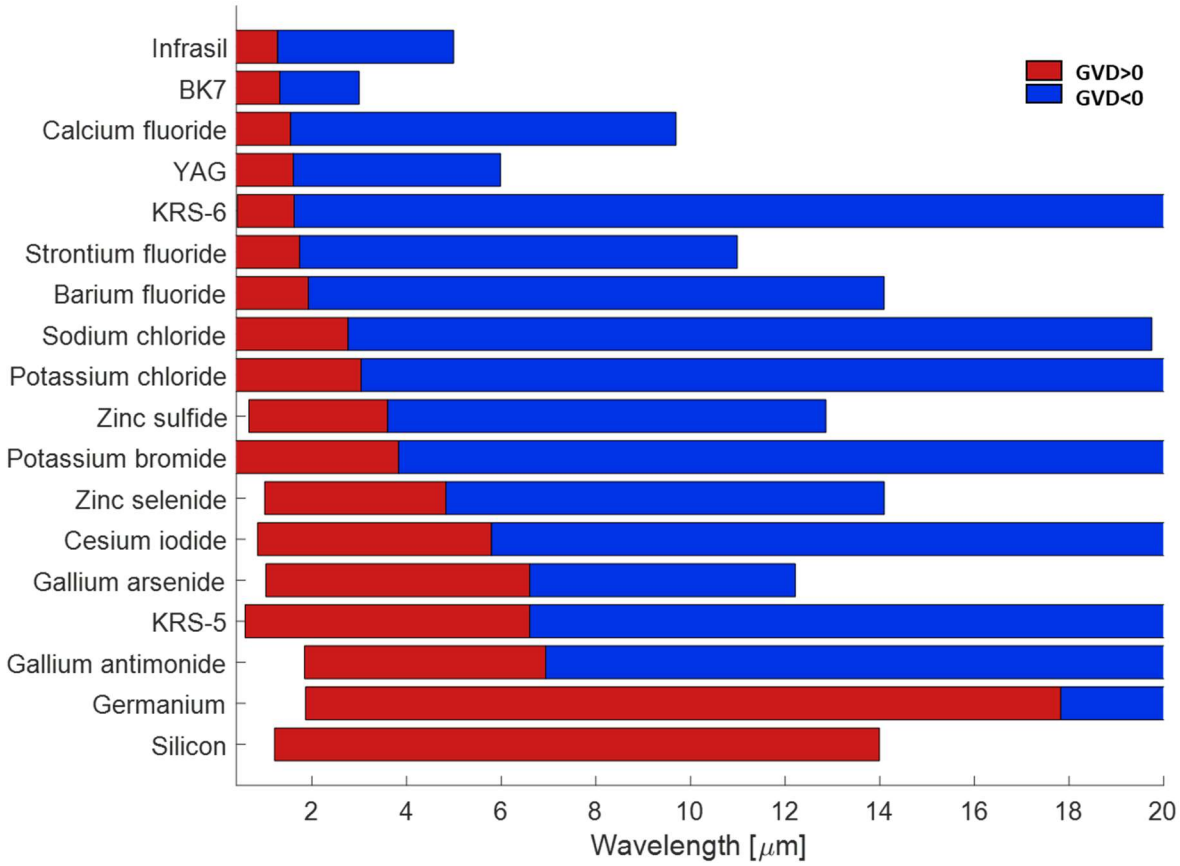

Fig. 6. The GVD sign of well-known isotropic solids in their infrared transparency window. The red bar stands for positive GVD and the blue bar stands for negative GVD, and they are separated by the zero-dispersion wavelength.

If a laser pulse propagates through a material with a central frequency close to the ZDWL of the material, it will only be affected by third and higher order dispersion. Compared to GDD, higher order dispersions have a much lower impact on pulse duration for the same amount of material propagation. For example, silica-based glasses usually contain dopants that shift the zero-dispersion wavelength toward 1550 nm, where the losses are also minimal. This way the optical signal close to this wavelength can maintain its temporal shape (soliton-like propagation) after much longer propagation distances. Alternatively, as phase derivatives add up linearly, one can achieve a similar effect in the mid-IR region by alternating positive and negative GVD materials with properly chosen thicknesses in the beam path, to achieve zero GDD in total. Unfortunately, STOD is positive for all materials, semiconductors and dielectrics too, at any given wavelength, so it cannot be nullified simply by propagating the laser pulse through a combination of different materials.

II.3. Nonlinear propagation of light

A nonlinear process was experimentally demonstrated by Franken et al. in 1961, when generating second harmonic in crystalline quartz [30]. In linear optics, when transition between energy states inside a material requires more energy than the energy of a single photon, light transmits through the material without absorption. This model is only valid for low intensity light, but at higher photon concentration other phenomena can occur. Multiple photons can contribute their energies to excite an energy transition, which we call nonlinear absorption. Non-absorptive optical processes can also occur at high optical intensities altering the linear model of light-matter interaction. We can use the perturbation theory to categorize these processes based on their order of nonlinearity. The higher the order of nonlinearity, the higher the intensities needed for them to appear. In linear optics, the optical response of homogenous nondispersive medium is linear, which was shown in Equation (II-8). The polarization vector can be expressed as

$$\mathbf{P} = \varepsilon_0 \chi^{(1)} \mathbf{E}\,, \tag{II-45}$$

where $\chi^{(1)}$ is the linear susceptibility, which is generally a second-rank tensor. This means that the **P** and **E** vectors are not necessarily parallel, which is the case in birefringent materials, where light travels at different speeds and directions in the crystal depending on the polarization of light.

In the nonlinear optics regime, at high optical intensities the approximation that the polarization vector linearly depends on the electric field no longer holds. In this case we can use Equation (II-46), where we can expand this nonlinear dependence as a power series of the **E** vector [31]

$$\mathbf{P} = \varepsilon_0 \left(\chi^{(1)} \mathbf{E} + \chi^{(2)} : \mathbf{EE} + \chi^{(3)} : \mathbf{EEE} + \cdots \right), \tag{II-46}$$

where $\chi^{(2)}$ and $\chi^{(3)}$ are third-rank and fourth-rank tensors known as the second- and third-order nonlinear optical susceptibilities, respectively. The elements of these power series all correspond to different physical processes, so we will distinguish them from one another as follows:

$$\mathbf{P^{(1)}} = \varepsilon_0 \left(\chi^{(1)} \mathbf{E} \right), \tag{II-47}$$

$$\mathbf{P^{(2)}} = \varepsilon_0 \left(\chi^{(2)} : \mathbf{EE} \right), \tag{II-48}$$

$$\mathbf{P^{(3)}} = \varepsilon_0 \left(\chi^{(3)} : \mathbf{EEE} \right), \tag{II-49}$$

where $\mathbf{P^{(1)}}$ is the linear polarization vector, while $\mathbf{P^{(2)}}$ is the second-order, and $\mathbf{P^{(3)}}$ is the third-order nonlinear polarization vectors. The electric field does not necessarily resonate at a single frequency, and in general it can be a combination of multiple fields oscillating at many different frequencies. This can happen when light is not monochromatic, as we have seen in Chapter II.1.2, or when lights from multiple sources coincide in a material. The linear polarization vector of Equation (II-47) is linearly related to the electric field, so it can only oscillate with the same frequencies as the electric field. On the other hand, second-order nonlinear polarization of Equation (II-48) can oscillate with the linear combination of all available frequencies, in a process called three-wave mixing.

II.3.1. Three-wave mixing

Let us suppose we have two monochromatic waves co-propagating with frequencies ω_1 and ω_2. In this case, the temporal distribution of the real electric field can be expressed as

$$E = E_1 e^{i\omega_1 t} + E_2 e^{i\omega_2 t} + c.c., \tag{II-50}$$

where c.c. stands for the complex conjugate of all the preceding parameters on the left side of the equation. The second-order polarization can be written as [32]

$$\begin{aligned} P^{(2)} &= \varepsilon_0 \chi^{(2)} \left(E_1 e^{i\omega_1 t} + E_2 e^{i\omega_2 t} + c.c.\right)\left(E_1 e^{i\omega_1 t} + E_2 e^{i\omega_2 t} + c.c.\right) = \\ &= \varepsilon_0 \chi^{(2)} \left({E_1}^2 e^{i2\ {}_1 t} + {E_2}^2 e^{i2\omega_2 t} + 2E_1 E_2 e^{i(\omega_1+\omega_2)t} + 2E_1 \overline{E_2} e^{i(\omega_1-\omega_2)t} + c.c.\right) + \\ &+ 2\varepsilon_0 \chi^{(2)} (E_1 \overline{E_1} + E_2 \overline{E_2}). \end{aligned} \tag{II-51}$$

The polarization components oscillating at a given frequency make electric fields oscillate at the same frequency, which results in the generation of new EM waves. These polarization components correspond to various nonlinear optical phenomena listed below

$$P_{SHG}^{(2)} = \varepsilon_0 \chi^{(2)} \left({E_1}^2 e^{i2\omega_1 t} + {E_2}^2 e^{i2\omega_2 t} + c.c.\right), \tag{II-52}$$

$$P_{SFG}^{(2)} = 2\varepsilon_0 \chi^{(2)} \left(E_1 E_2 e^{i(\omega_1+\omega_2)t} + c.c.\right), \tag{II-53}$$

$$P_{DFG}^{(2)} = 2\varepsilon_0 \chi^{(2)} \left(E_1 \overline{E_2} e^{i(\omega_1-\omega_2)t} + c.c.\right), \tag{II-54}$$

$$P_{OR}^{(2)} = 2\varepsilon_0 \chi^{(2)} (E_1 \overline{E_1} + E_2 \overline{E_2}). \tag{II-55}$$

Equation (II-52) describes the second harmonic generation (SHG) phenomenon, where the generated light oscillates at twice the frequency of the input wave, as also shown in Fig. 7. The phenomenon when frequencies of the waves are mixed and create light at frequency $\omega_1+\omega_2$ in Equation (II-53) is called sum frequency generation (SFG). Similar mixing occurs during difference frequency generation (DFG) described by Equation (II-54), where the generated light oscillates at the difference frequency $\omega_3=\omega_1-\omega_2$. Alternatively, using the same equation a different phenomenon can occur, when a wave oscillating at ω_3 frequency can interact with another input wave at ω_1 frequency to generate induced nonlinear polarization at ω_2 frequency. This way the initial beam at ω_1 frequency gets amplified, in a process called optical parametric amplification (OPA). The last component, which is shown in Equation (II-55), is the generation of a zero-frequency electric field, known as optical rectification (OR).

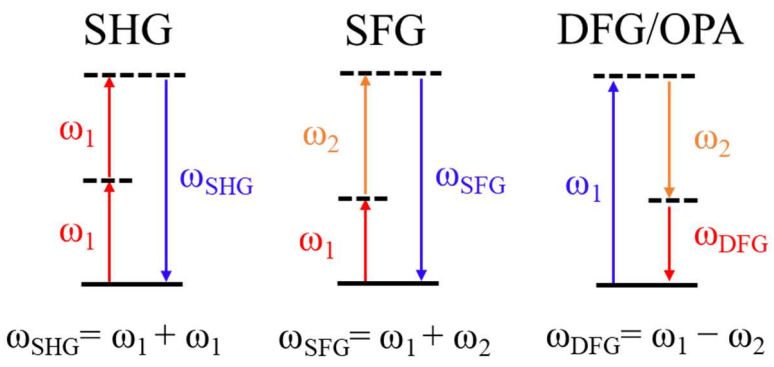

Fig. 7. Angular frequency relations of three-wave mixing processes.

Three-wave mixing can only occur if the crystal structure does not exhibit centrosymmetry. Unfortunately, gases, liquids, amorphous solids, and even most of the crystal materials are centrosymmetric, however there are a few noncentrosymmetric crystalline solids. These noncentrosymmetric crystals can be artificially synthetized, and if they form high quality single-crystals, they can exhibit macroscopic nonzero second-order nonlinear polarization. These nonlinear crystals are the building blocks of nonlinear physics, and they are the basis for many applications from quantum optics to laser physics [23,33]. It is important to note that the crystal properties – centrosymmetry and isotropy – overlap to some degree, but they are not the same. There are non-centrosymmetric isotropic crystals (e.g.: GaAs) and centrosymmetric birefringent crystals as well (e.g.: Sapphire).

Let us elaborate on the DFG/OPA processes as they are crucial for ultrafast (<1 ps) mid-IR lasers as shown in Chapter II.6.2. These interactions are governed by three conservation laws: energy conservation (II-56), momentum conservation (II-57), and the Manley-Rowe relation (II-58).

$$\hbar\omega_p = \hbar\omega_s + \hbar\omega_i \,, \tag{II-56}$$

$$k_p = k_s + k_i \,, \tag{II-57}$$

$$-\frac{dN_p}{dz} = \frac{dN_s}{dz} = \frac{dN_i}{dz} \,, \tag{II-58}$$

where ω is the angular frequency, $\hbar$ is the reduced Planck constant ($2\pi\hbar=h$), k is the wavenumber, N is the photon number, and z is the propagation direction. The different waves participating in the OPA process are traditionally called pump (p), signal (s) and idler (i) waves. It is customary to define them in a way to make the following relation hold true for them: $\omega_p > \omega_s > \omega_i$. These waves propagate at different speeds in the nonlinear medium, because of their different frequency and polarization state. When the wavenumbers corresponding to the propagation speeds satisfy the equation of momentum conservation (II-57), we call the process phase-matched. The deviation from this state is called phase mismatch, which causes the process to be less efficient. As the wavenumber generally depends on the frequency (dispersion), phase-matching is usually limited spectrally. The parametric bandwidth of a three-wave mixing process (or amplification bandwidth for OPA) is the spectral region, where the accumulated phase-mismatch of a nonlinear process does not exceed π. The bandwidth of the process can be extended by considering noncollinear geometry for the OPA (NOPA) [34], as shown in Fig. 8. Unfortunately, the generated signal in this case can have a pulse-front tilt as a result of the noncollinear geometry, which can limit the compressibility of the pulses [35]. Furthermore, the idler wave will have a strong angular chirp [36], which can be an issue if not only the signal, but also the idler wave is needed. Despite these issues, NOPA is widely employed when broad bandwidth amplification is necessary.

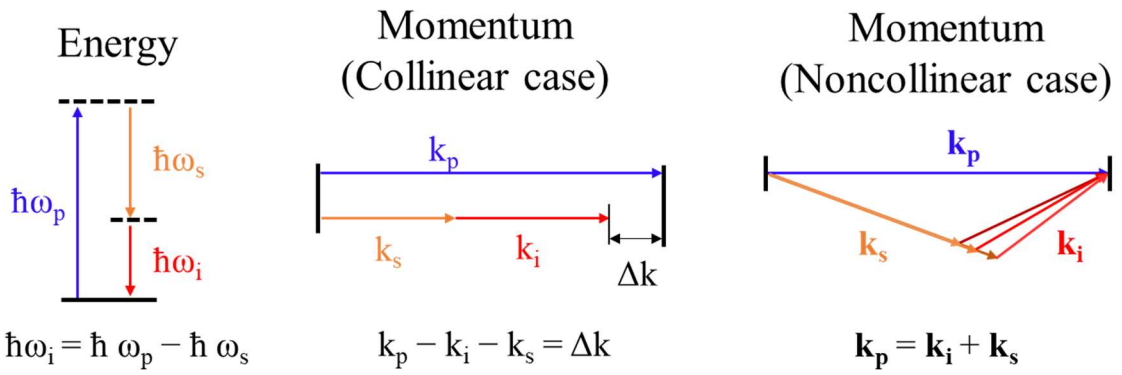

Fig. 8. Energy and momentum diagrams of the OPA process. The Δk is the phase mismatch at unit propagation length. The phase-mismatch can be reduced by employing noncollinear geometry, where the wavenumbers are nonparallel vectors. As a side effect, the idler will have angular chirp.

Phase-matching can be difficult to achieve as normal dispersion usually mandates that the refractive index monotonously increases with frequency. Let us take SHG as an example, where the phase-matching condition can be rewritten (II-57) in the following way [32]

$$\frac{n(\omega_{SHG})\omega_{SHG}}{c} = \frac{n(\omega_F)\omega_F}{c} + \frac{n(\omega_F)\omega_F}{c} = \frac{n(\omega_F)\omega_{SHG}}{c}, \tag{II-59}$$

where n is the refractive index, and ω_{SHG} and ω_F are the angular frequencies of the fundamental and SHG waves. Equation (II-59) can only be satisfied if the refractive index is the same at the fundamental and SHG frequencies, which is not true for materials with normal dispersion. However, phase-matching can still be achieved with several techniques [32]. The first one is called critical phase-matching (also called angle phase-matching), where a birefringent crystal is employed, which exhibit different refractive indices for different polarization waves. By adjusting the crystal angle, the wavenumber of the participating waves can be tuned, thus phase-matching can be achieved. The word 'critical' refers to the technique's relative sensitivity to misalignment. Additionally, in a birefringent crystal both the propagation speed and the propagation direction depend on polarization. This means that after some propagation in the crystal, depending on the crystal angle and beam diameters, the participating waves do not overlap spatially with one another. This process is called spatial (transversal and longitudinal) walk-off, and it limits the effective interaction length. This effect can be minimized with thin crystal materials and high optical intensities.

The second technique is called noncritical phase-matching (or temperature phase-matching), as some crystals e.g.: LN have strongly temperature dependent birefringence. Just by tuning the temperature of the crystal, phase-matching can be achieved without any change in the crystal angle. Furthermore, the crystal is cut perpendicular to the crystal axis, so all waves propagate along the crystal axis, which in turn prevents spatial walk-off between the participating waves.

The third technique is called quasi-phase-matching (QPM), where phase-matching is achieved in a periodic poled or orientation-patterned crystal with parameters designed for the application. The interacting waves in the QPM process can even have the same polarization, which in some cases can yield even higher conversion efficiency than critical phase-matching, and QPM works with collinear geometry too. Furthermore, for QPM it is not necessary to use birefringent materials; isotropic materials e.g.: GaAs can also be employed, but they still have to be non-centrosymmetric. The problem with QPM crystals is that they are difficult to manufacture with reliable quality. Furthermore, crystal thickness is limited, which consequently

limits the maximum aperture size. There are two major subgroups of QPM crystals, periodically poled (PP) materials, where the structure is fabricated in such a manner that the orientation of one of the crystalline axes is inverted periodically. This method requires ferroelectric materials for the poling process. For non-ferroelectric semiconductors with a cubic lattice structure such as GaAs, the orientation-patterning (OP) technique is used most often to achieve QPM.

II.3.2. Four-wave mixing

As the name suggests, in four-wave mixing four waves interact with one another. This arises from the third-order nonlinearity, but contrary to its second order counterpart, all media exhibit it regardless of symmetry consideration. Third-order nonlinearity can be described with the third-order nonlinear optical susceptibility of Equation (II-49). It is a fourth rank tensor, represented by a 3^4=81 element matrix [37]. While the third-order nonlinearity tensor fully describes four-wave mixing processes, it is beyond the scope of this dissertation. Instead, we would treat third-order nonlinearity as a scalar, assuming that all participating waves are linearly polarized and propagate in the same direction, and also that the medium is isotropic, where the electric field and the polarization vector of Equation (II-49) are parallel with each other. Furthermore, for further simplification, we will assume centrosymmetric media and only consider the first and third-order nonlinear optical susceptibilities [38]

$$\mathbf{P} = \varepsilon_0\left(\chi^{(1)}\mathbf{E} + 3\chi^{(3)}\mathbf{E}^3\right) = \varepsilon_0\left(\chi^{(1)} + 3\chi^{(3)}|\mathbf{E}|^2\right)\mathbf{E} = \varepsilon_0\chi_{\text{eff}}\mathbf{E}\,. \tag{II-60}$$

With this method we derive an effective electric susceptibility (χ_{eff}) second-rank tensor to express the polarization vector mirroring the Equation for linear polarization (II-45). We can express electric susceptibility with permittivity from Equation (II-8)

$$\chi_{\text{eff}} = \frac{\varepsilon}{\varepsilon_0} - 1\,. \tag{II-61}$$

Based on this result, we can derive a formula for the refractive index at high optical intensities using Equation (II-17)

$$\mathrm{n} = \sqrt{\frac{\varepsilon\mu}{\varepsilon_0\mu_0}} = \sqrt{\frac{\mu}{\mu_0}}\sqrt{1+\chi_{\text{eff}}} = \sqrt{\frac{\mu}{\mu_0}}\sqrt{1+\chi^{(1)}+3\chi^{(3)}|\mathbf{E}|^2}. \tag{II-62}$$

If the $3\chi^{(3)}|E|^2$ product is much smaller than $1+\chi^{(1)}$, which is usually the case, we can separate the intensity dependent component

$$\mathrm{n} \approx \sqrt{\frac{\mu}{\mu_0}\left(1+\chi^{(1)}\right)} + \frac{3}{2}\sqrt{\frac{\mu}{\mu_0\left(1+\chi^{(1)}\right)}}\chi^{(3)}|\mathbf{E}|^2 =$$

$$= \sqrt{\frac{\mu}{\mu_0}\left(1+\chi^{(1)}\right)} + \frac{3}{4}\frac{\mu\chi^{(3)}}{\mu_0\varepsilon_0 {n_0}^2 c}\mathrm{I} = \mathrm{n}_0 + \mathrm{n}_2\mathrm{I}\,, \tag{II-63}$$

where n_0 is the linear refractive index and n_2 is the nonlinear refractive index. As the refractive index is dimensionless, the nonlinear refractive index can be expressed in units of cm^2/W, which is most often positive, but it can be negative under some special conditions [39]. We can see that the nonlinear refractive index contributions only appear at high intensities, which phenomenon is called optical Kerr effect.

The optical Kerr effect has significant consequences for ultrashort laser propagation. As the intensity is rarely homogenous across the spatial cross-section of the pulse, the refractive index

of the media will take the shape of the intensity profile. In case of a Gaussian beam, the refractive index is the highest at the peak and the weakest at the tails. This effectively creates a nonlinear lens in the media, which results in the beam focusing itself, i.e. self-focusing [38] (or self-defocusing when n_2 is negative). A similar effect occurs in the temporal domain. The medium will change its refractive index as more and more intense parts of the pulse interact with it. As a result, the different temporal slices of the pulse accumulate different nonlinear phase shift as they propagate through the material [38]. This uneven phase accumulation is especially noticeable if we use the Fourier transform of (II-23) to determine the spectral distribution of the electric field. We have seen in Chapter II.2.2 that the temporal shape is the shortest if the spectral phase is flat. The same is true for the opposite; if the temporal phase is not flat, the spectrum is broader. The accumulated nonlinear temporal phase shift function is nonlinear; as a consequence, the spectrum broadens during propagation by self-phase modulation (SPM), which is the basis for the post-compression of mid-IR pulses described in Chapter II.6.3. The amount of nonlinear phase accumulated by a pulse through propagation is expressed by the B-integral

$$B \approx \frac{2\pi}{\lambda_c} \int_0^L n_2 I(z) dz\,, \tag{II-64}$$

where L is the thickness of the media, and λ_c is the central wavelength of the optical pulse. If the influence of plasma and dispersion effects can be neglected, the B integral keeps accumulating for the laser pulse, which means the spectrum broadens continuously as the laser pulse propagates. When an extremely broadband continuous spectrum is generated, the process is called supercontinuum generation (SCG).

Similarly to the linear refractive index, the nonlinear refractive index also depends on the frequency of the wave. It was important to approximate n_2 at mid-IR frequencies for the post-compression experiment described in Chapter III.3. Most nonlinear refractive index measurements use near-IR and VIS sources, which makes the results unreliable for mid-IR application. Furthermore, nonlinear refractive index data are scarce and are sometimes acquired by very different nonlinear measurement methods with large error bars, making the data points fluctuate by orders of magnitude from measurement to measurement. To acquire an approximation for the nonlinear refractive index in the mid-IR range, I have used the formula for nonlinear dispersion, as described in detail by M. Sheik-Baha et. al. [40,41]

$$n_2(f) = \frac{C}{n_0(f)^2 E_g{}^4} G\left(\frac{hf}{E_g}\right), \tag{II-65}$$

where n_0 is the linear refractive index, E_g is the material bandgap, C is a parameter mostly independent of the material, and G is a complex algebraic function described in reference [41]. The nonlinear refractive index strongly depends on the bandgap, as it is its power function with the order of –4. This explains why semiconductors, especially narrow bandgap semiconductors e.g.: Si, Ge and GaAs have large n_2 values. To determine the n_2 at mid-IR frequencies, Function (II-65) was fitted on the measured data points, treating E_g and C as fitting parameters. Using this method, I could acquire a good approximation for the n_2 values at the central wavelength of the MIR laser (3.2 μm). Note that in all cases the fitted E_g parameters were relatively close to the literature values (<10% difference), which validated the fitting process.

To facilitate access to the nonlinear refractive indices of materials, I created a material database in C++ and built a GUI for it with QT for Windows operating systems. This database

software can calculate the nonlinear refractive index at any given wavelength in the transmission windows of the contained materials. As time went on, I have added even more functionality to the software and more materials to the database (even some glasses, gases, and liquids), based on everyday needs during my laboratory work. Now it can calculate many different material parameters at any given wavelength, such as nonlinear and linear refractive index, dispersion parameters, absorption, and also the ZDWL in the first tab of the software. The second tab was created to calculate surface Fresnel losses at different polarization and incidence angles at the interface of any two materials in the database. The third tab contains information about crystal materials like their crystal system, birefringence, centrosymmetry, density, thermal conductivity and many more. The software is fairly compact; the whole program only takes up 69 MB of space on the hard drive. The GUI showing material parameters under the first tab is shown in Fig. 9.

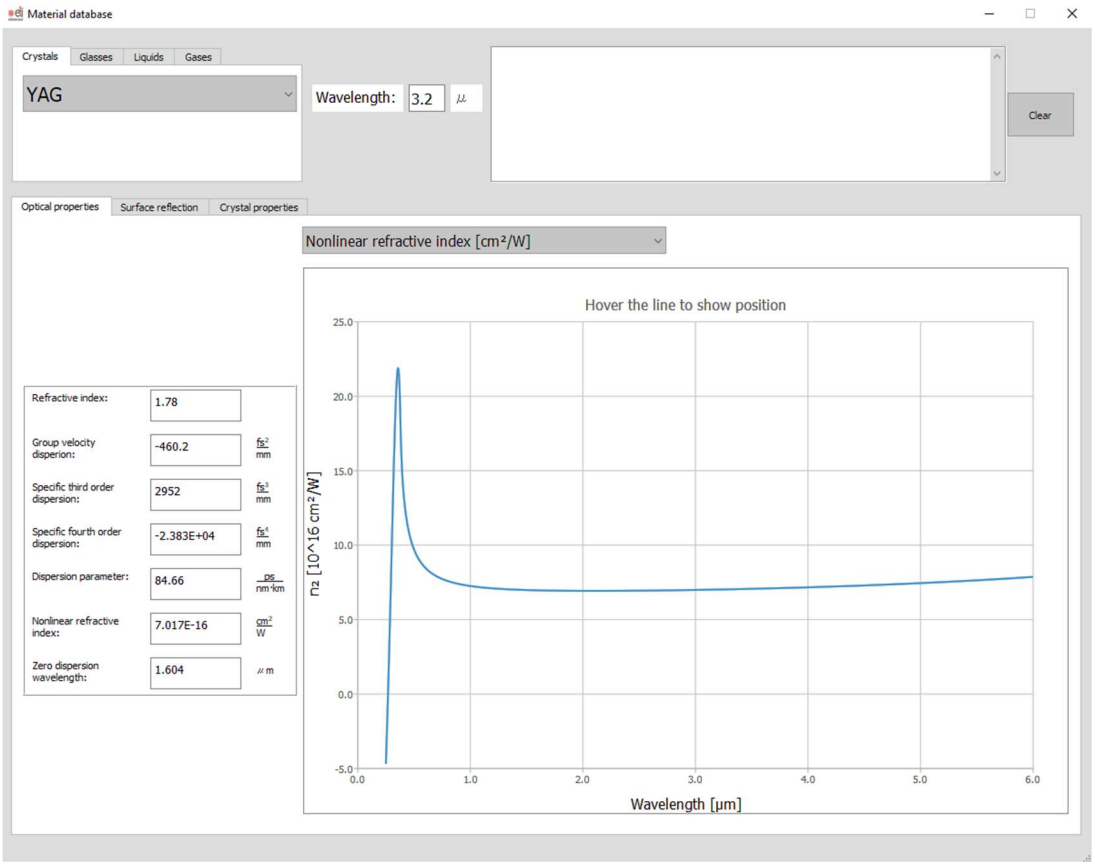

Fig. 9. The GUI of the material database software designed to allow instant access to material parameters, such as nonlinear and linear refractive indices, dispersion parameter, absorption, surface reflections, crystal system and many more.

II.3.3. Phase relations of parametric processes

When describing parametric processes, I have mainly focused on the frequency relations of the generated waves, but for several applications phase relations are equally important. Let us start with the phase relation between the fundamental and the SHG pulses. This I can derive from a simplistic theoretical model, and for the other parametric processes only the final relations are presented. The complex electric field of the pulse (E_F) can be expressed by its real amplitude (A_F) and phase (Φ_F). This can be expanded using the one-dimensional scalar electric field of

Equation (II-20) traveling in the z direction with a central angular frequency of ω_c, k_F wave number and φ_F temporal phase

$$E_F = A_F e^{i\Phi_F} = A_F e^{i(\omega_c t - k_F z + \varphi_F(t))}. \quad \text{(II-66)}$$

In this one dimensional model, the generated SH pulse also travels in the z direction with a wave number of k_{SH}, and its angular frequency is the double of the fundamental, which can be written as

$$E_{SH} = A_{SH} e^{i\Phi_{SH}} = A_{SH} e^{i(2\omega_c t - k_{SH} z + \varphi_{SH}(t))}. \quad \text{(II-67)}$$

The electric field of SH can be derived from the fundamental electric field as they are coupled by the nonlinear polarization vector of the material [32]. The coupling strength can be determined from the effective value of the d matrix (d_{eff}), which is most commonly used to quantize the three-wave mixing processes. The spatial evolution of the SH wave can be expressed as

$$\frac{dA_{SH}}{dz} e^{i\Phi_{SH}} = \frac{2id_{eff}(2\omega_c)^2}{c^2 k_{SH}} (A_F)^2 e^{i2\Phi_F}. \quad \text{(II-68)}$$

In Equation (II-68), both sides contain complex values, so both the amplitude and the phase must be equal. Let us only consider the phase relation and arrive at equation

$$\Phi_{SH} = 2\Phi_F + \frac{\pi}{2}. \quad \text{(II-69)}$$

Furthermore, we can assume that the phase-mismatch of Equation (II-57) of the SHG process is close to zero ($\Delta k = k_{SH} - 2k_F \sim 0$). In this case, the temporal phase of the SH pulse can be calculated from Equation (II-69)

$$\varphi_{SH} = 2\varphi_F + \frac{\pi}{2}. \quad \text{(II-70)}$$

Similarly, equations can be derived for DFG/OPA processes

$$\varphi_i = \varphi_p - \varphi_s - \frac{\pi}{2}, \quad \text{(II-71)}$$

where φ_i, φ_p and φ_s stand for the temporal phase of the idler pump and signal, respectively. The SPM processes can be understood as a four-wave mixing parametric process, where the three of the four waves are monochromatic components of the fundamental laser pulse and the fourth wave is a component of the resulting self-phase modulated wave [42]. The phase relation in this case can be written as

$$\varphi_{SPM} = \varphi_{F1} - \varphi_{F2} + \varphi_{F3} + \frac{\pi}{2}, \quad \text{(II-72)}$$

where φ_{F1}, φ_{F2} and φ_{F3} stand for the temporal phase of three fundamental waves, and φ_{SPM} is the temporal phase of the result of the self-phase modulation process. These equations contain the temporal phase; for the spectral phase the same equation can be derived [43]. The findings are summarized graphically in Fig. 10.

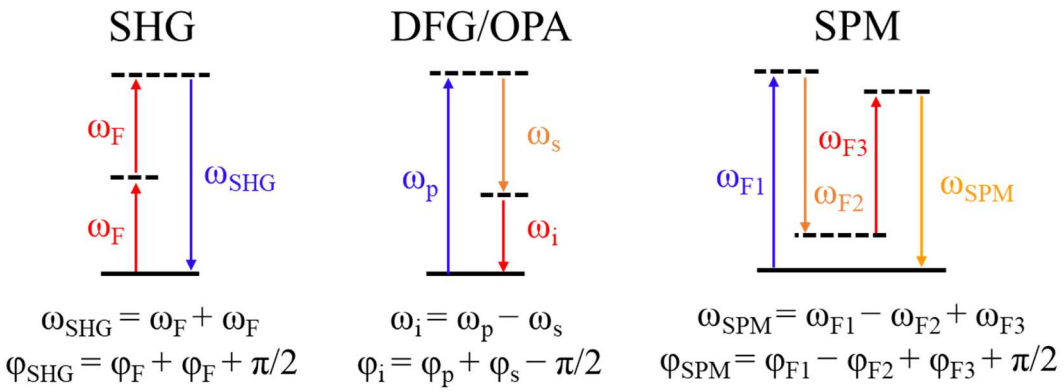

Fig. 10. Phase and frequency relations of common parametric processes i.e.: SHG, DFG, OPA and SPM. The letters F, i, p, and s stand for fundamental, idler, pump and signal waves, respectively. The SPM process involves three fundamental waves: F1, F2 and F3.

The CEP of the pulse can be understood as the value of its temporal phase at the peak of the pulse. As a result, the phase relations described by Equations (II-70) to (II-72) hold true for the CEP too [42]. This has profound consequences for both interferometric CEP measurements (see Chapter II.5.1) and for passive CEP stabilization [42]. In the OPA process, the idler CEP is the difference of the CEP of the seed and the pump. In the passive CEP stabilization schemes both of them have the same CEP (disregarding constant offsets), so the CEP of the idler will be a constant value, meaning it will be CEP stable. To achieve this, a self-seeded OPA scheme is most often used, where the pump and seed originate from the same source [42,44]. This results in a CEP stable idler, shown in Fig. 11.

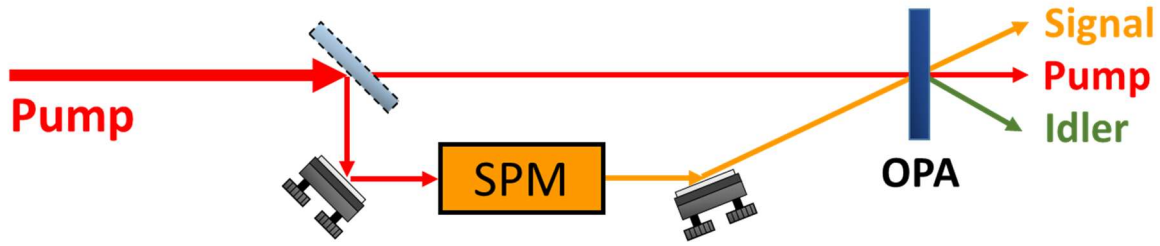

Fig. 11. A common example for a self-seeded OPA scheme to achieve a passive CEP stable idler. For easier understanding, a noncollinear scheme is presented here, but the idler is also CEP stabilized, when collinear OPA is employed.

II.4. Interferometry

When two or more EM waves coincide in space and time, the resulting wave's intensity is not a simple addition of the intensity of the incoming waves. The EM waves possess both amplitude and phase, and if these waves are coherent and have components in the same polarization direction, interference will occur at the superposition of the waves. For the description of this process let us assume two plane waves with the same polarization direction; for this we can use the scalar electric field of Equation (II-20)

$$E(t,\mathbf{r}) = E_1 e^{i(\omega t - \mathbf{k}\cdot\mathbf{r} + \varphi_1)} + E_2 e^{i(\omega t - \mathbf{k}\cdot\mathbf{r} + \varphi_2)} . \tag{II-73}$$

Coherence between them is enforced by the waves propagating with the same wavenumber (**k**) and angular frequency (ω). We can determine the resulting intensity of the interfering waves using Equation (II-25), normalized so we can disregard constant multipliers

$$I_n(t,\mathbf{r}) = E(t,\mathbf{r})\overline{E(t,\mathbf{r})} = {E_1}^2 + {E_2}^2 + 2E_1E_2\cos(\varphi_2 - \varphi_1) . \tag{II-74}$$

The interference is called constructive between these two waves when the phases of the waves are the same (modulo 2π), which results in the highest possible intensity value. Interference is called destructive when the phases of the waves differ by π (modulo 2π), which results in the lowest possible intensity. The intensity of a wave is something we can measure directly as opposed to the electric field. If the phase between two waves changes in time or space, we can determine this phase difference by measuring the intensity fluctuation. This principle is the basis of interferometry, and a device used for interferometry is called an interferometer.

There is a great selection of interferometers with different advantages and applications. In this work two types of interferometers are used (excluding common-path nonlinear interferometers used for CEP detection in Chapter II.5.1): Mach-Zehnder and Michelson interferometers. Both of them are shown in Fig. 12. The optical path difference, and consequently the phase difference between the arms are usually adjusted by a delay line. These interferometers are interchangeable for most applications, although there are some subtle differences. In both types, the incoming beam is separated into two beams by a beam splitter. In contrast to Michelson interferometers, Mach-Zehnder interferometers have the benefit that no back reflection occurs towards the laser source. On the other hand, Michelson interferometers require fewer optical elements in their design. Michelson interferometers are also more suitable for dual-band SRI measurements, as detailed in Chapter III.2.

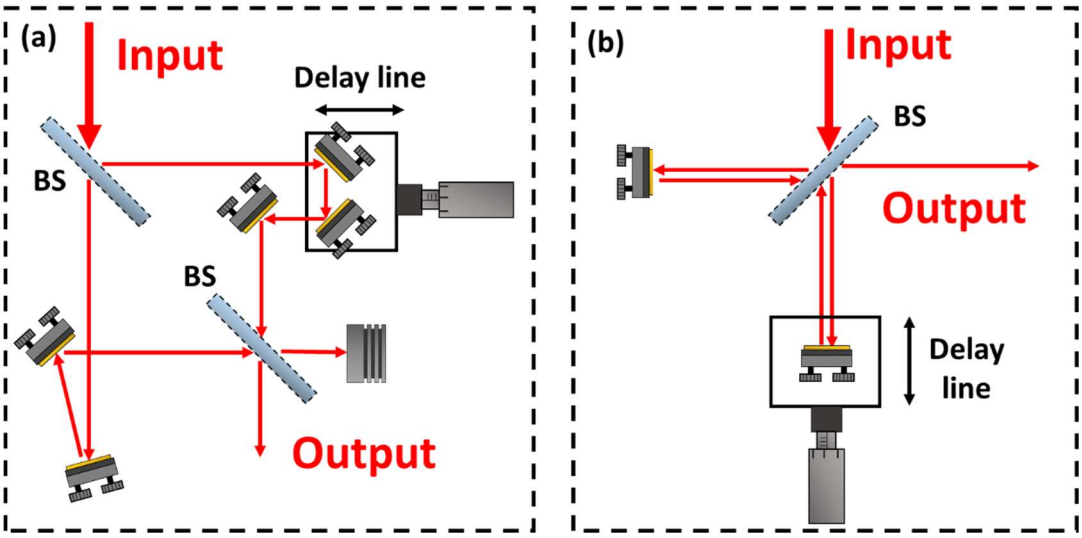

Fig. 12. (a) Mach–Zehnder interferometer and (b) Michelson interferometer used to measure the phase difference between the arms. BS: Beam splitter

There are two kinds of interference created by these interferometers: one in the time domain and the other is in the spectral domain. Let us suppose that coherent light is sent into the interferometer and we measure the output intensity with a photodetector. Then we record the signal continuously, while the delay between the two arms of the interferometer is changed. The two arms will constructively or destructively interfere depending on the momentary phase difference between the arms, so the recorded signal will be a temporal interference signal. In the other case, the illuminating source is spectrally broadband, and instead of a photodetector we record the signal of the interferometer with a spectrometer. This way the delay between the two arms does not need to be changed during measurements, as the interference will appear in the spectral domain, and the "frequency" of spectral modulation can be measured in seconds.

In this dissertation we mainly focus on the second case, when spectral interference is recorded. Let us describe the interference of two pulses with the same central frequency

$$E(f) = A_1(f)e^{i(2\pi f \cdot GD_1 + \varphi_1(f))} + A_2(f)e^{i(2\pi f \cdot GD_2 + \varphi_2(f))}, \quad \text{(II-75)}$$

where GD_1 and GD_2 are the group delays of the two pulses and φ_1 and φ_2 are their spectral phase and A_1 and A_2 are real amplitude functions. The normalized spectral intensity in this case can be written as

$$I_n(f) = E(f)\overline{E(f)} = {A_1}^2 + {A_2}^2 + 2A_1A_2\cos(2\pi f \Delta GD + \Delta\varphi(f)), \quad \text{(II-76)}$$

where ΔGD is the group delay difference and $\Delta\varphi$ is the spectral phase difference between the two arms. The resulting spectral intensity modulation's "frequency" will be the GD difference between the two pulses. We can see that the phase of the interference is linearly related to the phase difference between the two waves, so recovering the phase of the interference also yields the phase difference between the waves with the addition of a constant offset.

II.4.1. Spectrally resolved interferometry

Spectrally resolved interferometry (SRI) is the most commonly used method to characterize the spectral phase shift of different optical elements [45]. SRI relies on two-arm interferometers, most commonly Michelson or Mach-Zehnder interferometers depicted in Fig. 12. The

interferometer is illuminated by a broadband source, and the investigated optical element is inserted in one of the two arms, which will cause a phase shift difference between the arms. The created interference is then recorded by a spectrometer, which enables us to recover the spectral phase of the optical element. This method is highly versatile, it can be used to measure physical distances, as well as to determine the refractive index or the dispersion parameters of materials.

For broadband sources several options are available. White light or super-continuum sources are generally the best option, when the broadness of the spectrum is the only concern. Unfortunately, wide bandwidth spectrometers usually underperform in terms of spectral resolution and dynamic range, hindering precise phase retrieval. This issue is much more severe when phase derivatives are investigated, as in this case the relative error is amplified by each successive derivation. Also, temporal coherence is inversely proportional to the bandwidth, which limits the available maximum fringe density of the interferograms. Ultrafast laser sources provide a middle-ground between high temporal coherence monochromatic and low temporal coherence white light sources. They are not often used as they are more expensive and complex than other sources, but they can provide an excellent solution in laboratories already equipped with these types of lasers. They also provide high peak power pulses, which is necessary for the nonlinear SH-SRI and the dual-band SRI techniques detailed in Chapters II.4.3 and III.2, respectively.

The optical elements' spectral phase shift gained from the recorded interferograms can be evaluated with several methods, all of which have advantages and disadvantages. The minima-maxima method [46,47] uses the fact that the extremums of the interferogram are spaced equidistantly in the frequency domain. When normalizing the interferogram, the local minimum and maximum values are easy to determine, but the recovered spectral phase has a low resolution compared to the resolution of the interferogram. Another evaluation technique is the cosine function fit method, where a cosine function is fitted to the spectral intensity of Equation (II-76). The phase of the fitted cosine function is written as a polynomial described in Equation (II-38), with the phase derivatives as free parameters of the fitting. However, one of the most reliable methods is the Fourier transform spectral analysis [48], where discrete Fourier transform is used to recover the phase of the interferogram. In this dissertation only this method was used not only to recover the phase of the optical elements with the dual-band SRI, but also to determine the CEP of a laser pulse detailed in Chapters II.5.1 and III.1.

II.4.2. Fourier transform spectral analysis

The Fourier transform spectral analysis is widely applied to determine the spectral phase of an interference pattern. It is a powerful tool used in linear and nonlinear optics alike. However, before the analysis can start, there is one important thing to be considered. The most commonly used spectrometers are grating based, which do not disperse light evenly in the frequency domain [49]. The fastest discrete Fourier transform algorithm is FFT, which prerequisites equidistant frequency distributions. This means that if the spectrum is not evenly spaced in frequency, the data requires processing before the analysis can be performed.

This problem is further complicated by the fact that grating spectrometers have a finite chip size in their detector array, effectively integrating light within unevenly sized frequency regions. Thus, we cannot interpret the recorded spectrum as a function, but rather as a

histogram, which gives us the integrated spectral intensity within a frequency range. When converting such a measured spectrum into a spectrum with even frequency, the bin sizes will also change. It is a quite common mistake to use polynomial interpolation algorithms only to calculate the spectrum evenly spaced in frequency. To obtain the correct result, the ratio of the bin sizes must be used as the intensity correction function to the interpolated data [49]

$$S_f(f) = S_x\big(x(f)\big)\left|\frac{dx(f)}{df}\right|, \tag{II-77}$$

where S_x is the measured spectrum with measured values at the x bin (pixel) positions, S_f is the interpolated spectrum with equidistant frequency spacing, dx is the bin size of the spectrometer, and df is the frequency resolution of the frequency equidistant spectrum. All the bins of the spectrometer have a corresponding frequency value, and this function is retrieved when the spectrometer is calibrated. The numerical derivative of this function is exactly the correction function for the measured spectrum. The effect of this correction is noticeable in most cases, as shown in Fig. 13, but it has minimal influence in most applications (e.g.: SRI), which is why it is so often ignored.

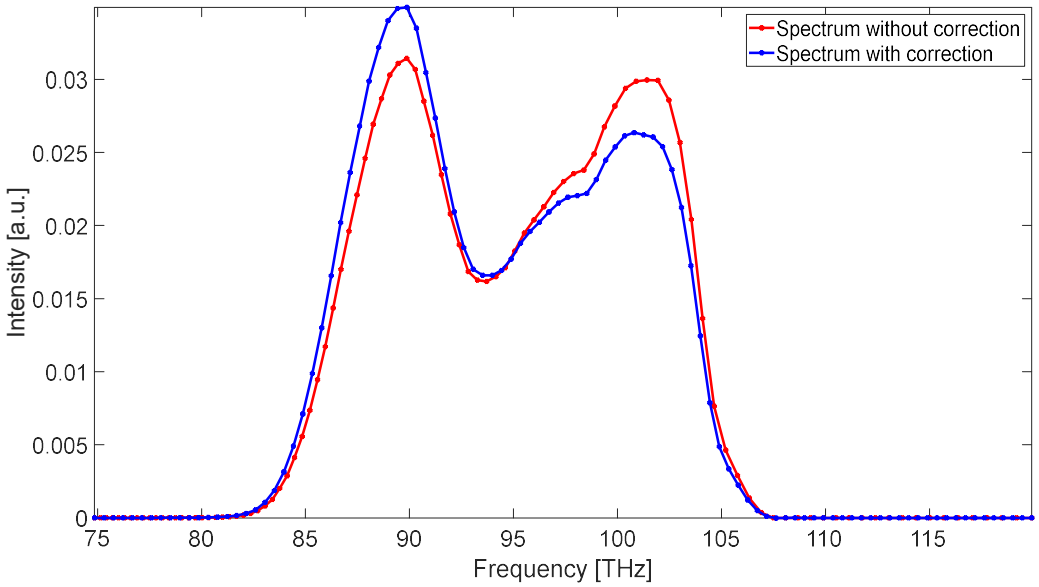

Fig. 13. Converting the spectrum measured by a spectrometer into a spectrum with equidistant frequency with and without intensity correction.

If a spectrum is equidistant in frequency, the FFT algorithm can be safely applied. Using Equation (II-24) we can see what happens in the Fourier domain, using the FT

$$\mathcal{F}\{I_n(f)\}(\tau) = \mathcal{F}\{{A_1}^2 + {A_2}^2\}(\tau) + \mathcal{F}\{2A_1A_2\cos(2\pi f\cdot \Delta GD + \Delta\varphi(f))\}(\tau)\,. \tag{II-78}$$

We can separate the first (DC term) component of the right side

$$DC(t) = \mathcal{F}\{{A_1}^2 + {A_2}^2\}(\tau)\,. \tag{II-79}$$

The cosine function of Equation (II-78) can be written as the sum of two complex functions, so we can derive the expression as follows

$$\mathcal{F}\{I_n(f)\}(t) = DC(\tau) + \mathcal{F}\{A_1A_2e^{i(2\pi\cdot\Delta GD+\Delta\ (f))} + A_1A_2e^{-i(2\pi f\cdot\Delta GD+\Delta\ (f))}\}(\tau) =$$

$$= DC(\tau) + \delta(\tau-\Delta GD) * \mathcal{F}\{A_1A_2e^{i\Delta\varphi(f)}\}(\tau) + \delta(\tau+\Delta GD) * \overline{\mathcal{F}\{A_1A_2e^{i\Delta\varphi(f)}\}(\tau)}\,, \tag{II-80}$$

where the * symbol stands for convolution. The convolution of Dirac delta and a function results in the function's shift in its argument by the argument of the Dirac delta function

$$\mathcal{F}\{I_n(f)\}(\tau) = DC(t) + \overline{\mathcal{F}\{A_1A_2e^{i\Delta\ (f)}\}(\tau + \Delta GD)} + \mathcal{F}\{A_1A_2e^{i\Delta\varphi(f)}\}(\tau - \Delta GD)\,. \qquad \text{(II-81)}$$

The three components in Equation (II-81) will be separated into three spikes in the τ time domain, centered around –ΔGD, 0, and ΔGD, which is displayed in Fig. 14. As both –ΔGD, and ΔGD contain information about the phase, only one of them is necessary for reconstruction, the other one and the DC spike at 0 can be filtered out. Usually the ΔGD spike is chosen as no extra operation is necessary to recover the phase in that case

$$I_{filtered}(t) = \mathcal{F}\{A_1A_2e^{i\Delta\varphi(f)}\}(\tau - \Delta GD)\,. \qquad \text{(II-82)}$$

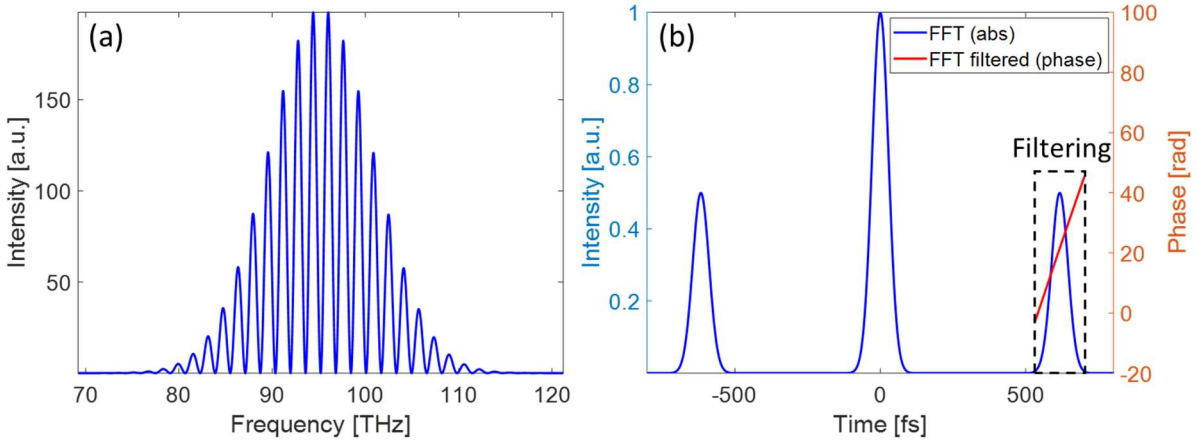

Fig. 14. a) The spectrum resulting from the interference between two pulses. b) The absolute value and phase of the FFT transformed spectrum plotted against time. If we only keep the ΔGD spike and filter out everything else, the phase of the original spectral interference can be recovered.

After filtering, IFFT is applied, which will result in

$$\mathcal{F}^{-1}\{I_{filtered}(t)\} = A_1A_2e^{i(2\pi f\cdot\Delta GD+\Delta\varphi(f))}\,. \qquad \text{(II-83)}$$

The IFFT produces a complex data array. The amplitude of this complex array is the multiplication of the spectral amplitudes in the two arm. On the other hand, the phase of the complex array is exactly the spectral phase difference between the arms disregarding constant offset. During SRI measurements, the sample is inserted into one of the arms, and the phase difference between the arms changes by exactly the phase of the sample. By subtracting the phase difference of the empty interferometer from our measurement we can determine the spectral phase shift of the sample.

II.4.3. Second harmonic assisted spectrally resolved interferometry

The second harmonic assisted spectrally resolved interferometry (SH-SRI) technique is an upgrade of the standard SRI method, as in the mid-IR region the commercially available spectrometers are quite expensive, bulky and their spectral resolution is limited [50]. Furthermore, the low spectral resolution is especially limiting for the Fourier transform spectral analysis. To circumvent this problem, an elegant solution was proposed: implementing second harmonic generation after the interferometer in order to shift the spectrum and therefore the detection range to a higher frequency region, where high resolution spectral measurements can

be performed by commonly available, high resolution SWIR spectrometers. Fig. 15 gives the schematic representation of such a device, consisting of a Mach-Zehnder interferometer and an SHG block.

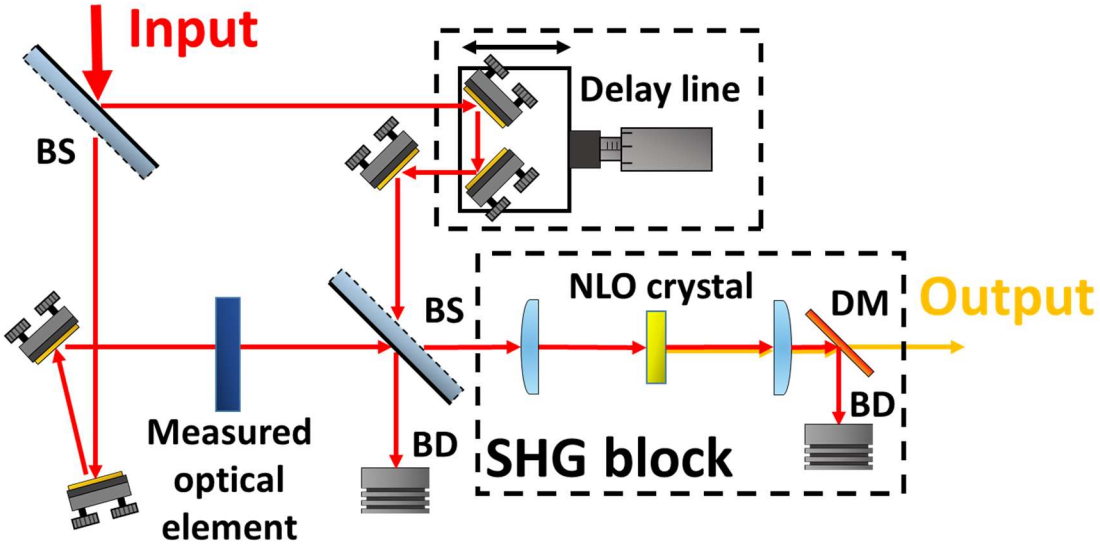

Fig. 15. Schematic diagram for SH-SRI, based on a Mach-Zehnder interferometer and SH generation in a nonlinear crystal. BS – beam splitter, DM – dichroic mirror; BD – beam dump.

The generated SH spectrum also contains an interference pattern. Based on Equations (II-70) and (II-76), the spectral phase extracted from the interference pattern at the SH wavelength is twice the spectral phase difference between the two arms of the interferometer

$$I_n(f) = E(f)\overline{E(f)} = {A_1}^2 + {A_2}^2 + 2A_1A_2\cos\left(2\pi f\Delta GD + 2\varphi_{F2}(f) - 2\varphi_{F1}(f)\right) =$$

$$= E(f)\overline{E(f)} = {A_1}^2 + {A_2}^2 + 2A_1A_2\cos\left(2\pi f\Delta GD + 2\Delta\varphi_F(f)\right), \qquad \text{(II-84)}$$

We can recover this spectral phase from the recorded interference pattern with the same methods as described in Chapter II.4.1. The spectral phase derivatives at the fundamental frequency can be extracted by dividing the measured spectral phase by two and expanding it around the fundamental angular frequency ω. This method can be upgraded even more to measure two spectral bands simultaneously, which is the main focus of Chapter III.2., where I present the dual-band SRI technique.

II.5. Carrier-envelope phase metrology

After the first observation of attosecond pulses [5], in the past twenty years experiments have become possible in material physics [51–54] and chemistry [55] on the sub-femtosecond timescale. These experimental techniques depend on CEP, so they require at least tens of microjoule energy, few-cycle driving pulses, where either the CEP of the pulse train is stabilized or pulse tagging is available [51,52]. Both pulse tagging and active CEP stabilization require the real-time measurement of CEP. It is important to note that several experimental applications, such as attosecond coincidence spectroscopy [52–54], time-resolved photoelectron microscopy [56], and quantum optics based XUV spectroscopy [57], benefit from high repetition rates (~10-100 kHz), as high repetition rate drivers drastically reduce the data accumulation time and improve the signal-to-noise ratio. Consequently, laser technology is being pushed towards higher and higher repetition rates to establish a foundation for MHz beamlines and attosources of the future [58,59]. In both cases, single-shot CEP detection is required, which is highly challenging for ~MHz pulse trains with the current technology.

Over the years, many single-shot CEP measuring techniques have emerged which we can divide into two categories based on the fundamental physical process they rely on: ionization based methods and interferometric methods. The difference between the values measured by these methods are subtle, but important. In the case of ionization based methods, the laser pulses are focused in a gas medium, and the resulting ionized electrons are used to determine the CEP at the focus point. This method is a localized CEP measurement, as the CEP of the pulses is known at an exact point (focus point). This is also called absolute CEP measurement in literature, although this name can be misleading, because with the propagation of a laser beam the phase of the laser also advances, which increases the CEP by a constant value. This means that measuring the localized CEP with a diagnostic device only informs us about the exact CEP value at the focus, but everywhere else the CEP will differ with an unknown constant offset.

In delocalized CEP measurements (also called relative CEP measurements), which is the result of single-shot interferometric methods, the measured CEP value cannot be assigned to a single point in space. This means that the CEP of a single pulse can only be known with the addition of an unknown constant phase shift anywhere. The constant phase shift offset of the delocalized CEP measurements can be determined at the target area, if a reference localized CEP measurement is available at the target. This way the localized CEP of every consequent pulse can be calculated from the measured delocalized CEP, provided that the beam path is not altered in the meantime. To further complicate matters, the interferometric methods which rely on temporal modulation do not actually measure the CEP, but rather the CEO frequency. Measuring the CEO only allows us to determine the change in CEP between consecutive pulses calculated from Equation (II-28), which prevents pulse tagging.

Despite this difference, the localized and delocalized CEP measurements and CEO frequency measurements can all be used for active CEP stabilization. Most often the CEP is stabilized to a fixed value by making fast changes in the laser oscillator, e.g. by modulating the pump intensity. Alternatively, an acousto-optic modulator can be used to actively stabilize the CEP, in a so called feed-forward method [60]. On the other hand, in parametric processes the phase can be stabilized passively using nonlinear processes as shown in Chapter II.3.3. CEP stabilization can also be achieved by stabilizing the CEO frequency of the oscillator at an integer multiple of the repetition rate of the pulse picked laser. In this case, the CEP will change

shot by shot by a constant amount in the oscillator, but after the pulse picker, the remaining pulses will have close to identical CEP values, hence the result is a CEP stabilized pulse train.

II.5.1. Interferometric methods

Using the phase relations in Chapter II.3.3, self-referenced interferometric measurement methods can be better understood. These methods rely on the heterodyne detection of the CEO frequency [20]. While multiple self-referenced nonlinear schemes exist, the f-to-2f method is the most common one, where the temporal modulation between the fundamental and the generated second harmonic is measured with a photodetector, and the yielded signal can be used to determine the CEO frequency. While these temporal interferometric methods are useful for measuring the pulse-to-pulse CEP change of oscillators, they are not suitable to characterize amplified pulses. The lower repetition rate after pulse-picking means that the accurate detection of the CEO frequency is problematic. In addition, laser amplifiers exhibit considerably higher peak intensity noise compared to Kerr-lens-mode-locked oscillators [61], resulting in spurious measurement noise [62]. In this case, a secondary phase correction loop may be necessary as an amplified stage can introduce additional phase noise [62], which is otherwise left uncompensated.

To extract single-shot delocalized CEP information of amplified pulses, a modified f-to-2f interferometer was developed [63,43]. In this case, the beating between the fundamental and the generated second harmonics is recorded in the spectral domain by sending the output of the interferometer into a spectrometer. We can describe this method by using a simplified one-dimensional temporal model

$$E_\omega(t) = A(t)e^{i(\omega_0 t+\varphi_{CE})}, \tag{II-85}$$

where A(t) is the temporal envelope of the pulse, ω_0 is the central angular frequency and φ_{CE} stands for the CEP. In the frequency domain the field reads:

$$E_\omega(\omega) = A_\omega(\omega)e^{i\varphi_{CE}}. \tag{II-86}$$

Under perfect conditions, the SH pulse is centered at twice the frequency of the original. The resultant CEP is the double of the fundamental CEP shifted by an offset, as seen in Equation (II-70). The complex electric field of the SH electric field is expressed as:

$$E_{2\omega}(\omega) = A_{2\omega}(\omega)e^{i\left(2\varphi_{CE}+\frac{\pi}{2}\right)}. \tag{II-87}$$

The spectra of the fundamental and SH pulses may overlap if the spectrum is either sufficiently broad or if it is broadened by SPM, which only shifts the CEP by a constant $\pi/2$ value, as seen in Equation (II-72). The overlapping region will exhibit a spectral interference pattern, where the period of the modulation depends on the relative delay between the fundamental and the SH pulses. The resulting normalized intensity signal, as detected by a spectrometer, can be described by:

$$\begin{aligned} I_{f-2f}(\omega) &= \left(E_\omega(\omega) + E_{2\omega}(\omega)\right)\overline{\left(E_\omega(\omega) + E_{2\omega}(\omega)\right)} = \\ &= I_\omega(\omega) + I_{2\omega}(\omega) + 2\sqrt{I_\omega(\omega)I_{2\omega}(\omega)}\cos(\varphi_{CE} + \omega\Delta t). \end{aligned} \tag{II-88}$$

The third term in this equation creates a spectral intensity modulation, where the phase of this pattern is in fact equal to the CEP shifted by an offset. Thus, by extracting the phase of the

spectral modulation we can obtain the delocalized CEP value of the input pulse using the Fourier transform spectral analysis, described in detail in Chapter II.4.2.

As the single-shot f-to-2f method relies on an optical spectrometer, acquisition time is constrained by the readout speed of detector arrays, e.g., a charge-coupled device (CCD). Even with the fastest devices with custom electronics, the minimum time duration between two consecutive measurements is at least tens of microseconds. For laser systems above 10 kHz repetition rate the measured CEP is usually extracted by integrating the spectra of multiple pulses, or undersampling the pulse train, which makes pulse tagging impossible and the measured delocalized CEP unreliable. Even when replacing the detector array with two photomultipliers, which in principle mitigates this limitation, the demonstrated fastest single-shot detection was at 10 kHz [11].

II.5.2. Ionization based methods

The localized CEP value of a laser system can be measured with several techniques. For amplified laser systems with pulse energies in the millijoule range (or above) it is quite common to use the so called CEP-meter based on Stereo-ATI measurements [64–66]. In this method, the focused linearly polarized laser pulses ionize noble gas and the emitted electrons are recorded with two time-of-flight spectrometers facing each other at the plane of the polarization of the pulses. The CEP can be determined for every single pulse from the left-right asymmetry signal of fast and slow rescattered electrons. The first single-shot stereo-ATI measurement took place in 2009 [65], with a device shown in Fig. 16. This technique has recently been proven to be fast enough for 100 kHz repetition rate single-shot CEP measurements and feedback [67].

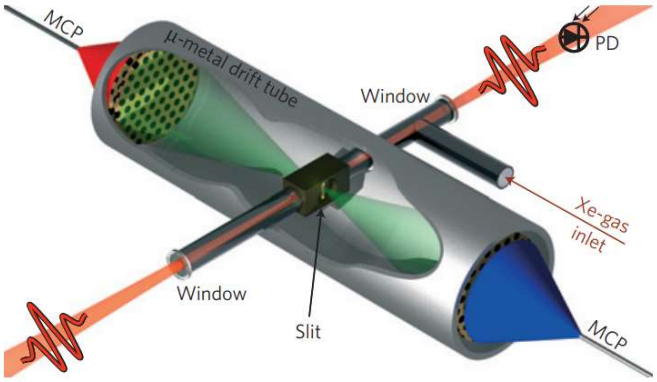

Fig. 16. The stereo-ATI phase meter from article [65]. The chamber is under high vacuum, with a xenon cell near the focus of the laser, where the atoms are ionized. The electrons are detected with a pair of time-of-flight spectrometers. MCP – microchannel plate detectors; PD – photodiode

Unfortunately, stereo-ATI is fairly demanding on the laser system as it typically requires minimum 30 μJ energy, few-cycle pulses for near-IR lasers [66]. This energy is larger or at least makes up a significant portion of the available pulse energy for most of the ~100 kHz repetition rate lasers. For mid-IR lasers the energy requirement is even more stringent because of the smaller photon energies. Additionally, it requires a chamber with active vacuum pumping and noble gas supply, making it significantly larger, more expensive and more complex compared to interferometric CEP measurement methods. New ionization based CEP detection methods are emerging using circularly polarized light to ionize noble gas [68] and air [69]. These methods are less complex compared to stereo-ATI, but they require similarly high

intensity, few-cycle driving pulses. Despite these strict requirements, this method can be used to measure the localized CEP, and it even provides information about the pulse duration on-target. To conclude this chapter, the limitations of interferometric and ionization based single-shot CEP detection methods are compared and showed in Fig. 17. The gray area on the graph represents laser systems, where these techniques cannot measure every single shot.

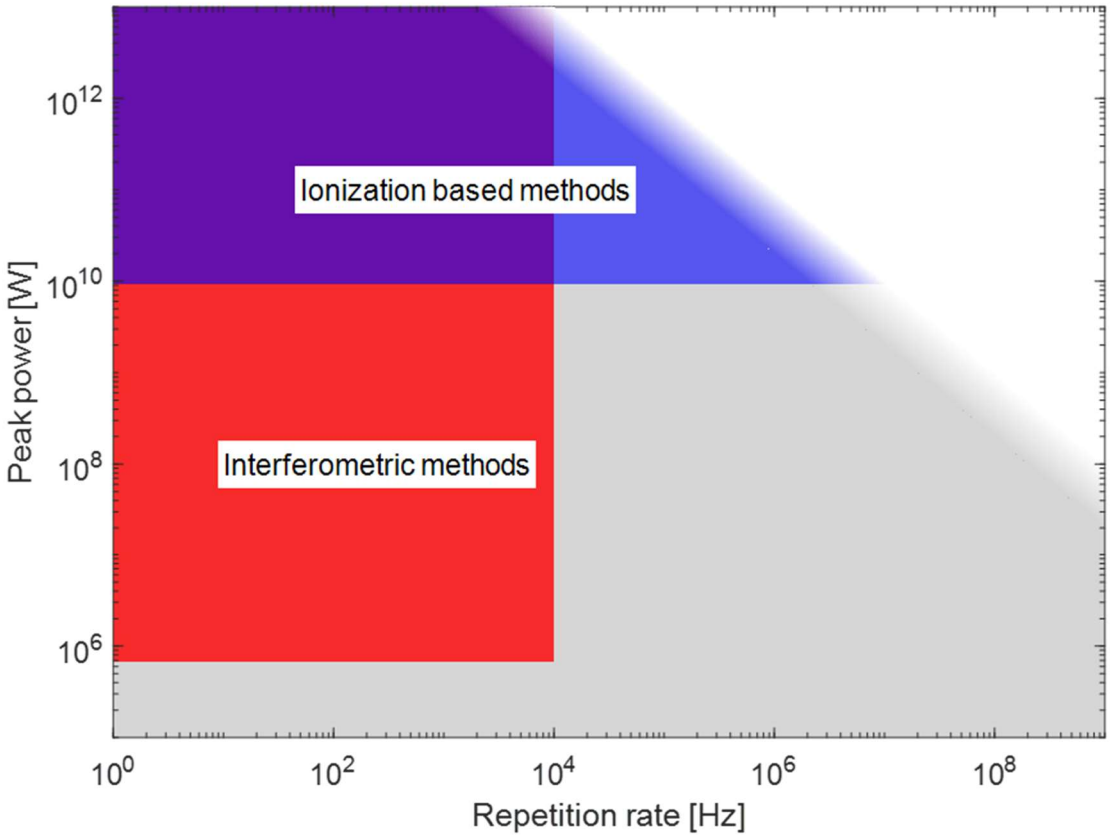

Fig. 17. Repetition rate and peak power limitations of the most frequently employed CEP detection methods. The blue and red areas represent the parameter space of laser systems, where single-shot CEP measurement is feasible by ionization based methods or interferometric methods, respectively. The purple area is the overlap between the red and blue area, where either measurement is feasible. The gray area represents those lasers systems where these methods are insufficient for single-shot CEP measurements.

II.6. Ultrafast mid-infrared systems

In the last several decades, the availability of mid-IR light sources has dramatically increased. Typical sources of mid-IR radiation include gas lasers, solid-state lasers, fiber lasers, semiconductor lasers, and sources obtained with nonlinear frequency conversion like DFG, OPA and OPO, or SCG [70]. In this chapter we would like to narrow the discussion to ultrafast (<1 ps) mid-IR (3-8 µm) laser systems. They can be divided into two categories based on how mid-IR radiation is generated, directly or indirectly. Direct sources create and amplify pulses in the mid-IR wavelength region using conventional laser amplification methods. On the other hand, indirect sources use nonlinear frequency conversion techniques like DFG and OPA to generate mid-IR pulses mostly from near-IR laser sources. These different sources and their subcategories are summarized in Fig. 18. CO and CO_2 gas lasers generate mid-IR laser radiation directly from gain in gas discharge, and they emit radiation in the 5–6 µm and 9–11 µm ranges, respectively. While they have plenty of applications in the industry, they have not been demonstrated as an ultrafast laser source so far.

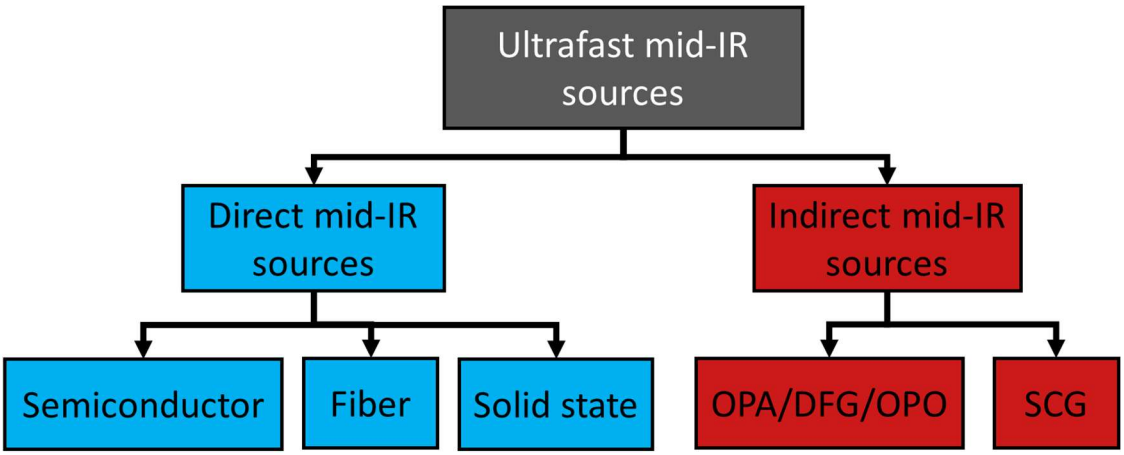

Fig. 18. Different types of ultrafast mid-IR sources

II.6.1. Direct mid-IR sources

Since the early 2000s, considerable research has been performed on direct ultrafast lasers in the SWIR and the mid-IR [71,72]. Despite these efforts, most sources generate pulses with wavelengths below 3 µm. To generate ultrafast pulses directly, mode-locked lasers are necessary. Mode-locking can be achieved in two ways: passively and actively. Active mode-locking relies on either an acousto-optic, or an electro-optic modulator synchronized with the resonator round trips. This way ~100 ps pulses can be generated. On the other hand, passive mode-locking is usually achieved by a saturable absorber placed inside the oscillator cavity, and it is capable of producing laser pulses with femtosecond pulse duration. Hereinafter only passive mode-locked femtosecond sources are considered. In the mid-IR there only a few available gain materials, and saturable absorbers are also scarce, which are the two main limiting factors for the development of femtosecond mid-IR sources [71].

We can differentiate direct mid-IR sources based on the gain material and divide them into semiconductor, fiber and solid-state lasers. Semiconductor lasers use epitaxially-grown semiconductor heterostructures electrically driven to achieve lasing. Semiconductor lasers can be further divided into quantum cascade lasers where photons are generated through

intersubband transitions (transitions between energy levels of the conduction band), and interband cascade lasers (transitions between different bands of the semiconductor heterostructure). Quantum cascade lasers are tunable and can emit an average power of several watts, but pulsed mid-IR quantum cascade lasers usually operate with pulse durations longer than 100 ns [70]. Interband cascade lasers are more favorable for pulsed operation in the mid-IR because of their longer upper-state lifetime [73]. Consequently, interband cascade lasers can reach picosecond pulse duration, which is still far from the few-cycle regime.

Rare-earth doped fiber medium is a more promising candidate for ultrafast IR laser operation. There are several rare-earth ions that are being actively researched for this task, like Tm^{3+}, Ho^{3+}, Er^{3+}, Pr^{3+}, Yb^{3+}, Nd^{3+} and Dy^{3+}. Most of these ions do not possess transitions corresponding to higher than 3 μm wavelength photons, with the notable exceptions of Ho^{3+} and Dy^{3+} ions. While the Ho^{3+} ion is mostly known as a dopant for 2 μm solid-state lasers, the ion also has a transition with a corresponding photon wavelength of 2.85–3.05 μm [72]. The host material cannot be the standard silica fiber used for telecommunications as it has a high mid-IR loss (> 2.7 μm) due to multiphonon absorption. Instead, mid-IR glasses are used for fiber manufacturing like fluorides, tellurites, and chalcogenides. These materials have lower losses in this wavelength range due to lower phonon energies. While the main application for tellurite and chalcogenide fibers are beam transportation and spectral broadening, significant advances have been made with fluoride glasses as a host material for fiber amplifier. One of the most frequently used fluoride glass materials is ZBLAN, which has paved the way for the construction of mode-locked picosecond Ho^{3+} doped ZBLAN fiber lasers emitting at around 3 μm [74]. The other promising candidate for longer than 3 μm femtosecond operation are the Dy^{3+} doped fiber lasers. The shortest pulse duration generated by such lasers is 724 fs transform-limited [75], with a pulse energy of 2.3 nJ at 3.05 μm central wavelength.

The two most commonly used solid-state mid-IR lasers are based on electronic transitions in rare-earth ions and vibronic transitions in transition metals. Rare-earth ions based solid-state mid-IR lasers use the same doping ions as fiber lasers i.e.: Ho^{3+}, and Dy^{3+}. Thus the emission spectra are the same, as the host material also has a marginal effect on the emission spectrum. Vibronic laser sources can provide much wider absorption and emission bands than rare-earth ions due to the strong coupling between the phonon and electronic states [70,72]. Vibronic sources are manufactured by doping II–VI compound semiconductors with transition metal ions like Cr^{2+} and Fe^{2+}. Cr^{2+}-doped semiconductor vibronic sources have large emission bandwidths in the 2–4 μm range and a broad absorption band centered at 1800 nm [76]. The II–VI compound host material is usually ZnSe, ZnS or CdSe. It can be pumped by various sources like Tm^{3+} solid-state laser, Er^{3+} fiber or infrared laser diodes. Kerr-Lens mode-locked operation with less than 50 fs pulse duration has been achieved, but so far only at around 2.5 μm [77,78]. Fe^{2+} doped II–VI compound vibronic laser sources can emit between 4 and 5 μm. However, the spectral absorption band of Fe^{2+} is around 2.5–4.0 μm, where pump sources are scarce [79], so it is most often performed with Er^{3+} lasers operating at 2.9 μm. Another issue is multiphonon quenching, which strongly limits the lasing capabilities of mid-IR transitions in the Fe:ZnSe crystal at room temperature. Femtosecond mode-locked operation for Fe:ZnSe has only recently been demonstrated at around 4.4 μm central wavelength with a pulse duration of 732 fs [80].

In conclusion, direct sources are highly efficient and can be used as CW and nanosecond to picosecond mid-IR sources. Unfortunately, further advancements are needed for few-cycle

mid-IR operation. Until technology improves, less efficient, but highly power-scalable indirect mid-IR sources are required for femtosecond operation.

II.6.2. Indirect mid-IR sources

Indirect mid-IR laser sources, as defined earlier, are based on nonlinear frequency conversion, most commonly on parametric processes such as DFG and OPA. These parametric processes are based on the nonlinear polarization component shown in Equation (II-54) and described in detail in Chapter II.3.1. There are several available nonlinear crystals for the three-wave mixing process. Unfortunately, BBO – as one of the most common nonlinear crystals in laser labs – does not transmit the mid-IR, but there are plenty of mid-IR transmitting alternatives, where either kind of phase-matching can be achieved. The most common mid-IR birefringent crystals where critical phase-matching can be achieved include lithium niobate (LN), gallium selenide (GaSe), silver thiogallate (AGS), silver selenogallate (AGSe), potassium titanyl arsenate (KTA), potassium titanyl phosphate (KTP), and zinc germanium phosphide (ZGP). Most common QPM crystals in the mid-IR include periodic poled lithium niobate (PPLN), periodic poled potassium titanyl phosphate (PPKTP), and orientation-patterned gallium arsenide (OP-GaAs). The transmission windows of these crystals are summarized in Fig. 19.

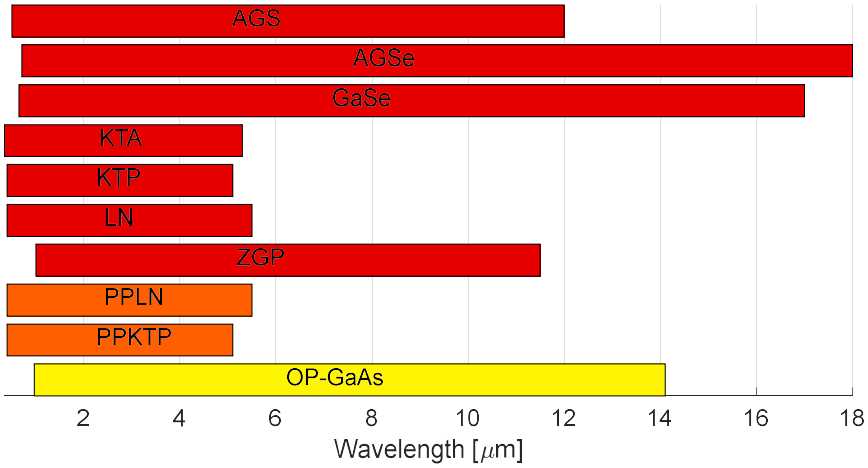

Fig. 19. Nonlinear crystals' transmission windows in the mid-IR. The red color refers to crystals which allow for critical and non-critical phase-matching. The orange color refers to crystals, where QPM can be achieved with periodic poling, the yellow color refers to crystals with QPM realized with orientation-patterning.

During the DFG process, a pump photon is annihilated and an idler and a signal photon are generated as a result. During the OPA process, seeded idler accompanies the incoming pump, and the seed wave gets coherently amplified, while signal photons are simultaneously generated. These processes provide an excellent foundation for the generation of down-converted mid-IR pulses using the most common picosecond pulse, near-IR lasers as a pump source. The main limitation of the DFG process is low efficiency, as maximum only a few percent of the near-infrared pump is converted. This issue can be overcome by dividing the pump power between several OPA stages. The seed for such an OPA chain is mostly SCG from the same pump, which circumvents the issue of electronic synchronization of multiple pump sources. After that, the idler or the signal pulses are parametrically amplified in multiple nonlinear crystals pumped by the same ps pump source [81–85].

Gérard Mourou and Donna Strickland were awarded the Nobel Prize in Physics in 2018 for the invention of the chirped pulse amplification (CPA) method [86]. The CPA based architecture allows for the energy upscaling of laser systems by stretching the ultrashort pulses to decrease their peak power prior to amplification, as high peak power can cause nonlinearities in the gain medium (such as self-focusing) or even optical damage. After pulse amplification (typically by a factor of 10^3 to 10^{12}), the pulses are recompressed close to their original pulse duration, which will result in an increased peak power compared to the original. The OPCPA process is very similar to this, but in this case the gain is parametric during the propagation of the laser through a nonlinear crystal, which is optimized (cut, thickness, coatings) for the OPA process [82]. Compared to OPA, OPCPA has larger scalability in terms of both energy and power. OPCPA systems are demonstrably capable of generating few-cycle pulses with several tens of millijoule pulse energy [83–85], at kilohertz repetition rate. The most commonly employed standard OPCPA architecture is displayed in Fig. 20.

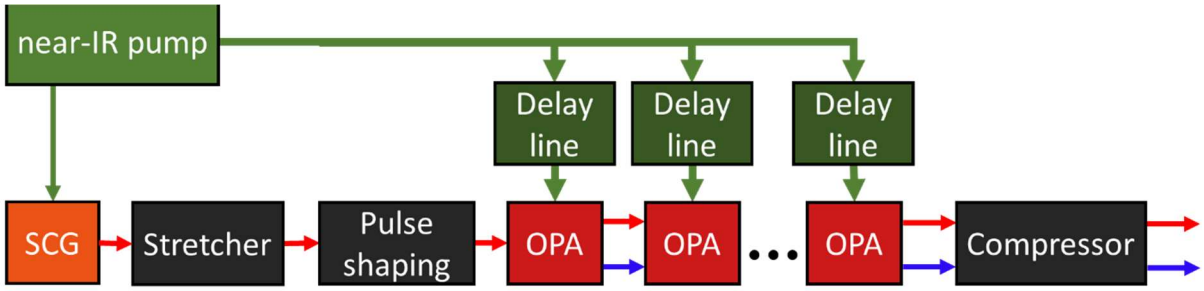

Fig. 20. Standard OPCPA architecture using a single ps pump laser. The green, red and blue arrows represent the pump, the idler and the signal beams, respectively. In each OPA stage either the idler or the signal gets amplified.

Several methods exist to stretch and compress pulses in an OPCPA: e.g.: by grating compressors [90], prism pairs [91], grism pairs, or bulk compressors. Despite the careful design of these dispersive components, which aim to handle the dispersion of an entire laser system, the compensation of higher order dispersion often requires additional pulse shapers like acousto-optic modulators or acousto-optical programmable dispersive filters (AOPDF), in order to compress pulses close to their FTL duration at the end of the OPCPA. The damage threshold of such pulse shapers may limit their utilization to low power beams, typically shaping the supercontinuum or the signal/idler after the first OPA stage.

Since in the OPA process energy exchange is an instantaneous process, unlike in CPA systems, no fraction of the pump photon energy is stored in the medium. This reduces the spatial aberrations of the beams and allows for higher repetition rate systems [44]. However, no crystal is perfectly transparent, and the residual absorption of the interacting waves can be considerable at a high average power, which ultimately limits average power scalability [87]. Furthermore, the problem with the instantaneous energy exchange is that temporal overlap must be achieved between the stretched seed and the picosecond pump, which requires an adjustable delay for the every OPA stage. An OPA stage usually contains only a single pass, but also OPAs have higher gain per pass compared to traditional gain materials. This allows OPCPAs to be more compact in size and overall less complex compared to multi-pass amplifier systems. They could also be operated at various central wavelengths with high wavelength tunability, even in the mid-IR regime, where direct ultrafast sources are less developed. The advantages and disadvantages of OPCPA systems over CPA systems are summarized in Table 2.

Advantages	Disadvantages
• Higher gain per pass • Mature technology for mid-IR • Broad gain bandwidth • Heating from pump absorption is low • Spectral tunability • Compactness	• Seed and pump laser must be synchronized • Phase-matching is needed • Limited aperture for nonlinear crystals • High pump beam quality required • Less efficient than CPA

Table 2. Advantages and disadvantages of OPCPA systems compared to CPA systems.

To achieve CEP stability, a self-seeded OPA scheme is often used, which provides passive CEP stability. However, this is not sufficient to stabilize long-term CEP drifts, so additional CEP stabilization is often employed.

II.6.3. Post-compression methods

Producing pulses efficiently with fewer than 4 optical cycles in the 3 to 4 μm spectral range remains very challenging based solely on the current OPCPA technology [9, 88–90]. The limitation is the gain bandwidth of the OPA process, which narrows the bandwidth of the amplified pulses, thus limiting the achievable shortest pulses. To generate shorter pulses, post-compression must be used, which consists of spectral broadening in a medium through the SPM process [90–101] followed by dispersion control. In the past decades, several technologies have emerged for the post-compression of laser pulses.

In the mid-IR spectral range, several noble-gas filled, hollow-core waveguide post-compression schemes have been demonstrated [91,92]. The benefit of this method is that spectral broadening can be fine-tuned by changing the gas pressure in the fiber. These fibers exhibit a total transmission of around 50% mainly due to material absorption and capillary losses, which means that the net peak power is increased only for relatively long initial pulses (>50 fs). This limitation is somewhat mitigated in antiresonant-guiding photonic crystal fibers (ARR-PCFs) [90,93], where a transmission of around 85% can be achieved. While the output provides homogenous compression, this technique has a number of disadvantages too, such as complexity, large footprint, dependence on the high pointing stability of the laser, and its overall price.

A less expensive and much simpler post-compression scheme for intense mid-IR pulses can be achieved by nonlinear broadening in solid-state media [98–101]. Here the nonlinear refractive index (n_2) is by orders of magnitude higher compared to that of the inert gases inside a hollow-core waveguide. In this method, the plate thickness usually does not exceed a few mm thickness, so even with input pulse energies orders of magnitude above the critical self-focusing limit no critical self-focusing can occur [99]. Multiple plates can be stacked after one another for increased spectral broadening. In order to decouple the spatial and spectral impact of the Kerr effect and to gain precise control of material dispersion, the application of millimeter thin nonlinear media is required. However, spectral broadening can be uneven over the beam cross section, as SPM depends on the local intensity and the intensity of the pulse is rarely

homogenous in space; it most often exhibits Gaussian or super-Gaussian spatial distribution. The uneven spectral distribution along the spatial dimensions is called spatio-spectral coupling. This can be minimized by spatially filtering the beam after the plates, by cutting the less broadened outer part, which also decreases the overall energy of the pulses.

A large compression factor can be achieved by having multiple passes through a nonlinear medium, when material dispersion is moderate. This setup can be made more compact by confining the laser into a cavity-like chamber, where mirrors focus the pulses into the nonlinear media multiple times. Even more than 100 passes can be realized with sufficiently large optics with broadband high reflection coatings to keep losses at a reasonable level. This device is called multipass cell or Herriott cell. Multipass cells have been demonstrated using bulk media [102,103] and recently noble gases [96,97] and they are promising candidates for post-compression for wide range of lasers with diverse pulse parameters. The main bottleneck of this method in the mid-IR regime is the availability of suitable mirror coatings to handle the broad spectral bandwidth, high intensity and irradiance (average power received by a surface per unit area) on the mirrors. For this reason, to the best of my knowledge, the implementation of multipass cells has not yet been presented for mid-IR wavelengths.

II.6.4. The ultrafast mid-IR laser source of ELI-ALPS

For all of the experiments discussed in this dissertation the MIR laser system [9] of the ELI-ALPS institute was used as the laser source. It is a mid-IR OPCPA, similar in architecture to the one shown in Fig. 20. The pump is a 100 kHz Yb^{3+}:YAG thin disk laser (DIRA-200, TRUMP Scientific Lasers) delivering 2 mJ pulses at 100 kHz. The pulses are compressed to 1.1 ps FWHM at 1030 nm. The seed for the OPCPA is generated by SCG in a YAG crystal. These broadband pulses are then shaped by an LN based AOPDF (Dazzler, Fastlite) [104].

LN is a popular choice for ultrafast mid-IR OPA, because it has broadband phase-matching and a high nonlinear coefficient [105]. For this reason, all the stages in the MIR laser are MgO-doped PPLN and LN crystals. Unfortunately, LN has strong OH^- infrared absorption, and the generated parasitic SH of the pump gets partially absorbed too, which can cause thermal lensing at high average power [105]. This issue is still manageable at 140 W average power of the last pumping stage in the MIR laser system using crystal ovens to mitigate parasitic SH generation.

The mid-IR pulses are first generated through DFG between the pump and the seed pulses in a MgO:PPLN crystal with a central frequency of around 3.2 μm. These passively CEP stable pulses are then amplified in one collinear MgO:PPLN OPA stage (OPA2) and two NOPA LN stages (OPA3-OPA4). Unfortunately, due to the noncollinear arrangement of the last stage, the 1.6 μm signal has angular chirp. The 3.2 μm idler pulses are compressed in an AR coated Si window, which has negative GVD at this wavelength. In normal operation, we usually have 140 μJ energy and 45 fs pulse duration at the output. In addition to the passive CEP stabilization, an active feed-forward CEP stabilization is employed using the signal of an 2f-to-f interferometer (f-to-2 interferometer with SH generation preceding the spectral broadening) and a fast spectrometer (Fringeezz, Fastlite) [106]. In the 2-f-to-f device SHG generation occurs in a type-I AGS crystal, then stable continuum is generated by focusing the beam into a YAG crystal. The error signal from the Fringeezz is sent back to the DAZZLER, making real-time phase correction in an active stabilization scheme. The resulting single-shot CEP is measured

by the same inline 2f-to-f, which yields 100 mrad CEP stability (undersampled to 10 kHz). The schematics of the OPCPA system is displayed in Fig. 21.

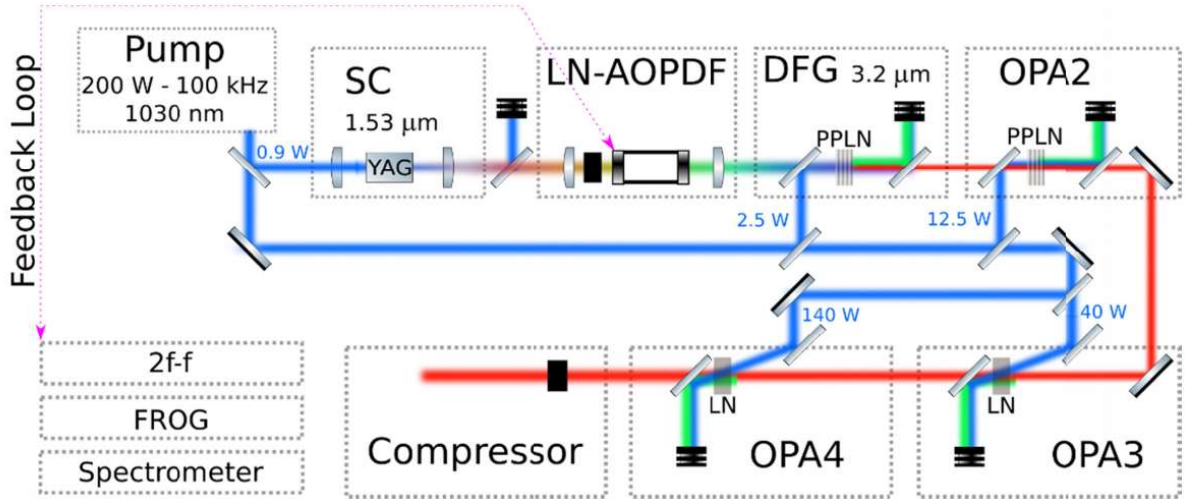

Fig. 21. The schematics of the MIR laser system of ELI-ALPS [9].

While the MIR laser system is certainly cutting-edge in terms of pulse duration and average power, there are other high power mid-IR lasers around the world with comparable laser parameters. To give an overview of its performance and compare it to other laser systems, I have summarized the current ultrafast mid-IR systems to the best of my knowledge in Table 3. I have limited the content of the table to systems with pulse durations less than 100 fs and to central wavelengths between 3 and 4 µm.

Central wavelength	Repetition rate	Pulse duration	Average power	Post-compression	Reference
3.5 µm	300 Hz	21 fs	0.014 W	Thin-plate	[100]
3.5 µm	1 kHz	31 fs	0.027 W	Thin-plate	[101]
3.4 µm	10 Hz	111 fs	0.13 W	no	[107]
3.2 µm	50 Hz	22 fs	0.125 W	HCF	[91]
4 µm	100 Hz	21.5 fs	0.206 W	HCF	[92]
3.9 µm	20 Hz	35 fs	0.26 W	N_2 gas cell	[108]
3.9 µm	20 Hz	30 fs	0.4 W	Thin-plate	[99]
3 µm	100 Hz	65 fs	0.43 W	no	[109]
3.1 µm	160 kHz	32 fs	0.48 W	Thin-plate	[98]
3.1 µm	125 kHz	72 fs	1.25 W	no	[110]
3.4 µm	50 kHz	44 fs	1.1 W	no	[88]
3.8 µm	100 kHz	79 fs	4.5 W	no	[111]
3.3 µm	160 kHz	14.5 fs	9.6 W	ARR-PCF	[90]
3.1 µm	100 kHz	73 fs	12.5 W	no	[112]
3.2 µm	**100 kHz**	**38 fs**	**15 W**	**no**	**MIR** [9]

Table 3. High power ultrafast mid-IR systems sorted by average power. The MIR laser system of the ELI-ALPS Institute is highlighted in bold font.

II.6.5. Mid-IR detectors and spectrometers

Mid-IR radiation is invisible to the human eye making any alignment difficult. But it is not only the human eye, which is unable to detect mid-IR radiation; most commercial IR viewers are

also limited to a wavelength range below 2 μm. To convert VIS and near-IR radiation to electric signals, silicon based semiconductor detectors are most often employed. On the other hand, silicon transmits mid-IR radiation, as seen in Fig. 6, preventing it to be used as a base material for detectors. Instead, narrower bandgap semiconductors (like InAsSb, or HgCdTe compounds) are often employed. As mid-IR semiconductor detectors are based on a relatively new technology compared to the well-established silicon based devices, production costs are generally higher. Furthermore, they often need to be cooled in order to provide the necessary sensitivity, which complicates the measurement process. Therefore, usually only single chip detectors are available commercially.

An alternative method for the detection of mid-IR radiation is achieved by thermal detectors. Here radiation gets absorbed on a blackened surface, which results in a rise in temperature. The spectral response of these detectors can therefore be as flat as the absorption spectrum of the absorptive element [113]. There are several devices based on this principle: pyroelectric detectors, and thermocouple receiver depending on how the temperature is converted to electric signal. Pyroelectric detection is most suited for cameras, as they can be operated at room temperature and even hundreds of mW of input power can be measured with them. Unfortunately, such cameras are expensive, and pixel sizes are limited to tens of μm, limiting the available resolution. An example is the Pyrocam IIIHR Beam Profiling Camera [114].

Building spectrometers for broadband mid-IR radiation is even more challenging than simple detection. In addition to all the previously mentioned detection problems, the gratings – vital components in most spectrometers – are either too narrow-band or have low efficiency at the mid-infrared range. Fourier transform infrared spectrometry (FTIR) [15] is a linear method aimed to overcome this problem. The basis for this detection type is a Michelson interferometer, which can be seen in Fig. 12. b. The measured beam is separated into two parts, one of which is delayed and then re-combined with the other part at a detector. By moving the delay, time domain interference can be created, and the FT method allows for the recovery of the original spectrum. In practice, the bandwidth of the measurement is limited only by the sensitivity of the detector and the bandwidth of the optics in the interferometer. Unfortunately, artifacts can emerge in the reconstructed spectrum for broadband pulsed sources, because of synchronization issues [115]. Alternatively, a triggered acousto-optic device can be used to disperse the pulses in time, and record it with a photodiode. In this case the spectrum can be recovered from the temporal signal of a photodetector, similarly to FTIR spectrometers. Such a device (MOZZA, Fastlite) [115,116] is employed for measuring the spectrum of the pulses of the MIR laser at ELI-ALPS.

III. New scientific results

III.1. Single-shot CEP detection with the TOUCAN method

Measuring the CEP of every single pulse of a high repetition rate amplified pulse train is a non-trivial task. Chapter II.5.1. summarizes the current CEP detection techniques for amplified lasers and their requirements. There I point out that interferometric methods require much lower peak power and can even use longer than few-cycle pulses for detection compared to ionization based methods. Until now, the main acquisition time bottleneck for these interferometric methods was the readout speed of spectrometers, which limited single-shot detection to a repetition rate below 10 kHz. The TOUCAN (**T**emporal dispersion based **O**ne-shot **U**ltrafast **C**arrier envelope phase **AN**alysis) technique also utilizes interferometric CEP detection, but it can reach a much higher data acquisition rate by eliminating its dependence on optical spectrometers. Instead, the technique utilizes dispersive Fourier transform (DFT) [117,118], which allows for spectral measurement with a single photodetector.

DFT is a phenomenon, which occurs when a laser pulse suffers high level of dispersion, and it stretches the pulse by orders of magnitude longer compared to its original pulse duration. The resulting temporal shape of the pulse will depend on the original spectral intensity distribution. The reason for this is quite straightforward: during the dispersion process, different frequency components travel at different phase velocities, accumulating different time delays. The time delay optical frequency function can be expressed using the far field approximation [118] and arrive at the expression

$$\mathrm{I}\big(\mathrm{T}(\omega)\big) = \mathrm{I}(\mathrm{GD}(\omega_0) + \mathrm{GDD}(\omega_0)(\omega-\omega_0) + \\ +\frac{1}{2}\mathrm{TOD}(\omega_0)(\omega-\omega_0)^2 + \frac{1}{6}\mathrm{FOD}(\omega_0)(\omega-\omega_0)^3 + \cdots), \qquad \text{(III-1)}$$

where I is the temporal intensity function, ω is the angular frequency, ω_0 is the central angular frequency, GD, GDD,TOD and FOD are the phase derivatives discussed in Chapter II.2.2, and T is the accumulated time delay of the laser pulse traveling through the medium. This Equation shows that at a high level of dispersion the resulting temporal shape is independent from the original temporal shape. Instead it depends on the original spectral shape and the dispersion of the medium. We can make further simplifications by only considering GD and GDD and neglecting all higher order dispersion

$$\mathrm{I}\big(\mathrm{T}(\omega)\big) = \mathrm{I}(\mathrm{GDD}(\omega_0)\omega + \mathrm{GD}(\omega_0) - \mathrm{GDD}(\omega_0)\omega_0) = \mathrm{I}(\mathrm{A}\omega + \mathrm{B}), \qquad \text{(III-2)}$$

where A and B are constant parameters. This shows that the spectral components of intensity are linearly mapped to the temporal domain, making this physical process analogous to Fourier transform.

Using DFT, the output spectrum of an f-to-2f interferometer can be mapped into the temporal domain. This creates CEP sensitive temporal interference. Even a single pulse can generate signal, and thus allow for single-shot detection. If the spectral modulation is transformed into a temporal waveform with tens of nanosecond duration, the temporal modulation can be detected with a relatively slow photodetector. One can conclude that a longer pulse duration is

preferable, but at long pulse durations these temporal waveforms can overlap in time, which limits the maximum repetition rate the device can detect without any issue.

The most convenient way to determine the CEP from this signal is to digitize it by an analog-to-digital (A/D) converter with a bandwidth at least twice the modulation frequency. In this case the CEP can be extracted from the phase of the digital waveform, using Fourier transform spectroscopy detailed in Chapter II.4.2, or to increase the speed of the calculation a simple maximum finding algorithm can also be employed. The phase detection of the photodetector signal can also be achieved with analog circuitry. In this case the only limitation for the repetition rate is the overlap of temporal waveforms and the photodetector bandwidth. In theory, this allows the TOUCAN method to be applied even for laser oscillators, because some photodetectors operate at multiple tens of GHz repetitions rates. As a result, the TOUCAN method can be used for single-shot CEP detection for a wider range of lasers than with any other previous method, which is illustrated in Fig. 22. Compared to Fig. 17 we can see that the TOUCAN method can be used for any laser system, where ionization or standard interferometric methods are already available, and even for some high repetition rate systems, where neither of them can be used.

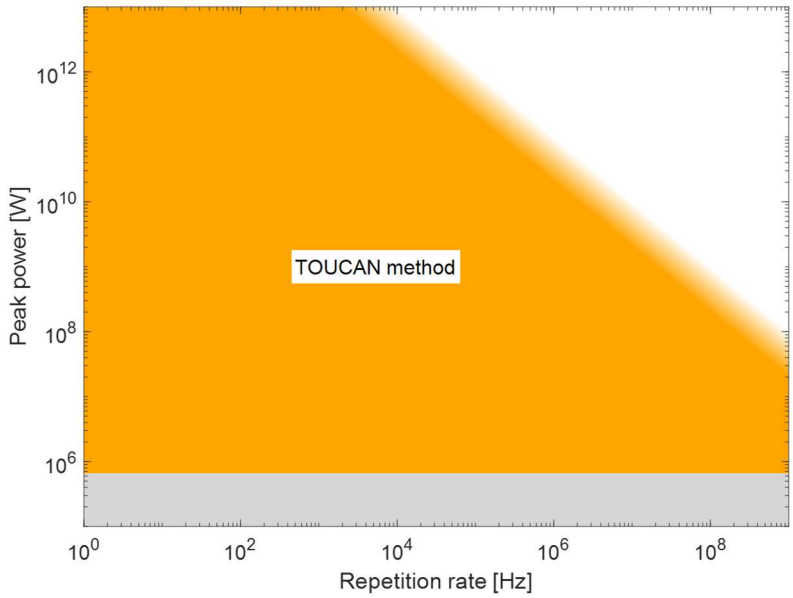

Fig. 22. Repetition rate and peak power limitations of the TOUCAN method. As the TOUCAN method can reach even GHz repetition rates, in the plotted parameter space it is only limited by the peak power necessary for the nonlinear processes.

III.1.1. Experimental setup demonstrating the TOUCAN method

The TOUCAN method was first demonstrated on the MIR laser system described in Chapter II.6.4 and shown in Fig. 21. As mentioned there, Dazzler an LN based AOPDF is used to fine-tune the temporal shape of the pulse, modify the spectral amplitude and control the phase. The CEP of the output pulses can be stabilized by sending 5 µJ of the compressed output to the Fringeezz, a commercial CEP measurement device, which creates a feedback signal for the Dazzler. Although this device contains an ultrafast spectrometer, the single-shot CEP measurement cannot exceed the 10 kHz repetition rate, which means the CEP measurement is undersampled, due to skipping 9 out of every 10 pulses of the 100 kHz pulse train. Fringeezz was used for calibration and cross-checking purposes, but it can be also used to stabilize the CEP.

Another 5 µJ fraction of the compressed output of the OPCPA was sent to the TOUCAN setup. The experimental arrangement contains an identical 2f-to-f interferometer and a DFT based measuring system capable of this single-shot CEP drift measurement. This consists of a 1.88 km long dispersive fiber (FSC-DCM-014D, OFS/Lucent), which maps the spectral modulation into the temporal domain, and an InGaAs amplified photodetector (DET01CFC, Thorlabs) for detection. The temporal waveform was digitized by the A/D converter of a 600 MHz oscilloscope (RTO2004, R&S). The experimental arrangement and the TOUCAN technique with all of its components are displayed in Fig. 23.

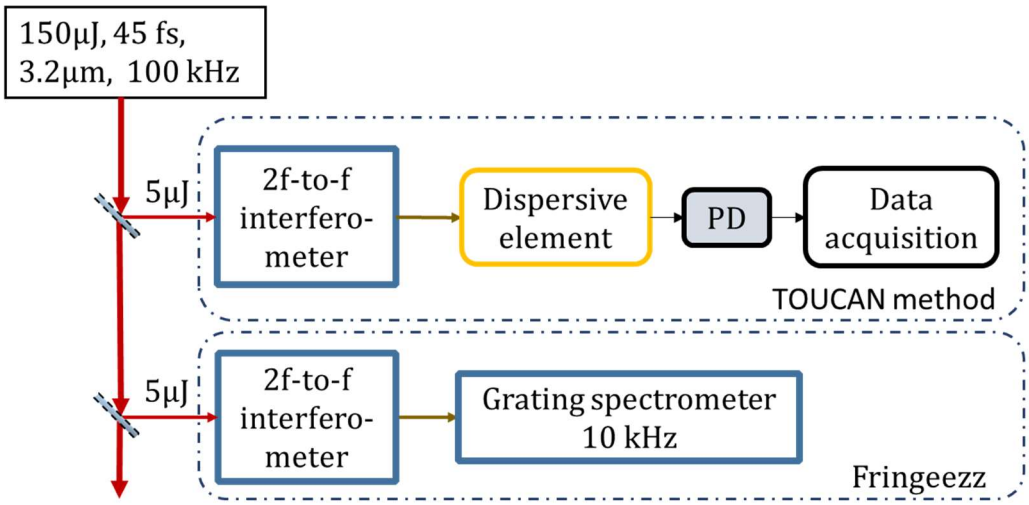

Fig. 23. Experimental arrangement used for verifying the TOUCAN technique. It contains the TOUCAN based single-shot CEP measuring device and the Fringeezz, a grating spectrometer used for cross-checking. PD – photodetector.

The oscilloscope was operated in the segmented memory mode (ultra segmentation), which allowed for the single-shot recording of every waveform at 100 kHz [119]. While the segmented memory mode allows for the fast recording of the waveform, no real-time evaluation was possible, so it was done after the measurement. The oscilloscope can be replaced with dedicated electronics, which would allow for real-time evaluation, and the generation of a feedback signal for CEP stabilization. Such a device is currently in development at ELI-ALPS, based on a field-programmable gate array (FPGA) circuit with 4 GSPS 12-bit AD converters. This FPGA will allow real-time data processing and data logging.

To align the injection into the single mode dispersive fiber, we used a high resolution optical spectrum analyzer (AQ6375 B, Yokogawa). Once spectral interference was detected at the output of the fiber, the CEP sensitivity was established by changing the actively stabilized CEP setpoint via the Fringeezz software. The recorded spectral modulation patterns for different delocalized CEP are shown in Fig. 24. The pattern is linearly shifted with the CEP value as predicted by Equation (II-88). We can approximate the time delay between the interfering pulses to be 178 fs based on the spacing of the interference.

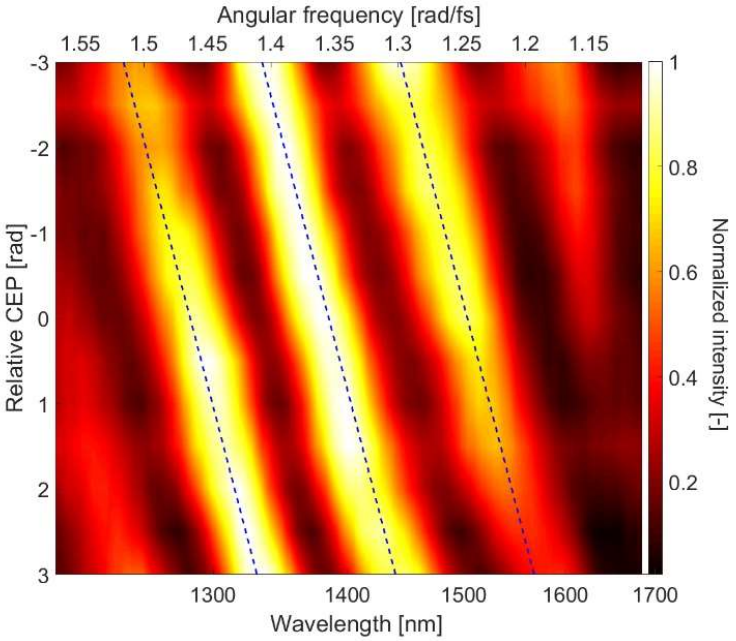

Fig. 24. The 2f-to-f spectral interference pattern recorded with an optical spectrum analyzer for different delocalized CEP values. The dashed lines are the results of linear fitting on the spectral fringe maxima, which shows the linear relation between the CEP and the phase of the interference. [120]

III.1.2. Dispersion characterization of the fiber

The laser pulse stretched by the fiber to ~100 ns long temporal waveforms measured by the photodetector and oscilloscope, also contained CEP sensitive modulation, as predicted by Equation (III-1). The calibration of the DFT technique requires characterization of the fiber dispersion, to be able to map the recorded temporal waveform to the original spectral interference. Although linear approximation can be used to determine the phase from the temporal modulation, for precise calculations higher order dispersion parameters of Equation (III-1) are required. Several methods exist to measure fiber dispersion, most of which are based on interferometric techniques like the ones described in Chapter II.4.1. However, in this experiment, dispersion was measured by comparing the spectral and temporal distribution of a modulated signal and by calculating the parameters of Equation (III-1). The ideal dispersion measurement would use the DFT signal of a dense interference (> 50 modulations) in the fiber and compare the temporal waveform recorded with the photodetector and oscilloscope with a measured spectral intensity distribution. As such dense interference was not available, we used the 2f-to-f interference roughly containing 4–5 modulations. To increase the effective density, multiple measurements were performed at different set CEP values, which shifted the maxima of the spectral interferences. Altogether 13 different CEP values were set, equidistantly distributed between $-\pi$ and π by stabilizing the CEP with Fringeezz. The spectrum was measured with the optical spectrum analyzer and with the photodetector at the exit of the fiber, and both measurements were low-pass filtered during post-processing to mitigate high frequency noises. The CEP sensitive modulations had relatively low frequency (~67 MHz), which means that it was resolvable with the both the photodetector and the A/D converter of the oscilloscope. Furthermore, the bandwidth of commercially available RF coaxial cables used for connecting the photodetector with the oscilloscope is much higher than this frequency.

To determine the dispersion parameters, we used an iterative algorithm. First, the initial dispersion parameters (GD, GDD, TOD, FOD) were initialized, which was used to calculate

the original spectrum from the recorded photodetector temporal signal. Then the resulting calculated spectrum was compared to the spectrum measured by the optical spectrum analyzer. The difference between the two spectra was used as a fitting error, which was subsequently minimized by changing the dispersion parameters with the algorithm presented in Fig. 25. The defined fitting error contained the comparison of 13 datasets, all of which were measured by both the spectrometer and the photodetector, and were recorded at different CEP values.

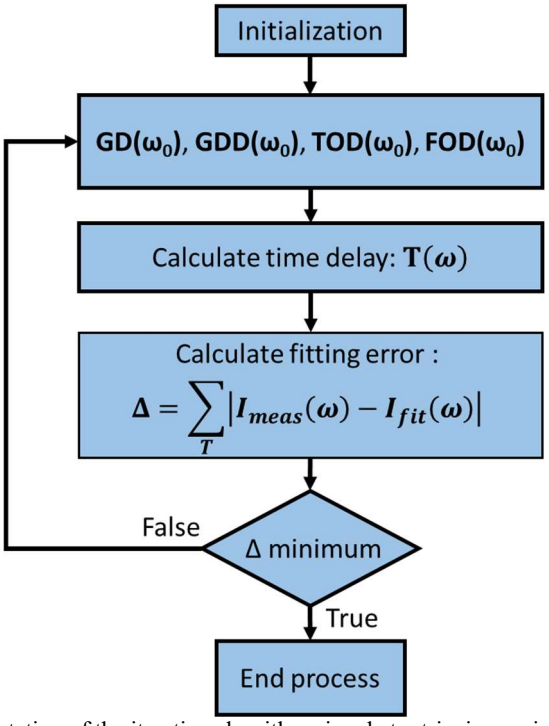

Fig. 25. Schematic representation of the iterative algorithm aimed at retrieving various dispersion orders. [120]

The result of the iterative algorithm at the best fitting determined the dispersion coefficients, which had the following values: GDD is 432.7 ps^2, TOD is –0.537 ps^3 and FOD is –0.0084 ps^4. The contribution of FOD and the higher order dispersion proved to be marginal and it was neglected in the time delay calculations. Even so, Equation (III-2) proved to be insufficient to precisely characterize the dispersion of the fiber, so instead Equation (III-1) was used up to the TOD coefficient. The time delay function retrieved by the iterative algorithm is plotted in Fig. 26. Fiber dispersion is usually characterized by the dispersion parameter, which linearly relates to the GDD. The following equation can be used to calculate the dispersion parameter

$$D(\lambda) = -\frac{2\pi c}{\lambda^2} GDD(\omega)\,. \qquad \text{(III-3)}$$

The dispersion parameter of the dispersive fiber at 1550 nm is –340 ps/nm according to the manufacturer, while calculating it from the fitting parameters results in –339.3 ps/nm, which validates the dispersion measurement method. The dispersion parameter calculated from GDD was also plotted in Fig. 26, together with the dispersion parameter provided by the manufacturer.

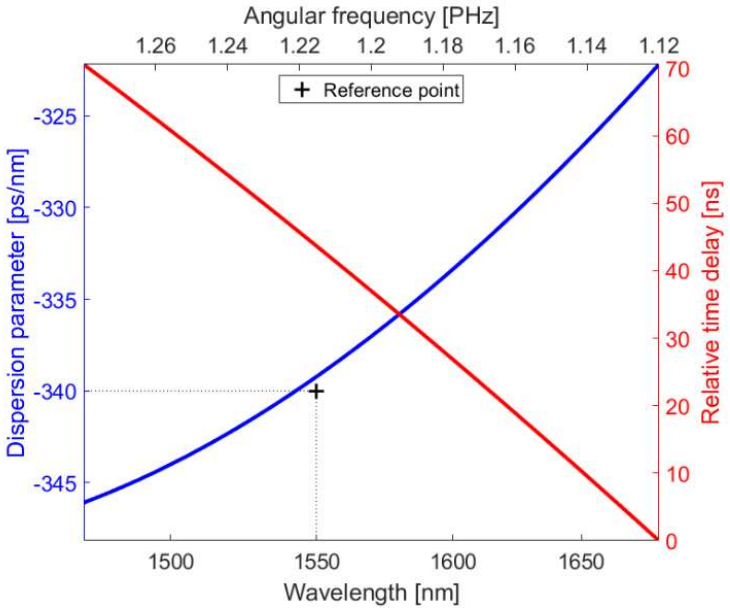

Fig. 26. Retrieved time delay as the function of the angular frequency (red) and the corresponding dispersion parameter (blue) for the FSC-DCM-014D fiber. The black cross is the dispersion parameter provided by the manufacturer. [120]

Using the dispersion curve determined by this iterative algorithm, we can compare the overlap between the temporal waveform and the spectral modulation on the same graph. The fiber has positive GDD at the central wavelength of the pulse so the temporal waveforms are reversed when compared to the spectrum, if the spectrum is plotted as a function of wavelength. With the wavelength axis on the bottom and the time delay axis reversed on the top, the overlap between the temporal waveform and the spectral measurement can be observed in Fig. 27.

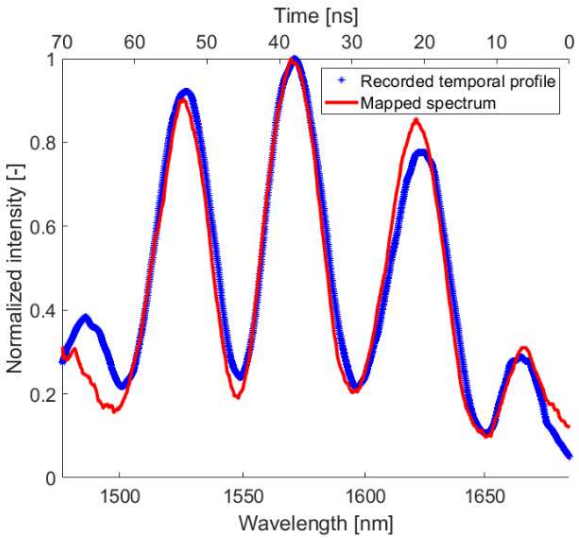

Fig. 27. 2f-to-f interference pattern used to determine the dispersion of the fiber. Superimposed are the temporal waveform recorded with a photodetector and digitalized by the oscilloscope plotted with a reversed time axis and the spectrum recorded with an optical spectrum analyzer. [120]

There is one thing left to consider, that is the temperature dependence of the fiber dispersion. As temperature changes, the refractive index of the fiber changes with it. As we have seen in Equation (II-40), the spectral phase and consequently dispersion depends on the refractive index. The temperature dependence of dispersion was not measured by the manufacturer of the fiber, and in the absence of an apparatus to perform such a measurement I used approximation. It was shown by Kato et al. [121] empirically that the temperature dependence of dispersion

relates to the wavelength dependence of dispersion by a constant factor. This can be expressed as

$$\frac{\partial D(\lambda,T)}{\partial T} = C\frac{\partial D(\lambda,T)}{\partial \lambda}, \tag{III-4}$$

where D is the dispersion parameter, and C is the constant factor ~ –0.028 nm/°C. It was shown [121] that this relation holds for widely different fibers, including dispersion-compensating fibers. For the fiber used in our measurements the temperature derivative of dispersion can be approximated to be 0.0015 ps/nm/km/°C from the dispersion curve. We can approximate how much relative error is created by the temperature change inside a laboratory, with the following equation

$$\Delta D = \frac{\partial D(\lambda,T)}{\partial T}\Delta T\,. \tag{III-5}$$

In the laboratories of ELI-ALPS, temperature values are stabilized within 1°. In these conditions, dispersion would only have a relative error of 0.0008%. Even in extremely unstable circumstances, when temperature changes within a range of 50 °C, during measurements the relative error of dispersion would only amount to 0.041%. This source of error can be safely neglected compared to other sources of errors, which are described in Chapters III.1.4 and III.1.5.

III.1.3. Delocalized CEP measurement with TOUCAN

The delocalized CEP of the pulses is measured with the TOUCAN method according to Fig. 23, single-shot at 100 kHz (the full repetition rate of the laser) and compared to the single-shot 10 kHz under-sampled Fringeezz measurement with the active CEP stabilization of the laser system turned off. The measurement time was limited to 1 second by the internal memory of the oscilloscope. Yet, thanks to the high repetition rate, this corresponds to 100,000 pulses, plenty enough for statistical analyses. The two datasets gathered by the two independent devices had to be synchronized. This was achieved by the Dazzler effectively cutting the seed for the OPA stages for a few milliseconds. As no seed was present for the OPCPA for a short time duration, the signal for both the Fringeezz and the TOUCAN devices disappeared, which facilitated synchronization between the recorded datasets.

To determine if the two synchronized datasets correlate, the 100 kHz TOUCAN measurement dataset needs to be decimated [122] or, as commonly known, down-sampled, and the matching 10 kHz subset of data must be found. There are ten possible subsets of data, out of which the closest match with the Fringeezz dataset has to be chosen. The Pearson correlation coefficient is not adequate to characterize matching between two phase values, as it does not take into account the wrapping issue arising from the circular algebraic properties of the phases. A wrapping issue occurs when a phase value steadily increases and after reaching the value of π, it wraps to the negative values just above $-\pi$, creating the illusion of a phase jump. If one of the datasets undergoes wrapping and the other one does not, it creates negative contribution for the Pearson correlation coefficient between the datasets. Therefore, to determine the level of matching between two sets of data I used the circular correlation formula [123]

$$R_{circ\_cor.} = \frac{\sum_{i=1}^{n}\sin(\alpha_i - A)\sin(\beta_i - B)}{\sqrt{\sum_{i=1}^{n}\sin^2(\alpha_i - A)\sum_{i=1}^{n}\sin^2(\beta_i - B)}}, \tag{III-6}$$

where α_i and β_i are both sets of circular algebraic data, while A and B are circular means [124] of the α_i and β_i datasets, respectively. The $R_{circ\_cor.}$ circular correlation coefficient value can take a value between –1 (anticorrealtion) and 1 (correlation). It is important to note that if the deviation of the CEP from its circular mean is small, it can be approximated by the Pearson correlation coefficient of the unwrapped phase, and despite its shortcomings, it is the most frequently used method in literature.

Using the circular correlation formula, I calculated matching between the Fringeezz data and the ten possible decimated TOUCAN datasets. The recorded datasets, which I also used for all evaluations, showed that out of the ten possible decimated TOUCAN datasets the second highest correlation coefficient reaches only 0.491, compared to the 0.982 at the maximum, which is shown in Fig. 28. This big difference between the maximum correlation compared to the other nine possible options appeared during all measurements consistently, allowing for the selection of the matching data subset reliably. It is a further proof that the TOUCAN method measures the progression of the delocalized CEP similarly to Fringeezz. Henceforth, the down-sampled data subset with the highest circular correlation coefficient will be referred to as the decimated dataset, and it will be used in all later evaluations and comparisons.

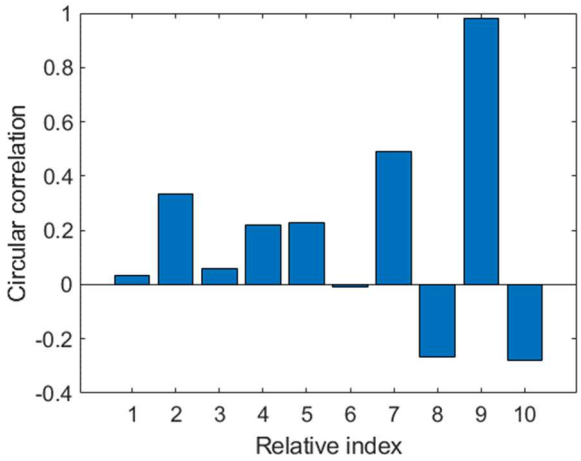

Fig. 28. Circular correlation coefficients between the Fringeezz delocalized CEP dataset and the ten possible decimated (10 kHz) CEP data subsets measured by the TOUCAN method. In this measurement, dataset 9 has the closest matching with the Fringeezz dataset. [120]

Although the correlation between datasets was high, it is important to compare the calculated delocalized CEP noise, which is most often expressed with the standard deviation of the datasets. The values are summarized in Table 4. It is important to note that the noise calculated from a decimated data subset is not equivalent to that calculated from the 10 kHz low-pass filtered data [122]. After the decimation process, high-frequency noise contributions are aliased. Aliasing means that if a high frequency signal is undersampled, the noise appears as a lower frequency replica (alias). Consequently, decimation can cause a deviation in the noise level, but the overall change is not significant, which can also be observed in Table 4.

Fringeezz (stabilization off)	TOUCAN decimated	TOUCAN 100 kHz
341 ± 5 mrad	351 ± 52 mrad	350 ± 52 mrad

Table 4. Measured CEP noise by both the TOUCAN method and the Fringeezz device when CEP stabilization was turned off, with the TOUCAN decimated CEP noise also shown.

The measurement data of Fringeezz shows a somewhat smaller CEP noise than the TOUCAN method. The uncertainty of the Fringeezz measurement is reported by the manufacturer to be 5 mrad, and it originates from the spectral resolution of the grating spectrometer. The uncertainty in case of the TOUCAN method originates from the temporal resolution of the recorded waveforms, but it is partly affected by time jitter between the trigger and the recorded temporal waveform, which is shown in Fig. 29. The timing system of the MIR laser provides 100 kHz TTL signals synchronized with the laser pulses, as it is triggered from the master oscillator of the laser system. This TTL signal is used to trigger the recording of the oscilloscope during the experiment. As it can be seen in Fig. 29, the time jitter between the laser pulse and the TTL signal will be detected as spurious phase noise. The standard deviation of this time jitter is 126 ps, which is equal to 48 mrad CEP noise.

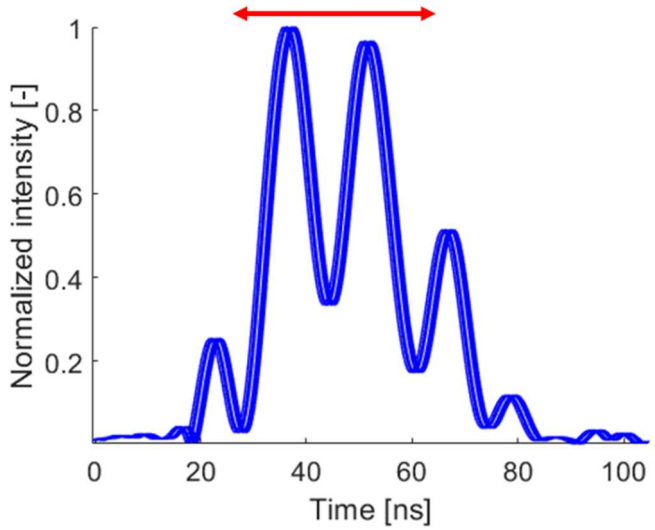

Fig. 29. The effect of time jitter between the trigger and the recorded temporal waveforms.

The resolution of the oscilloscope was set to 100 ps, to conserve the memory and increase measurement duration. A dedicated electronic with real-time evaluation could relax this limitation even more. In this case the resolution would stem from the bandwidths of the photodetector, the RF cable and the A/D converter. The frequency to time mapping is not perfectly linear as we have seen in the previous chapter. This means that temporal resolution and phase resolution vary at different times in the waveform. To give an example, the CEP resolution ranges from 33 to 43 mrad along the time domain of the recorded waveform. Where the CEP value is extracted roughly at the center, it is 38 mrad which is used in the uncertainty calculations. Using the conventional error propagation formula, the combined random uncertainty can be calculated by taking the root sum of squares of the two uncertainties (time jitter and time resolution).

To validate that the TOUCAN method and Fringeezz device measure the progression of the same physical parameter i.e.: delocalized CEP, on their own, both the noise comparison and correlation are insufficient. The CEP noise of two datasets can be identical even if the underlying data are uncorrelated. In addition, the circular correlation coefficient can be also high, yet the CEP noise can be very different. This can occur if the measured CEP is doubled due to incorrect calibration of one of the devices. In this case correlation would be close to one, but the CEP noise would be double for the multiplied dataset. A high circular correlation coefficient and a similar level of CEP noise together is a good indication, but to further validate

the TOUCAN technique, linear fitting was performed on the scatter plot of the corresponding measured CEP datasets seen in Fig. 30. The slope indicates the relative magnification of the measured delocalized CEP values. If the slope significantly differs from 1, it can mean that one of the two devices was incorrectly calibrated. As the slope of the linear fitting was 1.01, and we saw a high correlation between the dataset and independently performed CEP measurement, proper calibration can be confirmed.

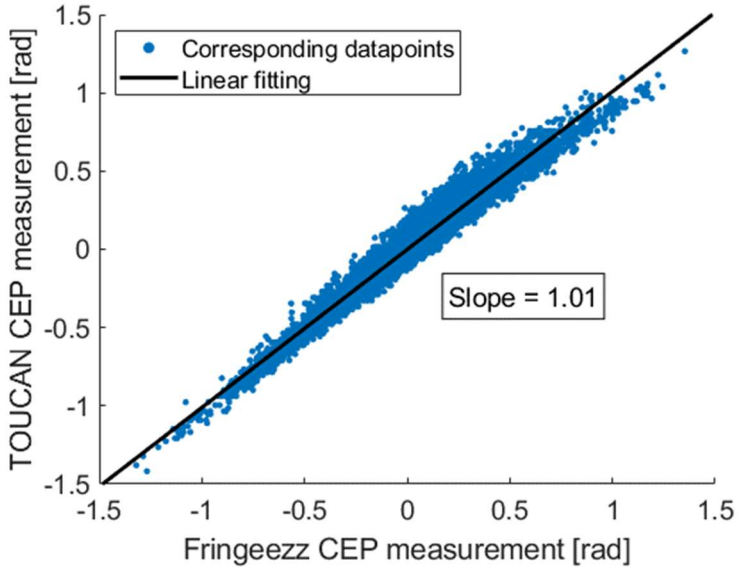

Fig. 30. The correlation of CEP data measured by the undersampled Fringeezz device and by the TOUCAN technique without CEP stabilization turned on. Linear fitting with a slope of 1.01 is displayed with continuous black line. [120]

The spectrum of the recorded CEP noise was also analyzed by calculating its power spectral density (PSD) and the integrated phase noise (IPN). The PSD is essentially the squared absolute value of the fast Fourier transformed function calculated only for positive frequencies, and it was used to analyze the most common resonant frequencies which occur in the temporal signal

$$\mathrm{PSD(f)} = \left|\mathrm{FFT}\left(\mathrm{I(t)}\right)\right|^2. \tag{III-7}$$

The numerical integration of the PSD function from the Nyquist frequency (the sampling rate divided by two) up to frequency f, generates the IPN discreet function

$$\mathrm{IPN(f)} = \sum_{\mathrm{f'}=\mathrm{f_{Nyquist}}}^{\mathrm{f}} \mathrm{PSD(f')\Delta f'}. \tag{III-8}$$

The IPN at the lowest frequency is the numerical integral of the complete PSD function, which results in the same standard deviation CEP noise shown in Table 4. The PSD of the TOUCAN CEP noise is plotted without decimation at the full repetition rate of 100 kHz in Fig. 31 (a). The PSD calculated from the decimated TOUCAN dataset and the Fringeezz measurement, both at 10 kHz repetition rate, is plotted in Fig. 31 (b). In Fig. 31(b) the two PSD functions almost completely overlap over the entire range and they possess the largest spikes at the same frequencies, further validating these results. The Nyquist frequency is the largest frequency where the PSD is defined. It can be also seen that the PSD distribution is different for the 100 kHz TOUCAN measurement shown in Fig. 31 (a). This is caused by the aliasing mentioned earlier, as the actual noise components above 5 kHz (Nyquist frequency for the 10 kHz sampling rate) are folded into low frequency aliases for both the undersampled Fringezzz and the decimated TOUCAN datasets [122].

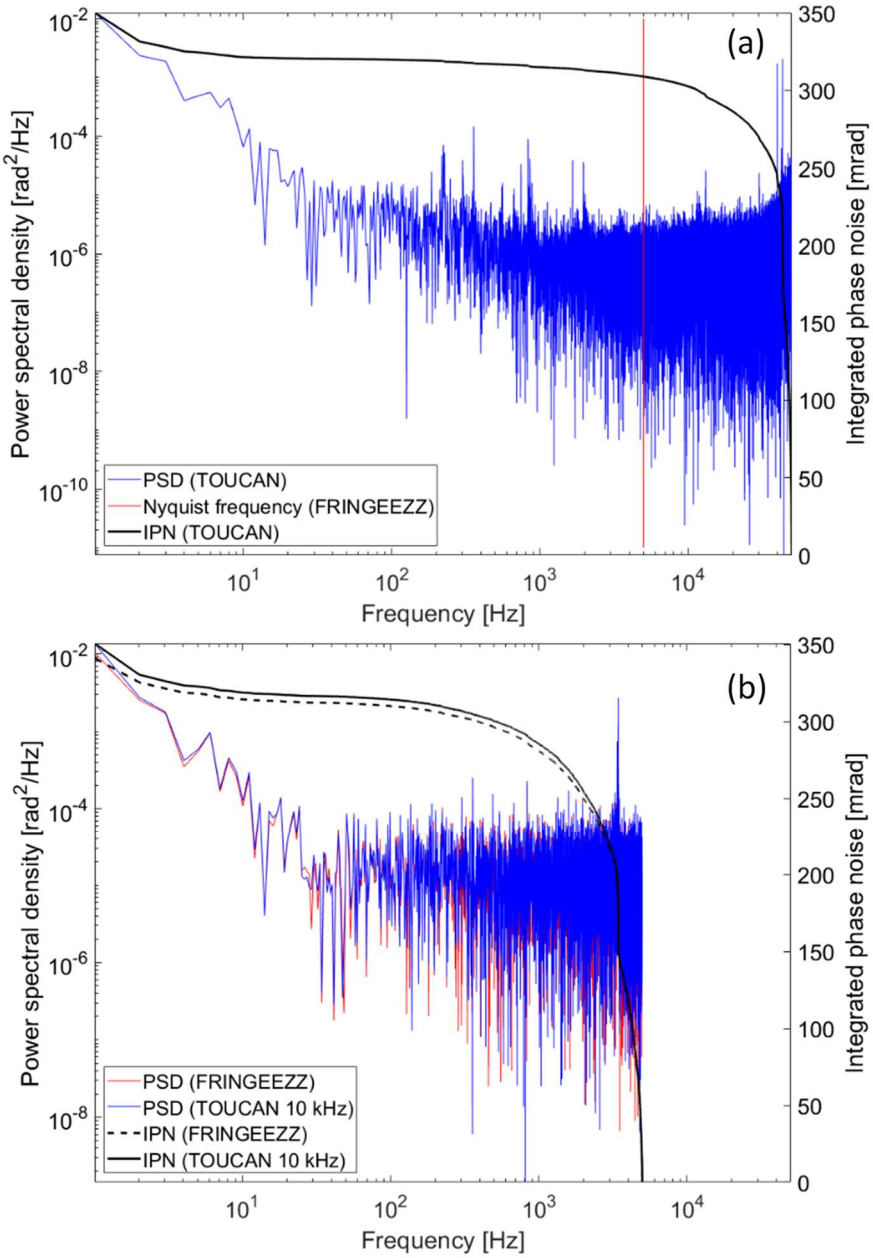

Fig. 31. (a) The PSD function of the delocalized CEP measured with the TOUCAN method at 100 kHz (blue line), and the corresponding IPN (black line). The Nyquist frequency of the Fringeezz is also displayed (red line). (b) PSD of the CEP measured with the TOUCAN method and decimated to 10 kHz (blue line), and the corresponding IPN (black line). PSD measured with Fringeezz at 10 kHz (red line), and the corresponding IPN (dashed black line). [120]

The analysis of the IPN shows that most contributions to the CEP noise stem from the resonance below 10 Hz (slow drift) and above 5 kHz. A longer measurement time would have probably yielded even more significant contribution to the slow drift. Any CEP stabilization scheme can only cancel noise up to the Nyquist frequency of the measurement. The current feedback system for the MIR system relies on the Fringeezz. As a consequence, the high frequency noise components between 5 kHz and 50 kHz are left unmitigated, even though the IPN function calculated from the 100 kHz TOUCAN measurement reaches 88% of the full integral between these frequencies. In theory, these noise components could be compensated with a 100 kHz TOUCAN based feedback-loop.

When the same device is used for active CEP stabilization and CEP measurement (in-loop measurement), the noise that emerges during detection is masked by noise stemming from stabilization [125]. For this reason, it is usually preferred to have separate devices for CEP stabilization and measurement if possible (out-of-loop measurement). In our laboratory we had two working 2f-to-f arrangements instead of three, which prevented us from making out-of-loop comparison while the laser was CEP stabilized. For this reason, we had to turn off the CEP stabilization during measurements, as I have mentioned earlier. We performed in-loop measurements too with the active CEP stabilization turned on using the Fringeezz, which resulted in a lower correlation between the recorded data (R_{circ_cor}=0.9) and high deviation between the measured CEP noises, as it can be seen in Table 5.

Fringeezz (in-loop measurement)	TOUCAN decimated	TOUCAN 100 kHz
111 ± 5 mrad	191 ± 52 mrad	187 ± 52 mrad

Table 5. CEP noise measured both by the TOUCAN method and the Fringeezz device, with the decimated TOUCAN measured CEP noise also shown. The CEP was actively stabilized with the Fringeezz signal.

III.1.4. Time jitter compensation

In the previous chapter the effect of time jitter on the measured phase was explained. To mitigate the impact of time jitter, alternative trigger sources were considered. Unfortunately, mid-IR photodetectors in the laboratory were not fast enough for this purpose. Instead the very same SWIR InGaAs photodetector was used, which detects the TOUCAN signal after the DFT. To avoid any unnecessary beam splitting and the accompanying signal reduction, a Fabry-Pérot etalon (uncoated 100 µm thick YAG plate) was introduced to the 2f-to-f signal before the dispersive fiber. This way replicas of the pulses with a known and fixed delay was created as a result of surface reflections on the etalon. This time-delayed replica generates an additional interference on top of the 2f-to-f spectral interference signal, although at a higher frequency and without CEP dependence. This superimposed modulation pattern is also mapped to the temporal domain by the DFT in the dispersive fiber, and it results in a waveform shown in Fig. 32. For this high frequency (426 MHz) modulation, the phase difference does not change with time, the fluctuations of the recovered phase can only result from the temporal jitter between the trigger signal and the laser pulses. The two different frequency modulations are separated by Fourier transform spectral analysis described in Chapter II.4.2. The original single modulation 2f-to-f signal is determined by digital low-pass filtering, while time jitter can be extracted through digital high-pass filtering the Fourier spectrum. By applying the inverse Fourier transform of these separated signals, they can be converted back to the time domain.

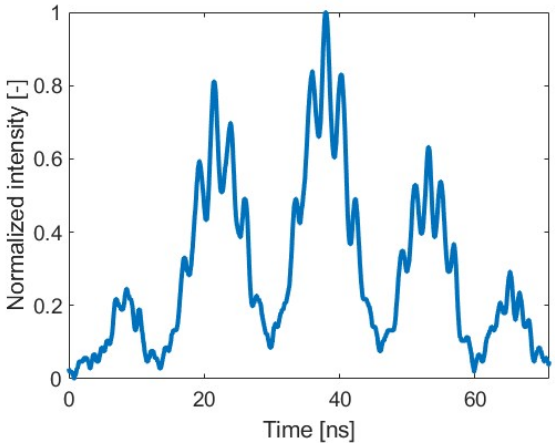

Fig. 32. Superimposed interference pattern with the delocalized CEP encoded in the low frequency modulation, while the time jitter can be determined from the high frequency modulation. [120]

The correction of time jitter was achieved as follows. Using the high-pass filtered data, the shot-to-shot temporal displacement caused by time jitter was determined and used to shift the low-pass filtered 2f-to-f signal in the time domain. This way time jitter was mitigated, which was one of the main limitations of the TOUCAN method. The time jitter corrected delocalized CEP measurement has much lower uncertainty than the uncorrected one. The circular correlation coefficient between the Fringeezz measurement and the decimated TOUCAN subset increased to 0.99, and the slope of linear fitting was 0.99 in this case, as it can be seen in Fig. 33 (a). The resulting CEP noise with lower uncertainties is displayed in Table 6. The PSD and IPN functions of the time jitter are also plotted in Fig. 33 (b). Although the reliability of these statistics increased, the overall phase noise did not change significantly, as the other noise sources still represent the majority of the contribution. Thanks to the jitter mitigation, only a few spikes disappeared from the PSD function, and the overall CEP noise and IPN functions remained almost the same.

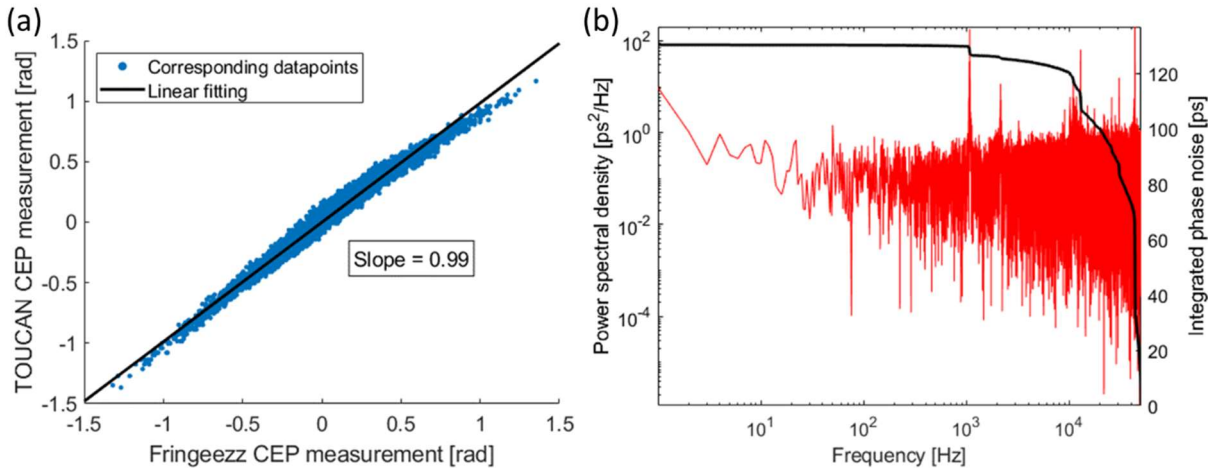

Fig. 33. (a) The scatter plot of delocalized CEP datapoints measured by the undersampled Fringeezz device and by the time-jitter mitigated TOUCAN technique. Linear fitting with a slope of 0.99 is displayed with a continuous black line. (b) The PSD and IPN functions of the measured time jitter. [120]

Fringeezz (stabilization off)	TOUCAN decimated	TOUCAN 100 kHz
341 ± 5 mrad	340 ± 19 mrad	338 ± 19 mrad

Table 6. Time jitter compensated CEP noise measurement

III.1.5. Intensity-phase coupling

Shot-to-shot pulse energy fluctuations can affect the SPM process regardless of the medium, as a result of which nonlinear phase change can fluctuate from shot to shot [62]. Most interferometric CEP measurements relies on SPM to create an octave broad spectrum necessary for detection, which means the measured CEP can have an additional spurious phase component depending on the pulse energy. This can affect not only standard interferometric CEP measurements, but also the TOUCAN measurements. To investigate this effect, the shot-to-shot intensity fluctuation was recorded with an amplified mid-IR photodetector (PDA10PT-EC, Thorlabs). The photodetector intensity level was recorded in the segmented memory mode by the same R&S oscilloscope. Two 2f-to-f interferometers were set up in parallel, and they were measured with the separate Fringeezz devices. One of the two Fringeezz was used for stabilizing the CEP of the laser, while the other one provided out-of-loop CEP measurement data. Synchronization was achieved by cutting the seed with the Dazzler, as described in Chapter III.1.3.The experimental arrangement is shown in Fig. 34.

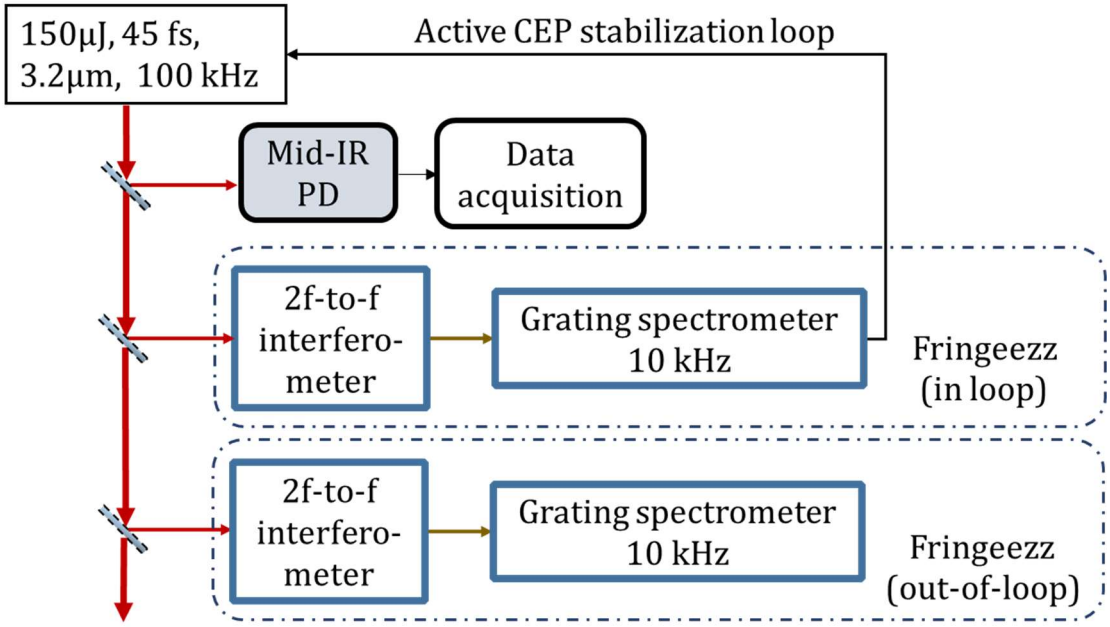

Fig. 34. Experimental arrangement to examine how the intensity fluctuation of the laser can affect the CEP measurement. One Fringeezz device was set up for active CEP stabilization, while the other one performed out-of-loop CEP measurement. Simultaneously, the intensity fluctuation of the laser was monitored by an amplified mid-IR photodetector.

To calculate the correlation between a circular parameter (the measured CEP) and a linear parameter (the photodetector voltage), the following equation [124] for linear-circular correlation coefficient was used

$$R_{lc\_corr.} = \sqrt{\frac{R(x,\cos(\alpha))^2+R(x,\sin(\alpha))^2-2R(x,\sin(\alpha))R(x,\cos(\alpha))R(\cos(\alpha),\sin(\alpha))}{1-R(\sin(\alpha),\cos(\alpha))^2}}, \quad \text{(III-9)}$$

where R is the linear correlation coefficient, x is a set of linear samples, and α is a set of circular samples, and R_{lc_corr} is the linear-circular correlation coefficient between x and α. Note that the linear-circular correlation coefficient lies between 0 (no correlation) and 1 (perfect correlation). High circular correlation of 0.8 was found between the two CEP measurements, but less than 0.1 linear-circular correlation was found between the photodetector signal and the out-of-loop

measured CEP after repeated measurements. This was true regardless of which Fringeezz was used for stabilization. The main reason for this was low intensity fluctuation, which was below 0.5 % RMS. Reference [62] indicates that this effect appears only when the laser intensity is modulated by a variable neutral density filter up to 10% of the full power continuously. Furthermore, the authors explicitly stated that they disregarded the inherent 1% RMS fluctuation of their laser system itself. The MIR system has an even smaller inherent fluctuation, and as it was proven by the measurement, intensity-phase coupling does not have a noticeable effect on the measured CEP in our case.

III.1.6. Outline

A new cost effective and simple method for delocalized CEP measurement named TOUCAN has been developed, calibrated and experimentally verified. The TOUCAN method is capable of single-shot measurements at arbitrary repetition rates and it was demonstrated on the 100 kHz MIR laser system for which no single-shot CEP detection was possible until now. In the absence of dedicated electronics recording the CEP, this was not performed real-time, and evaluation was performed in the framework of post-processing. As a high bandwidth FPGA based CEP recording system is currently in development, this issue will be addressed in the near future.

To verify the TOUCAN method, an experimental setup was built. Although it was designed for 100 kHz operation, based on the length of the temporal waveform it is suitable – without modifications – for measurements at repetition rates up to 10 MHz. The method can possibly be applied at even higher repetition rate lasers with less dispersive fibers and faster electronics and photodetectors. The main limitation in this case would be the ones imposed by the photodetector's response time, the bandwidth of the dedicated FPGA hardware computation and recording times. With these considerations even GHz repetition rates are within reach, even though no high intensity GHz repetition rate laser systems capable of driving CEP sensitive applications are currently available.

The uncertainty of the TOUCAN measurements can be improved to match or even exceed that of the Fringeezz device with dedicated electronics as the main limitation was the resolution of the recorded waveforms. Further improvements can be made by increasing dispersion by using a longer fiber, and consequently, by creating longer pulse temporal waveforms.

The absolute minimum energy needed for the CEP detection with the setup built to verify the TOUCAN method was 2.5 μJ. This can be further lowered, as 2f-to2f interferometers with specialized QPM crystals generating both SPM and SHG require only nJ pulse energies. In theory, this would allow for lowering the energy requirements to be many orders of magnitude below that of the single-shot stereo-ATI phase meter.

Summary I. I have developed an interferometric delocalized CEP measuring method, named TOUCAN, which is capable of single-shot measurements of few μJ energy pulses at higher repetition rates than ever before. The device was experimentally verified using the 100 kHz repetition rate MIR laser system. Shot-to-shot pulse energy change and temperature fluctuations as potential sources of measurement error were examined, and I have concluded that they have minimal effect on the accuracy of CEP measurements in the case of the examined laser. I have also shown that time jitter between the trigger and the detected photodetector signals significantly decreases the accuracy of the measurement. I have circumvented this issue by

creating an additional interference in the detected signal and removed the effect of time jitter via post-processing. The analysis of the CEP noise showed overwhelmingly high frequency noise components, which proves that CEP measurement and stabilization at full repetition rate is necessary to further reduce CEP noise in the MIR laser system.

III.2. Spectral phase shift measurement with dual-band SRI

As described in Chapter II.4.3., the SH-SRI is a modified version of standard SRI using nonlinear frequency conversion [50]. The phase shift recovered from the interferogram is doubled during the SH generation process. The SH-SRI technique records an interferogram at the SH frequency range, which can be used to determine the spectral phase shift at the fundamental frequency range. Because the SH-SRI technique relies on high resolution SWIR spectrometers for measurements in the mid-IR, which is a huge advantage, because high resolution mid-IR spectrometers are scarce and expensive. The SH-SRI can be further modified to create the dual-band SRI method, which determines the spectral phase shift at the fundamental and the SH frequency ranges at the same time, while the above mentioned benefit still holds.

The dual-band SRI method can have many scientific applications. At sufficiently high laser intensities even so-called non-ionizing (VIS-IR) EM radiation can ionize gases through multiphoton processes. By using SH and fundamental driving sources simultaneously, and by changing the relative phase between them, the behavior of the ionized electron can be modified [126]. This phenomenon is beneficial for many applications such as two-color terahertz generation [126,127] and two-color HHG [128,129]. These applications require spectrally broadband optical elements, where the induced spectral phase shift is characterized at both the fundamental and SH frequency bands. This gives plenty of motivation to develop a simple technique, where such characterization is possible using the same fundamental laser source, which is used for ionization.

III.2.1. Theoretical description and reconstruction methods

I define dual-band SRI as an SRI-based technique able to measure spectral phase shift at two bands simultaneously. To investigate the operation of this device a Mach-Zehnder type interferometer was first considered. Similarly to the SH-SRI arrangement, the SH beam is re-injected and sent through the interferometer backwards (opposite to the direction of the fundamental beam), as displayed in Fig. 35. This will result in additional interference patterns appearing in the interferogram. We can think of interferometers as replica generators. From an incoming pulse, the interferometer generates two pulses at the fundamental wavelength by beam splitting and recombination. The SH process generates two more pulses at the SH frequency, and because these two fundamental pulses are temporally separated, no parametric process can occur between the two (no SFG). Then the fundamental pulses are separated by a dichroic mirror, and the remaining two SH pulses are collimated. The SH pulses are separated from the fundamental pulses, and the SH pulses are sent through the same interferometer, which generates four pulses at the output. These four pulses spectrally interfere with one another. These interferences can be measured by a spectrometer or an optical spectrum analyzer. Both arms contain the same amount of transmission and reflection on optical elements, which means that the measurement of the empty interferometer (without an optical sample) will yield zero phase in this arrangement for both the SH and fundamental beams.

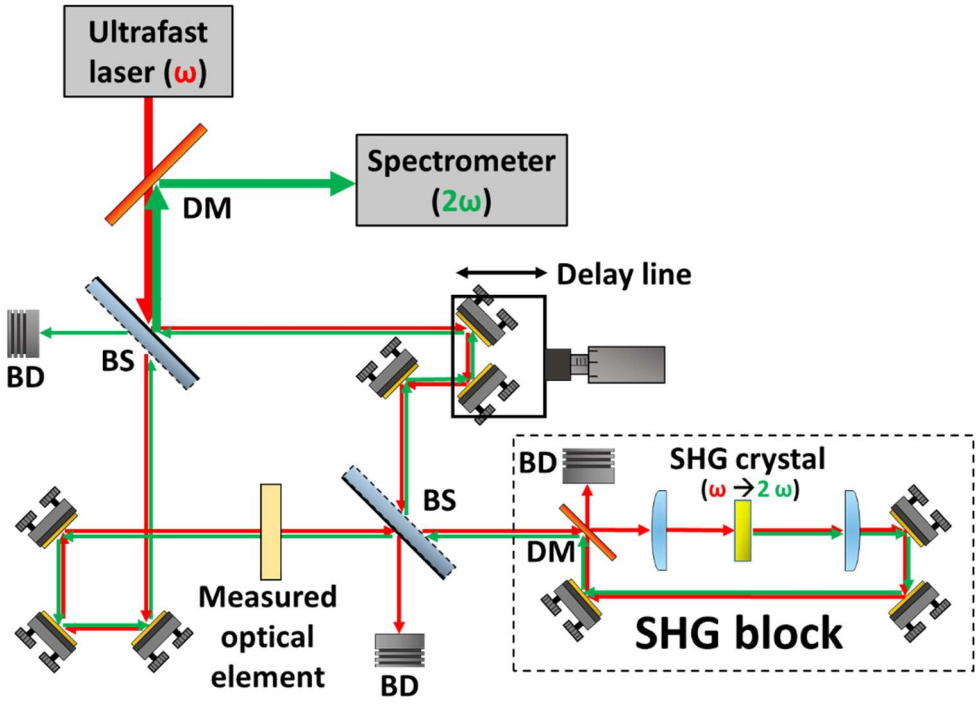

Fig. 35. Schematic view of the dual-band SRI realized with a Mach-Zehnder type interferometer arrangement. (b) DM – dichroic mirror reflecting 2ω and transmitting ω; BS – beam splitter; BD – beam dump, SHG crystal – nonlinear crystal for type I SHG.

The effect of this type of interferometer was first studied by a one-dimensional wave model based on Equation (II-70) and (II-75). Let us suppose that all phase differences between the two arms are caused by the measured optical sample. One of the four SH pulses does not contain spectral phase information about the optical sample. In the moving coordinate system of this pulse we can write the electric field as

$$E(2\omega) = A_1(2\omega)e^{i\Phi} + A_2(2\omega)e^{i(\omega\cdot GD(\omega)+2\varphi(\omega)+\pi/2+\Phi)} + A_3(2\omega)e^{i(\omega\cdot GD(2\omega)+\varphi(2\omega)+\Phi)} + \\ +A_4(2\omega)e^{i(\omega\cdot(GD(\omega)+GD(2\omega))+(2\varphi(\omega)+\pi/2+\varphi(2\omega))+\Phi)}, \quad \text{(III-10)}$$

where E(2ω) is the output electric field of the four SH pulses, Φ is the is the spectral phase of the first SH pulse, GD(ω), GD(2ω), φ(ω) and φ(2ω) are the group delays and the spectral phase shifts introduced by the optical path difference between the arms of the interferometer at the fundamental and the SH frequencies. The resulting interference will take the following form

$$I_n(f) = E(2\omega)\overline{E(2\omega)} = \left(A_1{}^2 + A_2{}^2 + A_3{}^2 + A_4{}^2\right) + \\ +2(A_1A_2 + A_3A_4)\cos(\omega\cdot GD(\omega) + 2\varphi(\omega) + \pi/2) + \\ +2(A_1A_3 + A_2A_4)\cos\left(\omega\cdot GD(2\omega) + \varphi(2\omega)\right) + \\ +2A_2A_3\cos\left(\omega\cdot\left(GD(\omega) - GD(2\omega)\right) + 2\varphi(\omega) + \pi/2 - \varphi(2\omega)\right) + \\ +2A_1A_4\cos\left(\omega\cdot\left(GD(\omega) + GD(2\omega)\right) + 2\varphi(\omega) + \pi/2 + \varphi(2\omega)\right). \quad \text{(III-11)}$$

All five components will have one or two corresponding spikes in the Fourier domain. The first component (DC) will have only one at time zero, while the other components, which hold phase information, will be moved by their linear phase (GD). We can name these spikes in the order

of appearance in Equation (III-11): time zero spike, fundamental spikes, SH spikes, difference spikes and summa spikes.

Based on Equation (III-11), I have also performed a numerical simulation. The simulated broadband light source had the same parameters as the MIR laser. The investigated sample was a 4 mm thick thallium bromo iodide crystal (KRS-5) [130] optical window, which caused all the optical path difference in the arms. It was assumed that all other sources of uneven dispersion in the arms (air propagation, optical components) can be neglected. The simulated interferogram of the four pulses is displayed in Fig. 36 (a). The FTSI method is used to extract the phase from the interferogram, because in the Fourier domain the spikes corresponding to the different interference patterns can be distinguished and separated [131–133]. The generated four pulses have 3^2=9 spikes in the Fourier domain, but the spikes in the negative time domain and the time zero spike can be safely ignored as they contain no additional phase information. There are $(3^2-1)/2$=4 possible group delays between the four pulses: GD(ω), GD(2ω), $|GD(\omega) - GD(2\omega)|$, and $GD(\omega) + GD(2\omega)$, as seen in Equation (III-11) too. When the interferogram is Fourier transformed, all four GDs will have a corresponding spike in the positive time domain as it is displayed in Fig. 36 (b), where the time delay between the four pulses can be observed, as described in Chapter II.4.2.

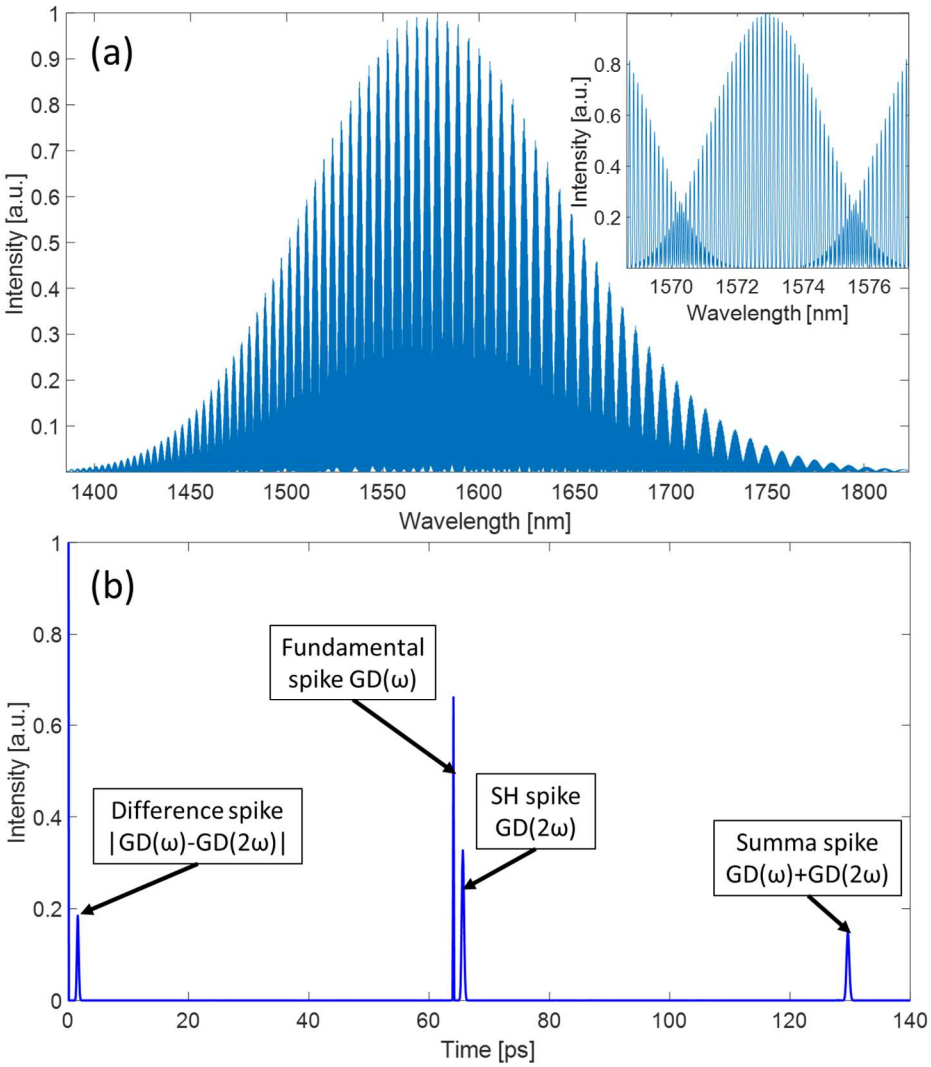

Fig. 36. (a) Simulated spectral interferogram at the output of the dual-band SRI containing a 4 mm thick KRS-5 window. (b) The calculated FT of this interferogram is shown only for a positive time axis.

The spectral phase shift at the fundamental and the SH frequency bands can be calculated from any of the two spikes, not just the fundamental and the SH spikes. There are six possible combinations. All of these cases are listed in Table 7.

Spike	1	2	3	4	5	6
Fundamental (F)	x	x	x			
Second harmonic (SH)	x			x	x	
Difference (Δ)		x		x		x
Summa (Σ)			x		x	x

Table 7. All possible combinations of two different spikes, which can be used to calculate the spectral phase shift at the fundamental and the SH frequency bands.

The phase of the difference spike can be $\varphi_F - \varphi_{SH}$ and $\varphi_{SH} - \varphi_F$ both, depending on the GD difference between the fundamental and SH spikes. The mirror image of the difference spike at negative time delay is its complex conjugate, so it possesses the opposite phase. As we narrowed the investigations to the spikes at positive time delays, we need to introduce a sign quantity to avoid confusion in future equations

$$S = \mathrm{sign}\big(GD(\omega) - GD(2\omega)\big), \tag{III-12}$$

which can be –1 and 1. Calculated from Equation (III-11) and using the S quantity, only 12 equations are needed to express the spectral phase shifts at the ω and 2ω frequency bands for all six cases. In these equations I have disregarded constant phase offsets, which – as I show later – will not impact the overall results

$$\text{Case 1.} \quad \varphi(\omega) = \frac{\varphi_F}{2}, \qquad \varphi(2\omega) = \varphi_{SH}, \tag{III-13}$$

$$\text{Case 2.} \quad \varphi(\omega) = \frac{\varphi_F}{2}, \qquad \varphi(2\omega) = \varphi_F - S\varphi_\Delta, \tag{III-14}$$

$$\text{Case 3.} \quad \varphi(\omega) = \frac{\varphi_F}{2}, \qquad \varphi(2\omega) = \varphi_\Sigma - \varphi_F, \tag{III-15}$$

$$\text{Case 4.} \quad \varphi(\omega) = \frac{\varphi_{SH} + S\varphi_\Delta}{2}, \qquad \varphi(2\omega) = \varphi_{SH}, \tag{III-16}$$

$$\text{Case 5.} \quad \varphi(\omega) = \frac{\varphi_\Sigma - \varphi_{SH}}{2}, \qquad \varphi(2\omega) = \varphi_{SH}, \tag{III-17}$$

$$\text{Case 6.} \quad \varphi(\omega) = \frac{\varphi_\Sigma + S\varphi_\Delta}{4}, \qquad \varphi(2\omega) = \frac{\varphi_\Sigma - S\varphi_\Delta}{2}. \tag{III-18}$$

The first case, where fundamental and SH spikes are used, is the most straightforward one, and it also has the lowest relative error based on simple error propagation model. These spikes can be called pure spikes to distinguish them from mixed spikes (difference and summa), where the phase is a mix of the spectral phase shifts of the two frequency bands. Thus, in all future calculations, unless stated otherwise, the pure spikes described by Equation (III-13) are used to determine the phase at the two frequency bands.

III.2.2. Verification by measuring well-known materials

The disadvantage of the arrangement shown in Fig. 35 is that it cannot be used with two separate delay lines for the SH and the fundamental pulses. This limitation is a cause for concern, when the fundamental and the SH spikes resulting from the Fourier transform of the

measurement are not well-separated in the Fourier (time) domain. This is the case, when the Fourier transform limit (FTL) of the SH pulse broadened by the spectral phase difference as described by Equation (II-82) is long in time compared to the GD difference between the fundamental and the SH pulses. Otherwise, the SH and the fundamental spikes completely or partially overlap, hindering the correct retrieval of the spectral phase shift. Increasing the optical path difference with the delay stage does not help, as it will equally shift the GDs of both the fundamental and the SH spikes, because the dispersion of air is negligible. When the GD difference between the fundamental and the SH pulses is too low, extracting the phase from the difference spike is also problematic because it will partially overlap with the time zero spike.

To prove that this problem occurs not only in simulations, but also in experimental conditions, a device based on the schematic arrangement of Fig. 35 was realized. As a broadband light source, 900 mW average power (corresponding to 9 µJ pulse energies) of the MIR laser was used for the experiment. The beam splitter (BSW511, Thorlabs) has 67% transmission at the central wavelength of the laser, and 46% transmission at the SH central wavelength. The SH of the MIR laser was generated in a 500 µm thick silver gallium sulfide (AGS) nonlinear crystal using type I interaction (θ=39°, φ=45°). The conversion bandwidth is calculated to be roughly ~900 nm, more than enough to cover the entire MIR laser spectrum. Both the focusing of the fundamental and the collimation of the SH beams were performed by 150 mm focal length CaF_2 lenses. All flat mirrors had unprotected gold coating. The measured optical sample was a 3 mm thick YAG optical window. As suspected, the SH and the fundamental spikes partially overlap, and the difference spike overlaps with the time zero spike, as shown in Fig. 37. Only the summa spike phase can be measured without interference, but on its own it is insufficient to decouple the spectral phase shifts at the SH and fundamental bands.

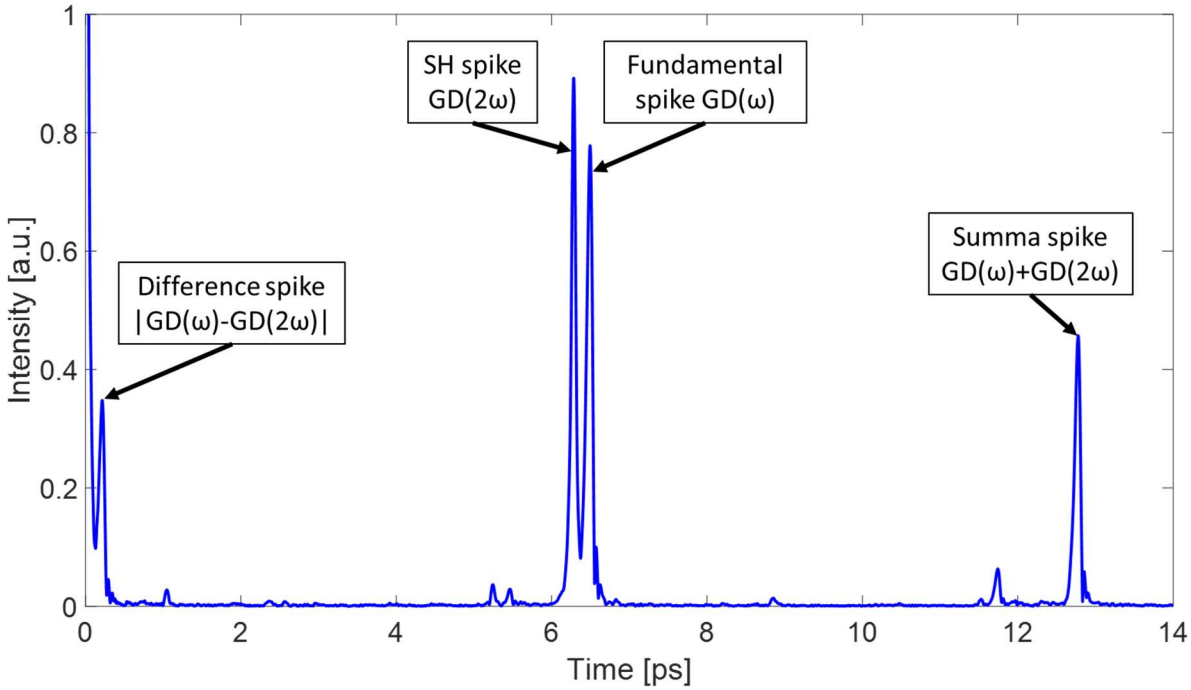

Fig. 37. The calculated Fourier transform of spectral interference at the output of a Mach-Zehnder type dual-band SRI device containing a 3 mm YAG plate in one of the arms. The fundamental and SH spikes partially overlap, and so do the difference spike and the time zero spike.

For these reasons, I generally recommend a Michelson type interferometer for dual-band SRI measurements, as displayed in Fig. 38, using separate delay lines for the SH and the fundamental beams. In this case, the optical path difference of the SH and the fundamental beams, and consequently the density of the corresponding interferences, can be set independently by the two delay stages (fundamental and SHG delay lines). The alignment of the device is also easier with separate delay lines. Just by blocking the beam of one of the two delay lines, only the interference stemming from the other delay line remains. This way the visibility of SH and fundamental interference fringes can be maximized independently.

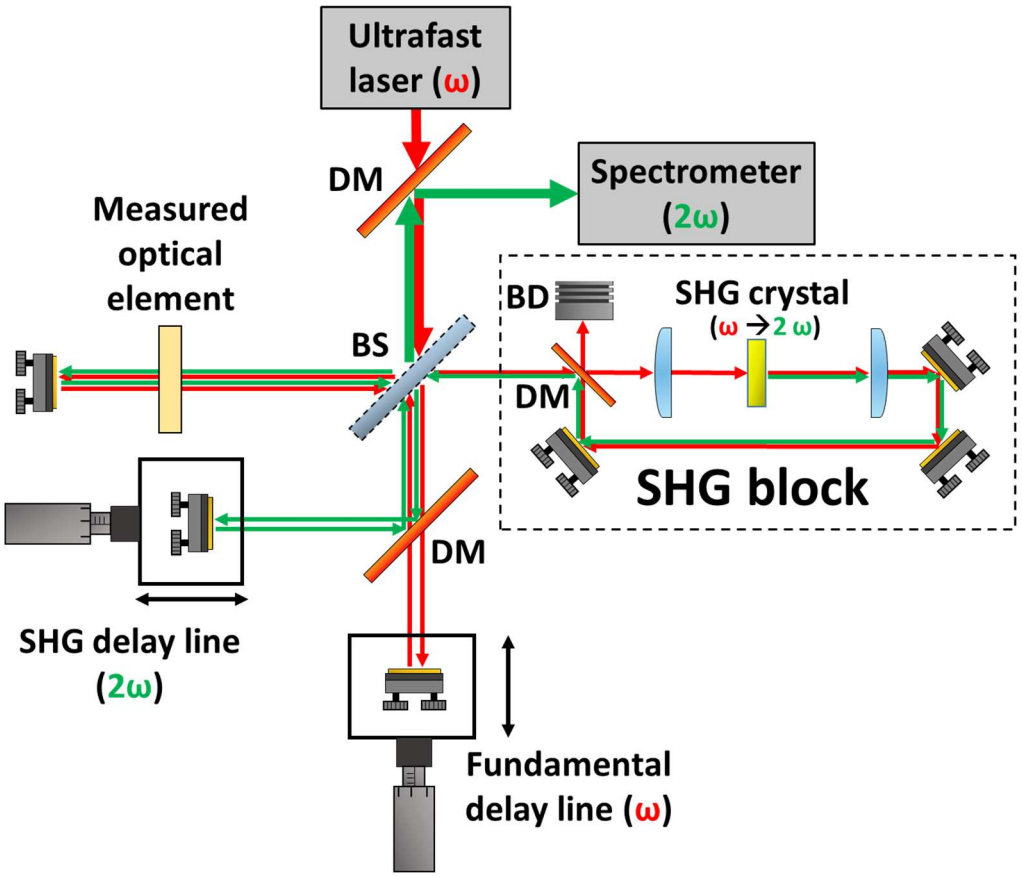

Fig. 38. Schematic setup of the dual-band SRI realized with a Michelson type interferometer arrangement. The SHG block creates the SH of the fundamental frequencies and sends it back to the interferometer. DM – Dichroic mirror reflecting 2ω and transmitting ω; BS – Beam splitter; BD – Beam dump, SHG crystal – nonlinear crystal for type I SHG.

The SHG block contained the same optical elements as described in the Mach-Zehnder type dual band SRI arrangement. At 1.6 µm central wavelength, the generated SH beam has perpendicular polarization compared to the fundamental, which poses no issue for the measurement of isotropic material. For the measurement of birefringent optical samples an additional waveplate is required to rotate the polarization back. The initial measurement was performed on a 4 mm thick KRS-5 optical window. The interferogram was recorded by a SWIR optical spectrum analyzer (AQ6375B, Yokogawa) with a spectral resolution of 0.05 nm. The recorded interferogram is displayed in Fig. 39 (a), while its Fourier transform is displayed in Fig. 39 (b). These spikes resemble the simulated ones shown in Fig. 36 (b), with different GDs set by the delay lines.

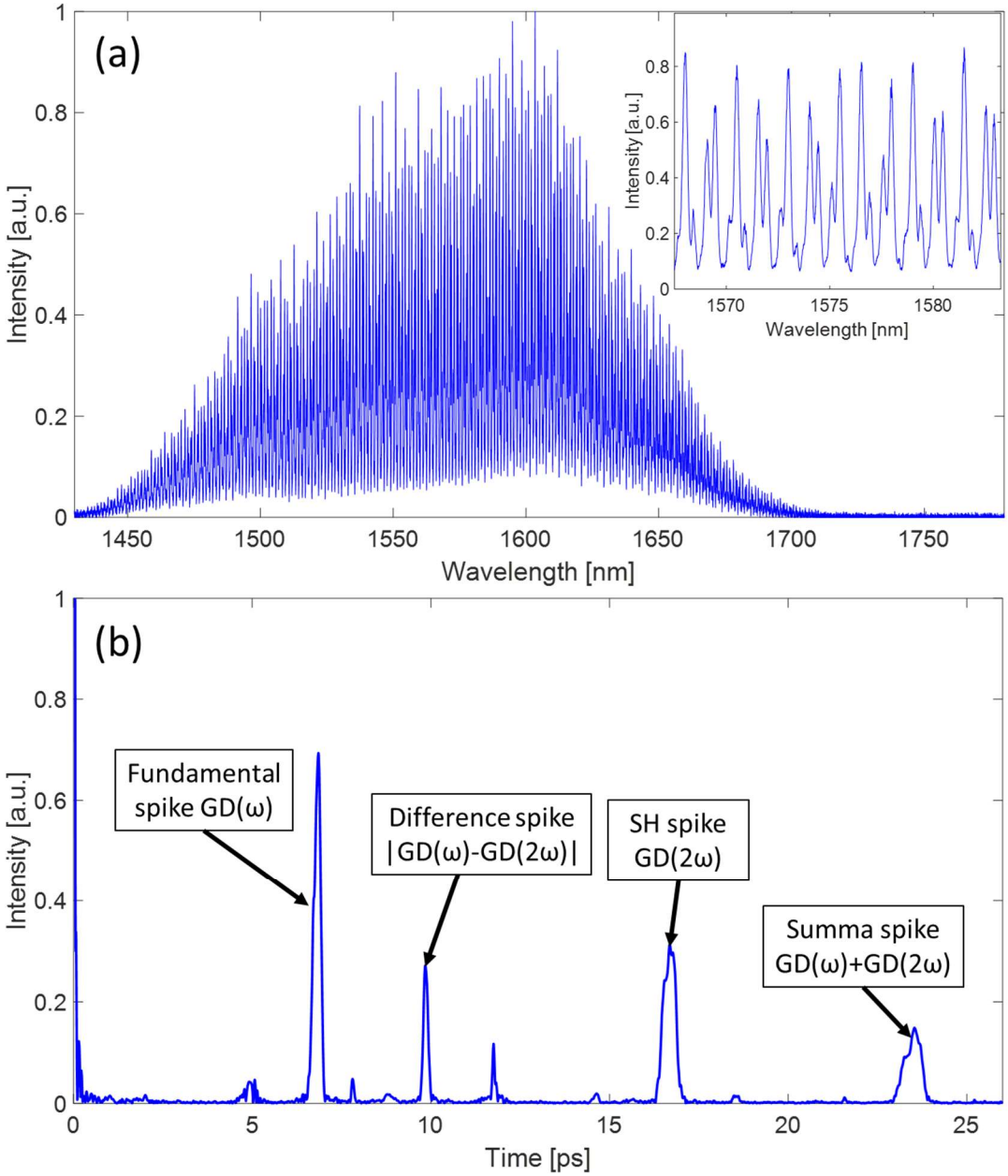

Fig. 39. (a) Measured spectral interference at the output of a Michelson type interferometer containing a 4 mm thick KRS-5 optical window using dual-band SRI. (b) The calculated FT of this spectrum, which contains no overlap between the spikes. The extra low intensity spikes stem from surface reflections of the KRS-5, which can be disregarded.

For the retrieval of the spectral phase shift from the measured data, the FT spectral analysis was used, by inverse Fourier transforming the fundamental and the SH spikes separately. The spectral phase shift of the empty interferometer (no sample) was measured as a reference, and later this "background" phase was subtracted from all the measurements. To investigate the repeatability of the results, 100 interferograms were recorded with the same parameters. From the 100 phase shift functions, mean and STD functions were calculated.

The delay line in the standard SRI and SH-SRI methods can be set arbitrarily over a relatively long range. Spectral phase shift measurements were performed with different SHG and fundamental delay line positions, but no significant deviation was observed in second and higher order dispersion, only the recovered GD was different. Because of this freedom, there is an inherent ambiguity not only in the constant phase offset but also in the linear phase (GD).

For this reason, in every instance the mean linear part of the phase was determined by least squares fitting, and later it was subtracted from the phase. This means that all the phase shift functions were shifted, so the mean phase shift crossed zero at the central wavelength of the laser or at its SH central wavelength, depending on which frequency band was investigated. Throughout my dissertation, GD compensation stands for the removal of the linear phase and constant phase, and the remaining spectral phase is called GD compensated phase. This process can be observed in Fig. 40. The subtraction of the linear part does not affect the GDD and higher orders of the dispersion parameters. This way, the measured spectral phase can be visually compared to the values calculated using the Sellmeier formula obtained from the literature [130,134–136].

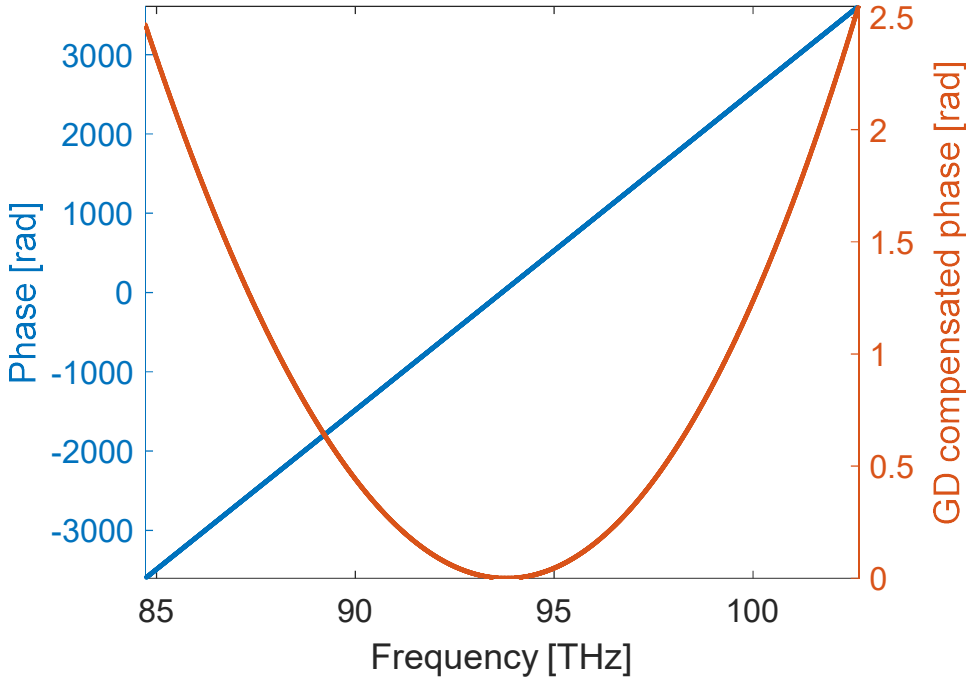

Fig. 40. A calculated spectral phase shift, which contains a large amount of linear phase plotted in blue. The same phase after GD compensation is plotted in red, showing a parabolic shape as the result of the dominating GDD component in the remaining GD compensated phase.

I examined several material windows, a 4 mm thick KRS-5 optical window, a 3 mm thick YAG [134] optical window, a 3 mm thick barium fluoride (BaF_2) [135] optical window, and a 3 mm thick calcium fluoride (CaF_2) [136] optical window. The calculated and the measured GD compensated spectral phase shifts are plotted in Fig. 41 – Fig. 44. As no linear phase remains, the plotted functions are close to being parabolic curves. For materials with positive GVD the parabolas open upwards, while for negative GVD materials the parabolas open downwards. Note that the SH central wavelength of 1.6 µm is very close to the zero dispersion wavelength for the dielectric YAG, CaF_2 and BaF_2 materials. We can see that even in the case of very low dispersion, the retrieved phase curves are in good agreement with the calculated ones.

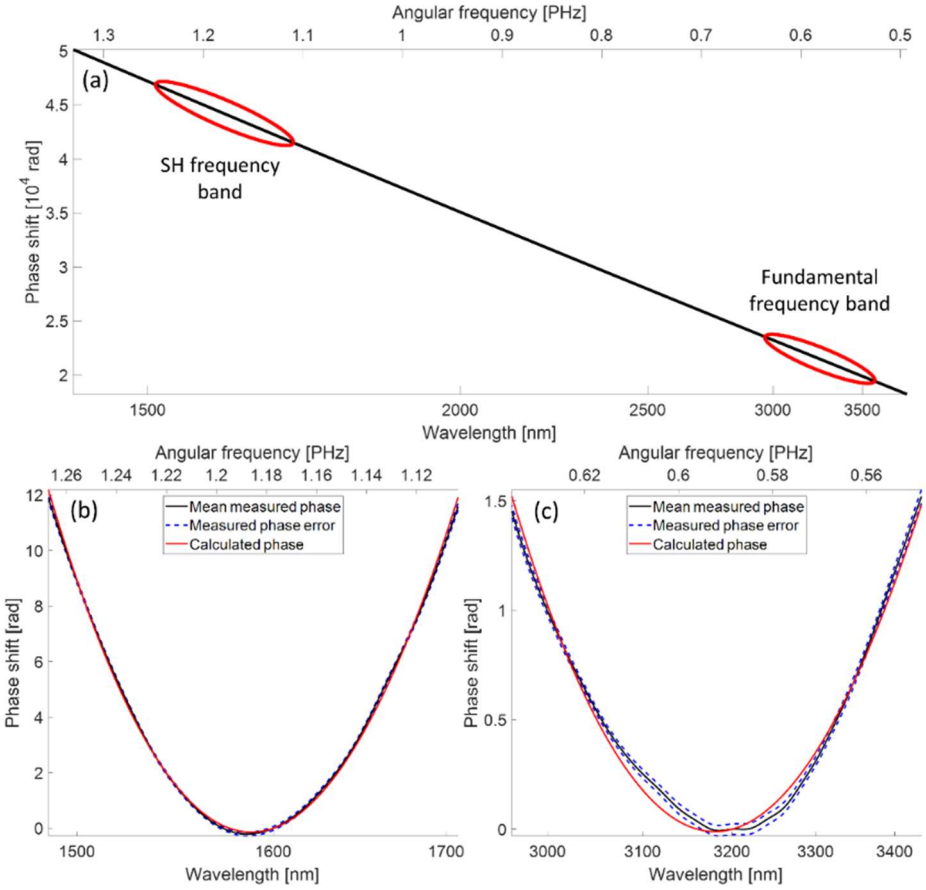

Fig. 41. (a) Calculated spectral phase shift from propagation through a 4 mm thick KRS-5 optical window in double-pass configuration using the Sellmeier equation. The frequency bands measured with the current SH-SRI setup are highlighted with red. The GD compensated, calculated and measured spectral phase shift retrieved at the (b) SH and the (c) fundamental frequency bands.

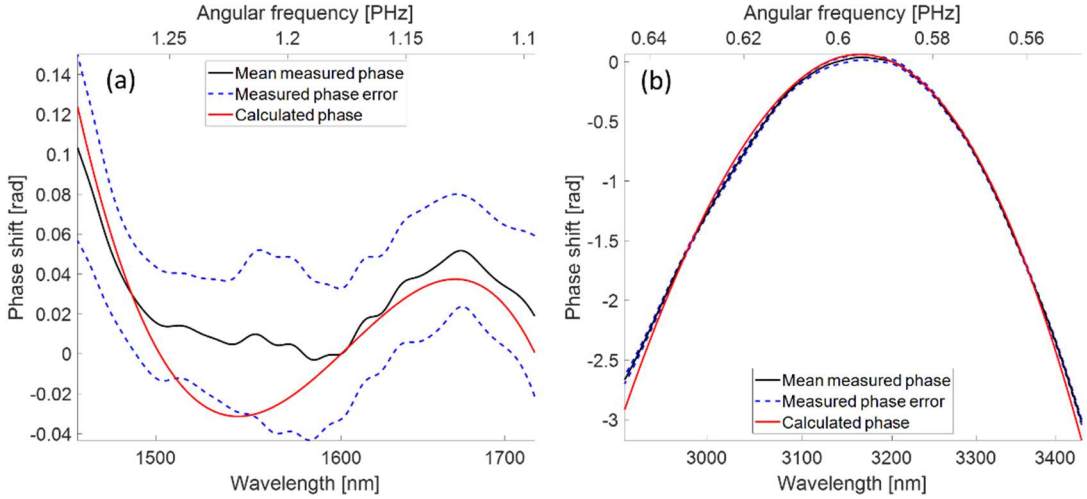

Fig. 42. Calculated and measured GD compensated, spectral phase shift after propagating through a 3 mm thick YAG optical window in double-pass configuration, retrieved at the (a) SH and the (b) fundamental frequency bands.

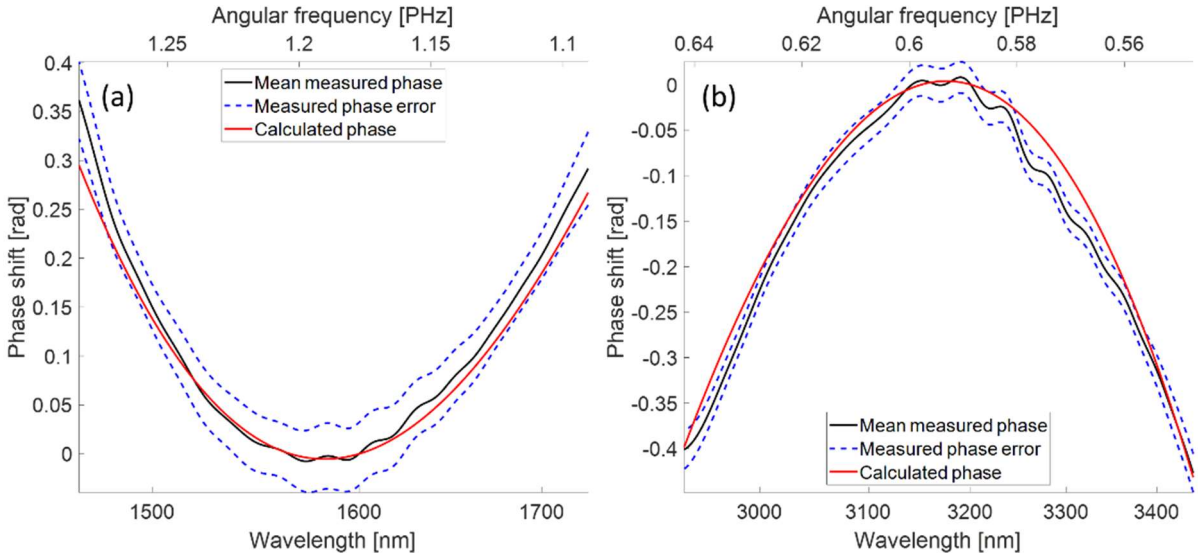

Fig. 43. Calculated and measured GD compensated spectral phase shift after propagating through a 3 mm thick BaF_2 optical window in double-pass configuration, retrieved at the (a) SH and the (b) fundamental frequency bands.

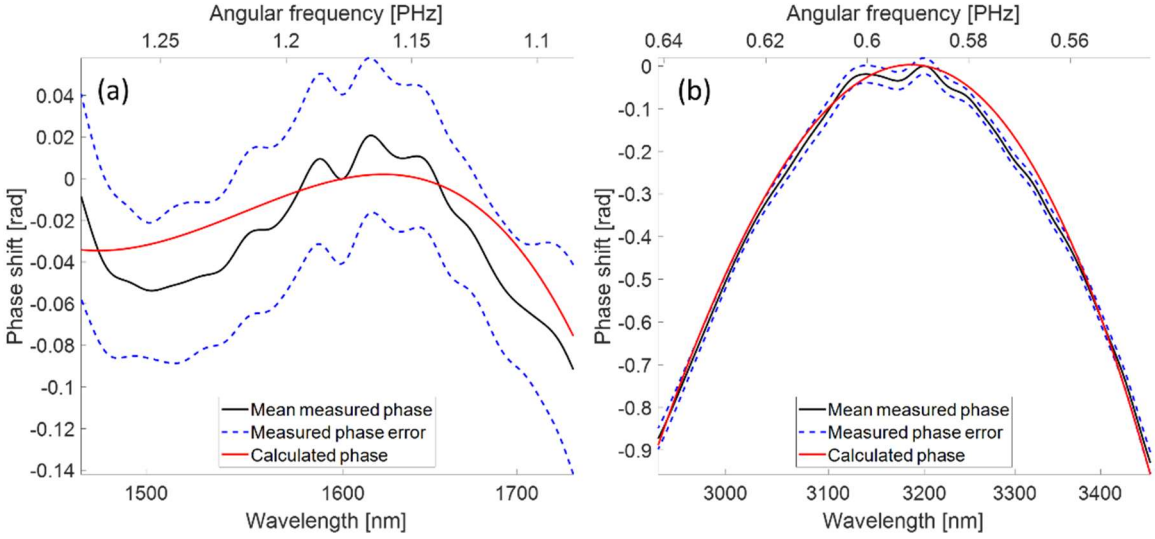

Fig. 44. Calculated and measured GD compensated, spectral phase shift after propagating through a 3 mm thick CaF_2 optical window in double-pass configuration, retrieved at the (a) SH and the (b) fundamental frequency bands.

III.2.3. Comparing reconstruction from pure and mixed spikes

The interferogram contains double the information necessary for the complete reconstruction of the spectral phase shift at both frequency bands. This allows for multiple ways to reconstruct the spectral phase shifts using the same interferogram. So far only Case 1 of Table 7 was used because of the simplicity of the equations. To prove that other phase reconstruction methods are just as viable, the spectral phase shifts were calculated using mixed states with Equations (III-18) of Case 6 as well. For the purpose of comparison, the same interferograms and reference background measurements (no sample) were used. By comparing the GD compensated phase shifts no significant difference was found in the shape of the curves regardless of the reconstruction method. To quantize the difference, the GDD values at the central frequency of the fundamental and the SH pulses were used for the comparison. These were calculated by polynomial fitting on the spectral phase curves for every single recorded interferogram. The mean and standard deviations of the retrieved GDDs were also calculated

and they are summarized in Table 8. The calculated GDD values were obtained with the material database software described in Chapter II.3.2 using Sellmeier equations.

GDD [fs^2]	Measured from single spikes (Fundamental, SH)	Measured from mixed spikes (Difference, Summa)	Calculated from Sellmeier equations
4 mm KRS-5 (1.6 µm)	1794 ± 21	1766 ± 56	1803
3 mm YAG (1.6 µm)	9 ± 19	7 ± 20	2
3 mm BaF_2 (1.6 µm)	35 ± 6	31 ± 18	30
3 mm CaF_2 (1.6 µm)	–8 ± 7	–16 ± 21	–6
4 mm KRS-5 (3.2 µm)	787 ± 25	709 ± 82	791
3 mm YAG (3.2 µm)	–1391 ± 42	–1382 ± 43	–1375
3 mm BaF_2 (3.2 µm)	–190 ± 13	–224 ± 39	–192
3 mm CaF_2 (3.2 µm)	–382 ± 14	–414 ± 40	–398

Table 8. The GDD values at the fundamental and the SH frequency reconstructed from single spikes and mixed spikes, compared to calculated values determined from Sellmeier equations.

As can be seen, the calculated GDD values are within two sigma confidence intervals of the mean values at all cases, which confirms that the two pure and the two mixed-state spikes also hold full information of both spectral bands. This means that a single dual-band SRI spectrum demonstrably contains double the information necessary for complete spectral phase shift reconstruction. However, the reconstruction of the mixed states generates higher uncertainty than the reconstruction of pure spikes.

III.2.4. Possibilities for extension

A different arrangement can be made based on the dual-band SRI setup, one that measures the spectral phase shift of an optical element at the ω, 2ω, and 4ω frequencies too. This hypothetical setup only requires a spectrometer sensitive in the 4th harmonic frequency range. With the 3.2 µm central wavelength MIR laser, the generated 4th harmonic would be around 800 nm, where silicon based high resolution spectrometers are available. This arrangement is shown in Fig. 45, and it is named triple-band SRI, as it effectively probes optical elements at three frequency bands at the same time. Compared to the dual-band setup, an additional SHG block is required to generate a 4th harmonic beam from the SH beam, altogether 8 pulses at 800 nm. After the separation of the SH beam, the 4th harmonic beam is sent back to the same interferometer. The most practical arrangement includes a Michelson type interferometer with three separate delay lines.

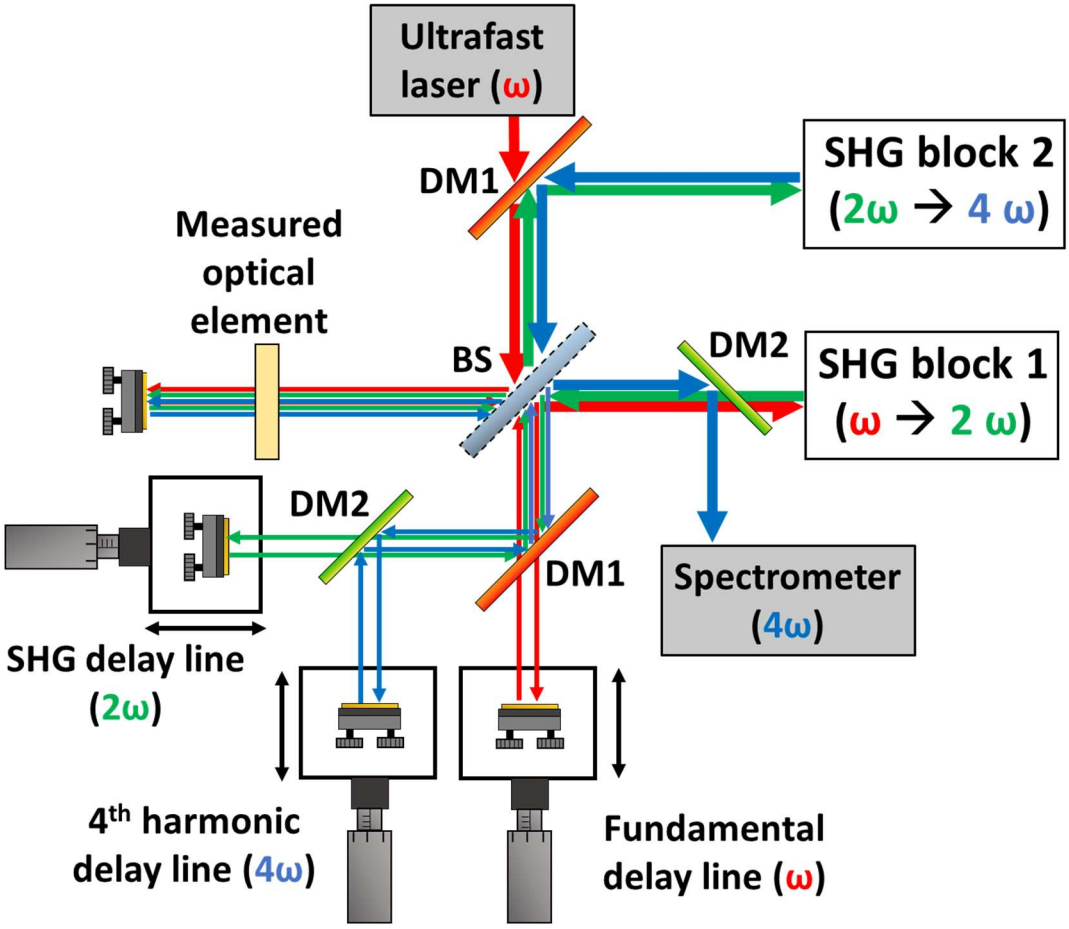

Fig. 45.Schematic setup of the triple-band SRI with a Michelson type interferometer. SHG block 1 creates the SH of the fundamental frequencies and SHG block 2 creates the 4th harmonic from the SH. DM1 – dichroic mirror transmitting ω, and reflecting 2ω, and 4ω; DM2 – dichroic mirror transmitting ω, and 2ω and reflecting 4ω; BS – beam splitter.

Performing measurements with the triple-band SRI would result in a spectrum with $(3^3 - 1)/2=13$ interferences corresponding to 13 spikes in the positive time domain at 13 different group delays: GD(ω), GD(2ω), GD(4ω), GD(ω) + GD(2ω), GD(ω) + GD(4ω), GD(2ω) + GD(4ω), GD(ω) + GD(2ω) + GD(4ω), |GD(ω) − GD(2ω)|, |GD(ω) − GD(4ω)|, |GD(2ω) − GD(4ω)|, |GD(ω) − GD(2ω) + GD(4ω)|, |GD(ω) + GD(2ω) − GD(4ω)|, |−GD(ω) + GD(2ω) + GD(4ω)|. The corresponding phases hold information about the spectral phase shifts at the fundamental, SH and 4th harmonic frequency ranges. From the 13 spikes in the positive time domain three must be chosen for reconstruction, which allows for 286 possible combinations. However, only 246 of them contain sufficient information to determine the phase at all three frequency bands. The most straightforward way is using the pure spikes at GD(ω) (fundamental), GD(2ω) (SH), and GD(4ω) (4th). In this case the spectral phase shifts are calculated as follows

$$\varphi_\omega = \frac{\varphi_{\text{Fund.}}}{4}, \qquad \varphi_{2\omega} = \frac{\varphi_{\text{SH}}}{2}, \qquad \varphi_{4\omega} = \varphi_{4^{\text{th}}}. \tag{III-19}$$

A triple-band SRI device would require extremely broadband optical components, which is especially challenging for the beam splitter and the dichroic mirrors. The realization, alignment and evaluation of the triple-band SRI setup would be a considerably complex task. Furthermore, there are only a few applications where spectral phase shift measurements are required at all three frequency bands. Consequently, no attempt was made to build this device.

While even the realization of triple-band SRI would be challenging, I have extended the theoretical method to its logical extremum, and defined the n-band SRI method. The n-band SRI method would be very complex, it would have n–1 SHG blocks and n delay lines. This will generate 2^n pulses, with $(3^n - 1)/2$ distinct interferences between them. The corresponding $(3^n - 1)/2$ spikes in the positive Fourier domain would not overlap with each other after careful alignment of the n delay lines. Let us suppose that the spikes are isolated when they have x ps time difference between them. In this case, the first delay line should be set to GD(ω)=x ps, the second should be set to GD(2ω)=3x ps, third one to GD(4ω)=9x ps, and the n^{th} one to GD(2^{n-1}ω)=3^{n-1}x ps. Now all the neighboring spikes have exactly x ps time difference between each other. This would require a spectrometer with a resolution of at least $1/(2(3^{n-1}+1) \cdot x)$ THz to avoid aliasing.

III.2.5. Outline

In this chapter the dual-band spectrally resolved interferometric method is presented, that can retrieve the spectral phase shifts at the fundamental and the SH frequency bands simultaneously. Phase shift reconstruction is possible from a single spectrogram without extreme requirements for the bandwidth of the used spectrometer. A Michelson type interferometer with two separate delay lines is presented as the most reliable dual-band variant, capable of spectral phase shift evaluation even close to the zero dispersion wavelength. To validate the method and the device, the spectral phase shift of several optical windows was reconstructed at the two frequency bands. The resulting spectral phase curves showed excellent agreement with the spectral phase curves determined from the Sellmeier equations obtained from literature. It can be concluded that the presented method is an excellent tool for measuring the spectral phase simultaneously at the SH and the fundamental frequency bands, which could be useful for characterizing the optical components designed for applications such as two-color terahertz generation or two-color HHG.

Other modified versions of the dual-band SRI were also examined theoretically. A single delay line Mach-Zehnder type interferometer based setup was numerically simulated and experimentally tested. Due to spike overlaps in the FT domain, this device was incapable of determining the spectral phase shifts. The Michelson type interferometer based triple-band and n^{th}-band SRIs were also theoretically examined, but due to their complexity they were not realized in practice.

Summary II. I have developed a technique called dual-band SRI to characterize the spectral phase shift of optical elements at the fundamental and SH frequency bands of an ultrafast laser source simultaneously from interferograms recorded exclusively at the SH frequency band. The technique was first examined by theoretical description and numerical simulation, and was then tested experimentally. I built a dual-band SRI device, and performed measurements using 9 μJ energy pulses from the MIR laser system. The spectral phase shift of well-known optical materials was measured, which verified both the technique and the device. Furthermore, I have proven that a single measured interferogram holds double the information necessary for the complete reconstruction of the spectral phase shift at both bands, by employing and comparing different evaluation methods. By using the wave theory description of dual-band SRI, I examined further extensions of the method to measure more than two frequency bands simultaneously.

III.3. Post-compression of mid-IR pulses

The MIR laser system, described in Chapter II.6.4, produces sub-5 cycle pulses at relatively high average power (>10 W). Different post-compression techniques were considered (described in Chapter II.6.3), to compress these pulses. Based on the review given therein, we chose spectral broadening in thin optical windows, after which we used recompression in bulk due to the methods' relative simplicity and cheap components. During the investigation, it was important to find the most suitable materials for spectral broadening and for the bulk compressor as well. In this search several material properties were deliberated: spectral transmission, nonlinear refractive index, material dispersion, and two-photon absorption. The main concern was the fact, that MIR laser system provides relatively high average power, which in some cases can lead to optical damage through thermal shock in these materials. This led us to prioritize nonlinear crystals based on their nonlinear refractive indices, so that we can use relatively big spot sizes and moderate laser intensities and irradiances on these crystals, and still achieve sufficient broadening, without optical damage.

III.3.1. Material selection

As it was described in Chapter II.2.1, solids can be assigned to three categories based on their bandgaps: metals, semiconductors and dielectrics. Only two of these materials can transmit mid-IR radiations: semiconductors and dielectrics. Semiconductors have positive GVD at 3.2 μm, as seen in Fig. 6 and high nonlinear refractive index ($n_2>10^{-15}$ cm^2/W), because of the relation between the bandgap and the nonlinear refractive index shown in Equation (II-65). However, the narrow bandgap of semiconductors also means that fewer photons are needed for nonlinear absorption, which can decrease transmission at high intensities. On the other hand, dielectrics have negative GVD at 3.2 μm, but they possess a lower nonlinear refractive index ($n_2<10^{-15}$ cm^2/W). Note that as it was mentioned in Chapter II.2.2, both semiconductors and dielectrics have positive STOD, which can limit pulse compression of few-cycle pulses in bulk media. To find the most suitable nonlinear crystals, the software described in Chapter II.3.2 was used. The relevant parameters of the material candidates for post-compression are summarized in Table 9.

As the nonlinear reflective index is the driving force for the SPM process, semiconductors i.e.: Si, GaAs and Ge were the prime candidates, as they have the highest nonlinear refractive index. Ge has a bandgap of 0.66 eV, which allows for parasitic two-photon absorption at 3.2 μm (0.39 eV). GaAs looks more promising, but no vendor was found selling optical windows with anti-reflection (AR) coating for broadband mid-IR sources, which is necessary for semiconductors with a large refractive index, to minimize Fresnel losses on the front and back surfaces. On the other hand, Si has a bandgap of 1.1 eV, setting the onset of non-linear absorption to three or more photons, which makes it preferable to germanium. Furthermore, multiple vendors sell them with broadband mid-IR AR coating. To compensate for the added high positive GDD of a Si plate, a negative GVD dielectric must be chosen as the second plate. Out of all the commercially available dielectrics listed in Table 9, YAG has the highest nonlinear refractive index. A single potassium bromide plate was also considered for its low GVD and STOD parameters, as a result of which long soliton like propagation and broadening

can be achieved in the material. Unfortunately, it is hygroscopic, which means that the crystal would degrade in air after long use. These arguments led us to choose the combination of an uncoated Si and an AR coated YAG plate for the setup.

The same combination was proposed by Faming Lu et al. [100], for the post-compression of an ultrafast mid-IR laser with parameters somewhat similar to the MIR laser, but at only 300 Hz repetition rate, which means that the average power was only <50 mW of compared to the 11 W used in our experiments.

Material name	n [-]	GVD [fs^2/mm]	STOD [fs^3/mm]	Calculated n_2 [cm^2/W]	Comment
Magnesium fluoride	1.36	–193.2	1116.47	5.02E–17	Birefringent
Lithium fluoride	1.36	–296.21	1663.68	7.10E–17	
Barium fluoride	1.46	–64.1	400.2	1.81E–16	
Calcium fluoride	1.42	–133.25	764.22	1.89E–16	
Sapphire	1.71	–694.67	4296.05	3.06E–16	Birefringent
YAG	**1.78**	**–460.21**	**2951.87**	**7.02E–16**	
Potassium bromide	1.54	12.88	105	8.70E–16	Hygroscopic
Zinc sulfide	2.26	41.49	537.68	2.81E–15	
Zinc selenide	2.44	142.96	476.33	5.58E–15	
Silicon	**3.43**	**485.16**	**866.68**	**3.14E–14**	
Gallium arsenide	3.31	557.47	1252.02	2.94E–13	
Germanium	4.04	1402.66	3024.02	3.17E–13	Two-photon absorption

Table 9. The relevant optical parameters at 3.2 μm of nonlinear crystal candidates for post-compression in ascending order regarding the nonlinear refractive index. The bold lines correspond to the chosen materials.

III.3.2. Spectral broadening in thin plates

The thicknesses of the two plates were chosen to optimize spectral broadening and minimize dispersion. Thinner plates at the same laser intensities accumulate less nonlinear phase through propagation, and consequently less spectral broadening can occur. However, choosing thicker than a few mm Si and YAG has disadvantages, as both materials are highly dispersive in this spectral region, meaning that after some propagation the pulse stretches and intensity decreases. As a result, SPM usually occurs in the first few millimeters of propagation. The accumulated dispersion is also problematic as material STOD is always positive, which means it cannot be compensated by bulk compression. For the above reasons, a 2 mm thick YAG crystal and a 1 mm Si crystal were chosen.

The MIR laser of ELI-ALPS delivered 50 fs compressed pulses, and 43 fs FTL pulse duration at the time of the experiment calculated from Equation (II-39). Fine dispersion tuning before post-compression was performed with the Dazzler in the OPCPA system to optimize pulse compression for the spectral broadening in the plates. We focused 11 W average power

from the laser using a gold coated concave spherical mirror with a focal length of f = 500 mm to avoid plasma formation in ambient air. We tuned the laser intensities on the front surfaces of the plates by changing their distance from the focus point, and always kept them in the diverging beam behind the focus point. The goal was to eventually achieve close to 2-cycle FWHM recompressed pulse duration, which practically requires a broad spectrum with shorter than 2-cycle FTL pulse duration to have some margin. Meanwhile, linear and nonlinear losses should be as low as possible to avoid excessive decrease in power and minimize the chance for optical damage in the plates.

The output energy was calculated from the measured average power right after the plate(s) with a thermopile power meter (UP55M-500W-H12-D0, Gentec-EO). Peak intensities were estimated on the basis of the beam diameter at the plates positions and temporal characterization (see Chapter III.3.3). The beam diameter was measured with a pyroelectric scanning slit beam profiler (Nanoscan, Ophir).

The first test only involved an uncoated YAG crystal inserted at Brewster's angle [137] to minimize surface losses. Moving the YAG close to the focus caused spectral instability. In addition, visible filamentation in the material and self-focusing of the beam was be observed, together with significant optical losses from nonlinear processes (similarly to those described for a CaF_2 plate in reference [138]). Increasing the intensity even further caused optical damage on the second surface of the YAG crystal due to critical self-focusing. When laser intensities exceeded 380 GW/cm^2, the YAG crystal suffered optical damage. This is in stark contrast with the results obtained by Faming Lu, et al. [100], where 1000 GW/cm^2 laser intensities were reached on a YAG crystal without such an issue. The reason for this difference is most likely due to the fact that the MIR laser operates at 100 kHz repetition rate compared to the 300 Hz laser system used by Faming Lu et al., which causes a significant increase in irradiance. According to an article by V. Shumakova et al. [99], even 2500 GW/cm^2 mid-IR laser intensity was tested on a YAG crystal without damage although only at 20 Hz repetition rate. Most probably, the high irradiance of kHz repetition rate pulse trains can have cumulative and thermal effects in the YAG crystal plate leading to optical damage. The YAG plate was placed after the focus (measured to be 505 mm from the focusing mirror), so the divergence somewhat compensated for the nonlinear self-focusing effect. The ideal position was found to be at 525 mm from the focusing mirror, where the absorption loss was only 2%.

Next we investigated the optimal distance of the AR coated 1 mm thick Si plate from the focus (without the YAG plate), with the method previously applied to the YAG plate. No visible filament could be observed as Si is not transparent in visible light. Yet, by monitoring the transmission we could see when nonlinear absorption became significant and the output beam profile distorted. Optical damage of the AR coating was also observed at peak intensities above 300 GW/cm^2. The ideal position was found to be at 580 mm from the focusing mirror with 14% absorption loss.

Finally, the combination of the two plates were tested. By inserting the YAG plate into the beam path first at the previously determined optimal position, the pulses are close to being self-compressed [99], which was proven by SH-FROG temporal characterization described in Chapter III.3.3 with a pulse duration of 36.8 fs, reconstructed with RMS error of 0.71%. These pulses have higher peak power than the input pulses without a compressor. By optimizing the Si plate position relative to the focus (675 mm after the focusing mirror) we could achieve a

broader spectrum with the two-plate arrangement, with an overall absorption loss of 11%. The empirically determined ideal positions are shown in Table 10. The resulting spectra were measured by Mozza, the multi-octave spectrum analyzer, and they are shown in Fig. 46.

Material (position)	Peak intensity [GW/cm^2]	Absorption loss [%]	Output energy [μJ]	FTL [fs]
YAG (525 mm)	275	2	104	34.4
Si (580 mm)	207	14	92	21.4
YAG (525 mm) & Si (675 mm)	275 & 77	11	92	17.5

Table 10. Measured parameters of the thin-plate compression setup. The FTL duration was calculated from the measured spectra. The values in brackets refer to the distance of the given plate from the focusing mirror.

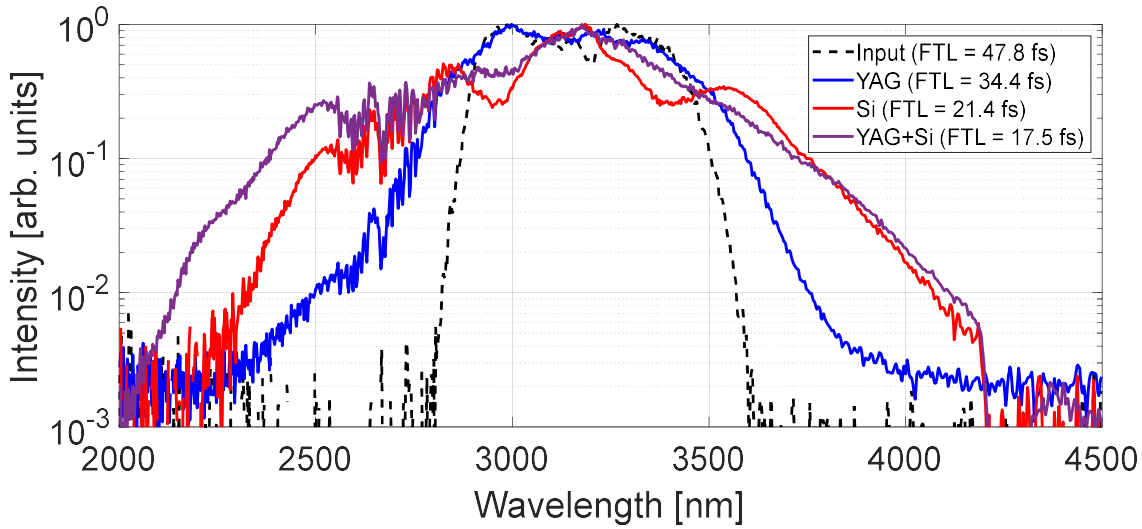

Fig. 46. Measured spectral broadening in different post-compression schemes. Input spectrum for reference (black), with only a single YAG crystal at 525 mm (blue), only a single Si crystal at 580 mm (red), and with a YAG crystal at 525 mm and an Si crystal at 675 mm together (purple). [139]

By comparing the spectral broadening of different post-compression schemes in Table 10, I concluded that using single plates alone and pushing the spectral broadening beyond the 2-3 cycle FTL bandwidth is impractical due to excessive losses, beam distortions and heavy energy fluctuations. For this reason, the combination of YAG and Si plates was used to spectrally broaden the pulses of the MIR laser. Furthermore, after the Si plate, the pulses are positively chirped, which allows for the fine-tuning of pulse compression with a bulk compressor or wedge pair made of fluoride crystal or mid-IR transmitting glass. The finalized scheme for post-compression is shown in Fig. 47. The diagnostic methods and devices are detailed in the next chapters.

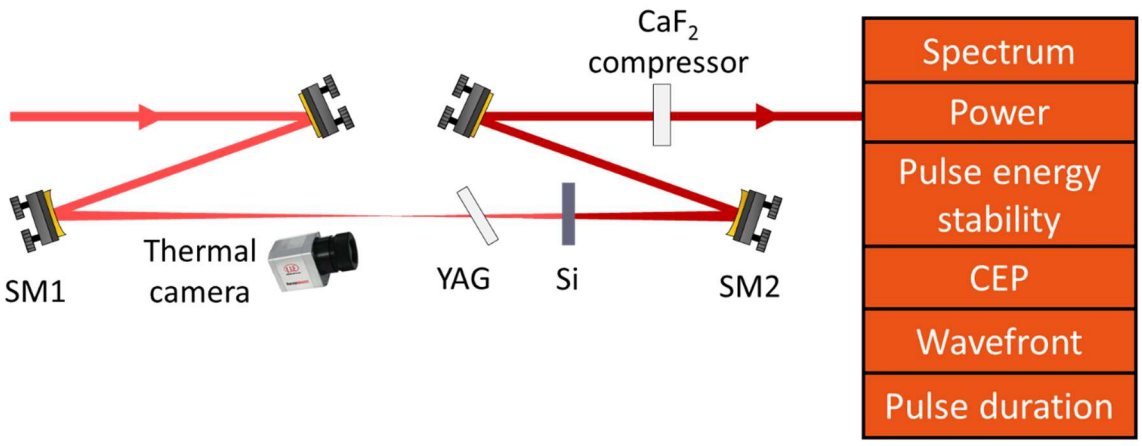

Fig. 47. Schematic view of the post-compression arrangement and the laser diagnostics used for characterization. SM1 and SM2 are concave spherical mirrors. Spectral, power, pulse energy and the CEP stability are measured continuously in parallel with one another, while wavefront and pulse duration measurements were occasionally performed separately from the other measurements.

The final configuration of YAG (at 525 mm) at Brewster's angle and AR coated Si (at 675 mm) provided 9.2 W average power (right after the Si plate) with a broad spectrum supporting 17.5 fs FTL duration. The B-integral accumulated in the YAG and the Si plates was also calculated using the intensities and the thickness of the plates, and it was determined to be 0.7 rad in the YAG plate and 3.96 rad in the Si plate. Note that while air is fully transparent for the whole spectral range of the MIR laser, the broadened spectrum overlaps with the spectral absorption bands of some composites of air i.e. CO_2 and water vapor. The spectral hole observed at 4.2–4.3 µm is caused by CO_2 absorption, while the modulation at 2.6–2.7 µm is due to the absorption of water vapor in the air of the laboratory (40% relative humidity).

After propagation through the two plates, the two-dimensional beam profile exhibits a sinc like intensity distribution due to the spatial Kerr effect. After the nonlinear crystal plate, a spherical mirror (SM2) collimates the spectrally broadened beam to 8 mm diameter (at $1/e^2$ intensity level). The highly divergent outer rings of the beam are filtered by the very same spherical mirror, as only the central peak of the beam is reflected. This incurs an additional net loss of 2 W average power, but also reduces spectral-temporal coupling.

III.3.3. Compression and temporal characterization

The temporal characterization of the compressed pulses was performed by two independent devices separately. One of them is based on the SH-FROG technique [140], where an SH based nonlinear autocorrelator is used, coupled with spectral measurement, and full temporal intensity and phase is recovered by an iterative algorithm. Based on this design, a home-built all-reflective FROG device was constructed, as shown in Fig. 48. The two arms of the autocorrelator were separated and recombined by D-shaped mirrors to avoid dispersion from beam splitters. A 100 µm thick AGS crystal (θ=36.6°) was used for the SHG process, with a spectral acceptance bandwidth of 4100 cm^{-1} (i.e. from 1.9 µm to 8 µm), which was sufficient to measure the post-compressed pulses. After the crystal, three beams propagated in different directions. There were two side beams coming from the two arms of the autocollimator and a third beam generated by the SFG process in the crystal. The side beams were filtered by an iris,

and the remaining SFG beam was focused into an InGaAs based grating spectrometer (NIR-QUEST512-2.5, Ocean Optics).

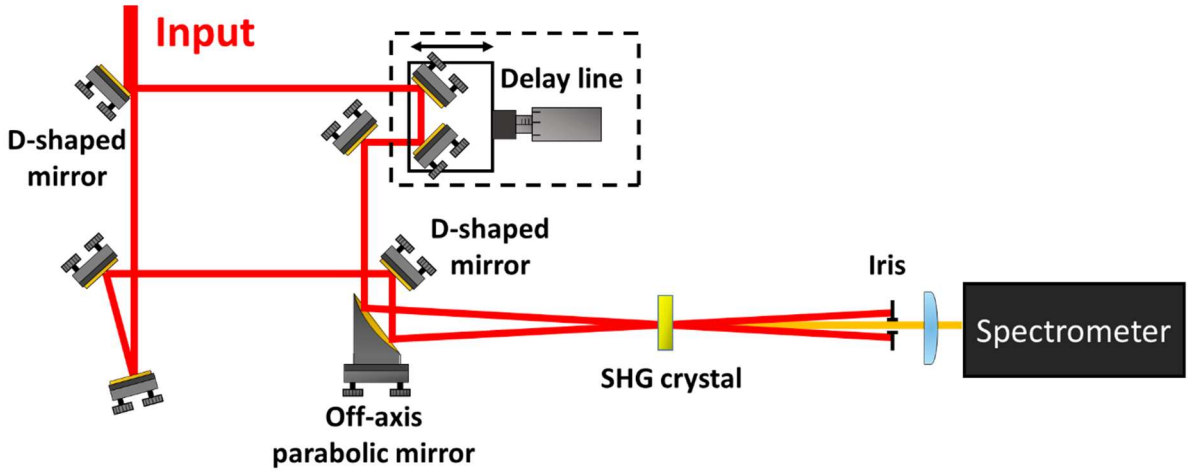

Fig. 48. All reflective SH-FROG. The beam is separated and recombined in the autocorrelator by a D-shaped mirror to avoid any dispersion. The SHG crystal is a broadband 100 µm thick AGS crystal (θ=36.6°).

For the bulk compressor different thickness (2, 3.3, 4 and 5 mm), negative GVD CaF_2 optical windows were tested, which were available at the lab at the time of the experiment. The aim was to achieve the shortest possible pulse duration. The FROG measurement of these compressed pulses are compared in Table 1.

Compressor type	No compressor	2 mm CaF_2	3.3 mm CaF_2	4 mm CaF_2	5 mm CaF_2
Pulse duration	70.9 fs	35.8 fs	22.8 fs	27.6 fs	34.5 fs

Table 11. FWHM pulse durations calculated from the measured FROG traces, with different thickness CaF_2 plates used as a bulk compressor.

It can be concluded that 3.3 mm thick CaF_2 provided the shortest, 22.8 fs FWHM pulses, reconstructed with 1.06% RMS error. The measured and the reconstructed SH-FROG traces are displayed in Fig. 49 (a-b), respectively. The reconstructed temporal profile and the corresponding spectrum with spectral phase is shown in Fig. 52 (a) and (c), respectively.

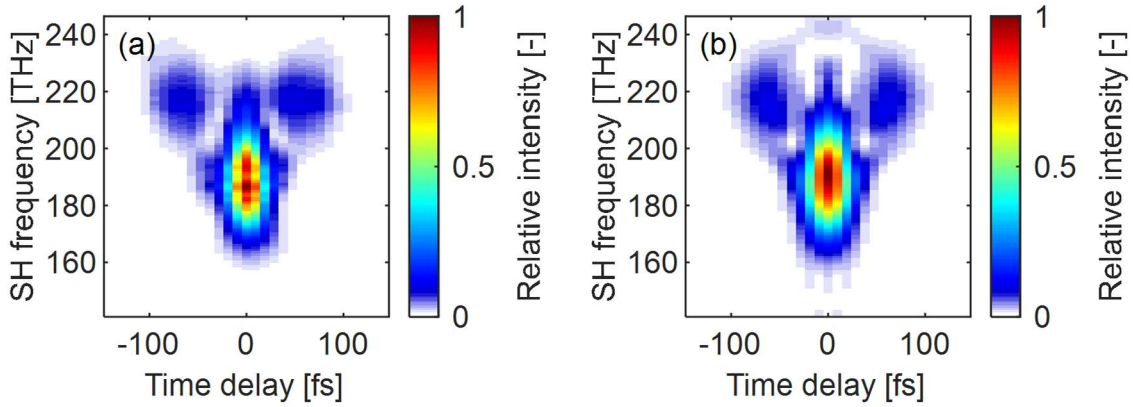

Fig. 49. (a) Measured SH-FROG trace of the post-compressed pulse with 3.3 mm thick CaF_2 bulk compressor. (b) Reconstructed SH-FROG trace using an iterative algorithm with a global error of 1.06% RMS. The reconstructed FWHM pulse duration is 22.8 fs. [139]

An alternative temporal characterization measurement was performed using a relatively new method named TIPTOE (tunneling ionization with a perturbation for the time-domain observation of an electric field) [141]. The TIPTOE setup is visualized in Fig. 50. As detailed in reference [142], the input beam is divided into two parts. This was achieved by a reflective optic: a segmented flat mirror. The relative delay between the outer and inner beam segments was controlled by the piezo-controlled center segment. The separated beams were focused between a pair of metal electrodes using an off-axis parabola with a focal length of 5 cm. The modulation of the ionization yield was measured as a function of time delay. Then a focusing holey mirror was used to refocus the outer beam between a second pair of electrodes. This way a reference yield could be obtained, and inherent laser fluctuations can could be accounted for. The measured and reconstructed ionization yield signals as a function of delay are visualized in Fig. 51. The reconstruction algorithm computes the electric field and phase of the measured pulses using the ionization yield modulation function.

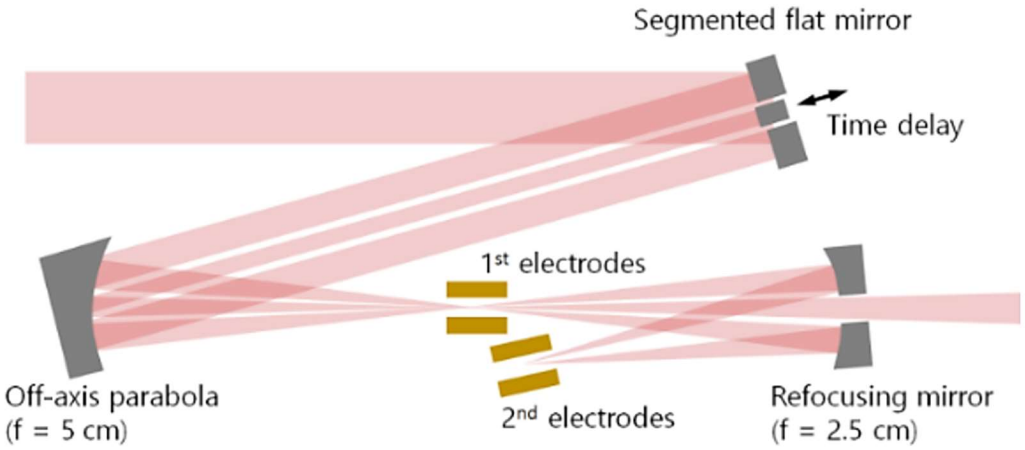

Fig. 50. Schematic representation of the all-reflective TIPTOE setup. The modulation of the total ionization yield is recorded as a function of time delay, from which the post-compressed pulses can be temporally characterized. [139]

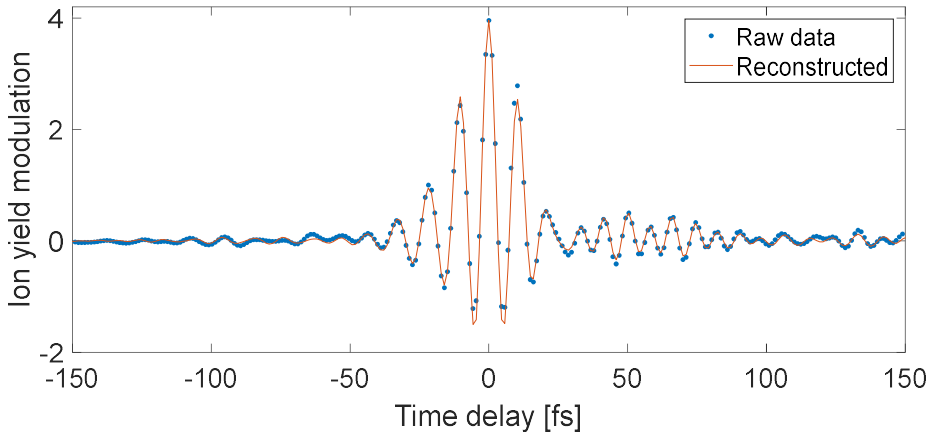

Fig. 51. Raw (blue dots) ionization yield modulation from the TIPTOE measurement and the reconstructed ionization yield (red line). It is not to be confused with the electric field of the laser pulse. The complex electric field of the signal pulse can be reconstructed from the measured ionization yield data. [139]

From the TIPTOE measurement, the reconstructed FWHM pulse duration was found to be 23.5 fs (2.3 cycles) after recompression, which is identical with the pulse duration obtained by the SH-FROG within a difference of 1 fs. The temporal and spectral intensity distribution of the post-compressed pulses measured by the two methods are displayed and compared in Fig.

52 (a-d). The two fundamentally different techniques yielded very similar results both in the temporal and spectral domains. Based on these results, it can be concluded that the recompressed pulse duration is no more than 2.3 optical cycles (FWHM). In Fig. 52 (c), the spectral phase retrieved from the FROG trace has a local extremum at around 2.6 µm (115 THz). In Fig. 52 (d), the same phase measured by the TIPTOE method is heavily modulated. This can be attributed to the water vapor absorption in the air. It can also be observed in Fig. 49 (a), where at the higher SH frequencies the FROG trace has a double peak structure at 60 and –60 fs positions. This phase distortion can also limit the further broadening and compressibility of the pulses. Temporal side peaks can be observed in Fig. 52 (a, b), by both the TIPTOE and the SH-FROG measurements. As TIPTOE (unlike the SH-FROG) is sensitive to the direction of time, it confirms that these peaks are post-pulses. Based on the reconstructed complex temporal distributions, the temporal Strehl ratio (defined by the ratio of the peak power of the measured and that of the transform-limited pulse shape) is 0.73, with 90% of the full pulse energy contained in the main peak.

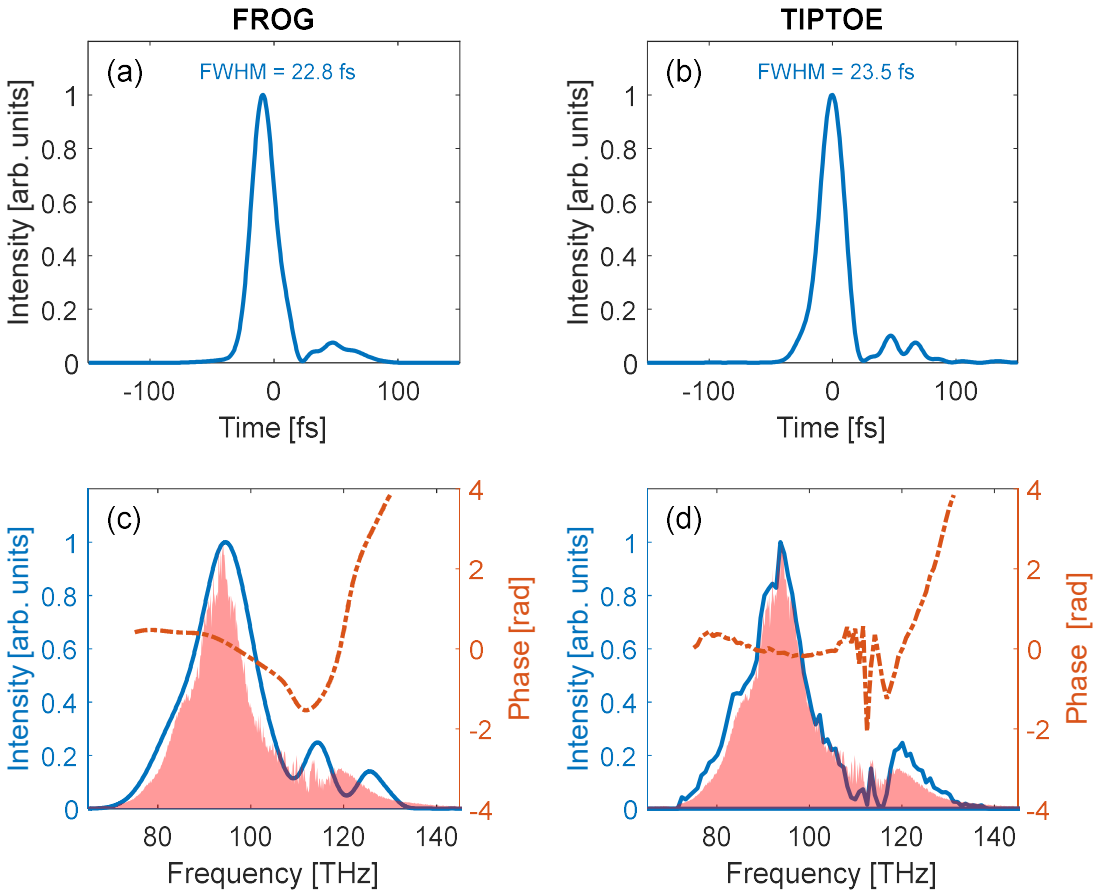

Fig. 52. (a) The reconstructed temporal intensity distribution of the SH-FROG measurement, yielding an FWHM pulse duration of 22.8 fs. (b) The temporal intensity distribution reconstructed from TIPTOE yielding 23.5 fs FWHM pulse duration. (c) The reconstructed spectral intensity (blue line) and phase (orange dashed line) from the SH-FROG compared to the spectral measurement performed by Mozza (pink area). (d) The spectral intensity (blue line) and phase (orange dashed line) from TIPTOE measurement and the spectral measurement performed by Mozza (pink area). [139]

In conclusion, the remaining beam with 7.2 W average power was recompressed in an uncoated CaF_2 bulk compressor with negative GVD. The beam diameter was big enough, so no SPM occurred in the compressor. Due to Fresnel losses, the final output average power was 6.8 W (68 µJ per pulse).

III.3.4. Long-term stability and wavefront measurement

As mentioned earlier, several experiments benefit from using the post-compressed pulses of the MIR system as the source. Importantly, these experiments would require good long-term stability of the laser parameters to provide stable conditions during measurements. To verify the long-term stability of the post-compressed beam, multiple eight-hour stability measurements were performed simultaneously. The delocalized CEP was measured after the post-compression scheme by Fringeezz (undersampled 10 kHz) and stabilized by sending the feedback signal to the Dazzler. During this eight-hour period, 288 million pulses were measured, and the CEP noise was found to be 82 mrad RMS, as displayed in Fig. 53 (a). The stabilized CEP contained a high frequency noise component, which the stabilization feedback loop was unable to correct, making some of the CEP values jump out compared to the overall average. However, these outliers are a minority, as they only represent less than 5 percent of all measured data points, and the rest are all within the ±150 mrad interval of the average.

Long-term energy stability measurement was performed by focusing a leakage of the main beam into a mid-IR sensitive InAsSb Amplified Detector (PDA10PT-EC, Thorlabs). The resulting single-shot pulse energy stability was 2.4% RMS. An additional power stability measurement was performed with the Gentec-EO thermophile power meter, which is not capable of single-shot operation, and was consequently unable to resolve fast oscillating noises. The measured RMS stability of the average power during the same eight-hour period was 0.9%, shown in Fig. 53 (b). Furthermore, spectral intensity changes were also monitored during this period with the Mozza spectrum analyzer, displayed in Fig. 53 (c). The resulting FTL pulse duration RMS stability was 1.1%.

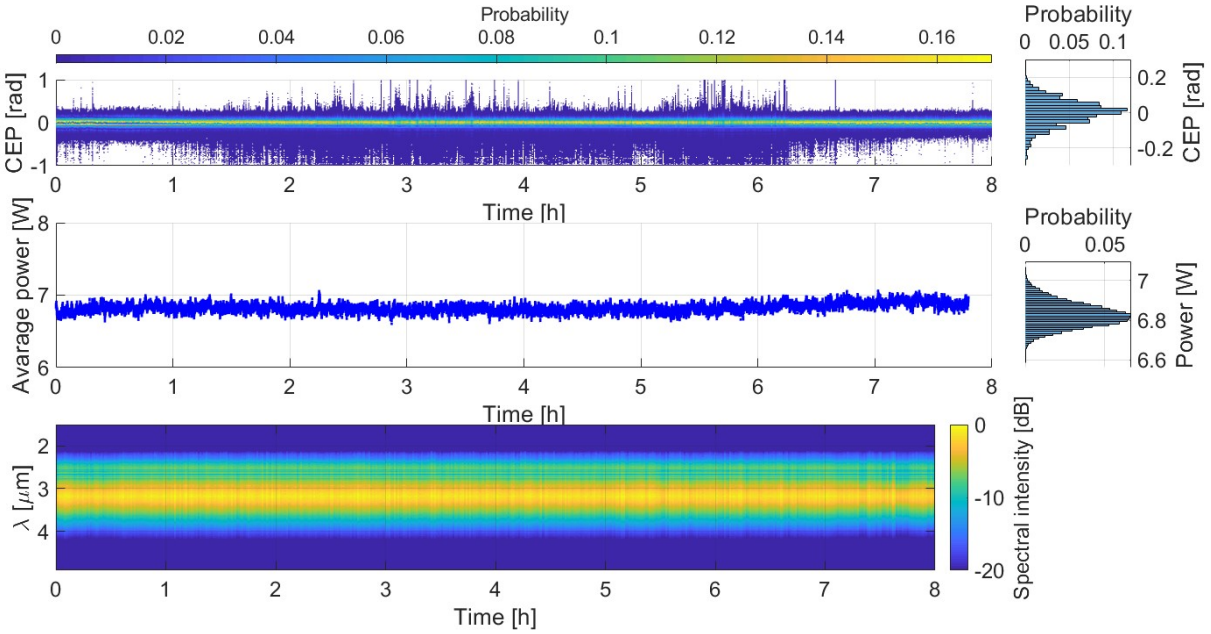

Fig. 53. Eight-hour long stability of different laser parameters of the post-compressed pulses. (a) the CEP stability as measured by Fringeezz; (b) the power stability as measured by power meter; (c) the recorded spectral intensity as measured with Mozza spectrometer. [139]

After several days of prolonged use of the post-compression setup during a user experiment, damage was observed at the back (output) surface of the YAG. This significantly affected the beam quality, which led us realize the issue. The reason for the damage is most likely due to

the high irradiance on the YAG crystal, which is close to the damage threshold of the material. A possible explanation is that small disturbances in the OPCPA or in the air during propagation can increase irradiance on the surface, which can lead to optical damage. After the damage was noticed, the YAG plate was moved laterally so the beam would not overlap with the damage spot; as a result, all previous parameters were restored. No damage was ever noticed on the Si plate during operation.

Using a wavefront sensor (SID4-DWIR, Phasics), the near field spatial intensity distribution of the post-compressed beam was also measured on the same day, as shown in Fig. 54 (a). From the waveform the peak-to-valley value of the phase map was 0.3 λ, while the RMS of the phase map was 0.061 λ, where λ is 3.1 μm, the central wavelength of the post-compressed pulse. The Strehl ratio was calculated to be as high as 0.97 from the wavefront measurement, as the peak focal intensity in the aberrated point spread functions divided by the peak focal intensity of the ideal point spread function. The far field distribution was calculated using 2D FT of the measured complex near field distribution, and it is shown in Fig. 54 (b).

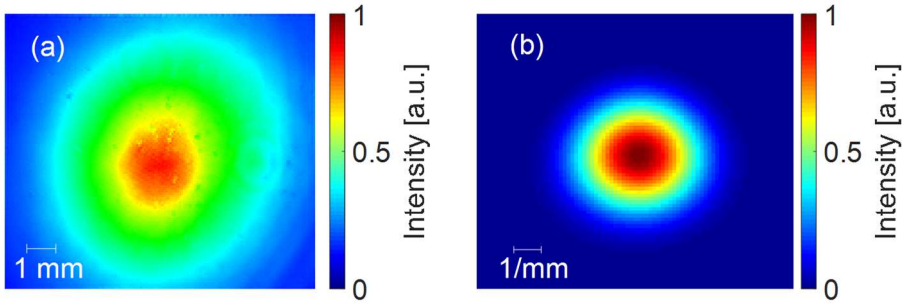

Fig. 54. (a) Near field spatial distribution of the post-compressed beam reconstructed from the wavefront sensor measurement. (b) The same wavefront was used to calculate the far field intensity distribution. [139]

III.3.5. Thermal monitoring and pulse energy upscaling simulation

As a consequence of the relatively high average power of the input beam, the temperature in the nonlinear crystals was expected to rise due to multiphoton absorption, which can lead to unintended side-effects. To monitor these temperature changes in the Si and YAG crystals during operation, a thermal camera (TIM-200, Micro-Epsilon) was employed. After seven minutes of operation, thermal equilibrium was reached on both crystals, where heat losses from thermal conductivity and thermal radiation balance out heat gain from absorption. The temperature distributions along the front surfaces are shown in Fig. 55 (a, b). The temperature increased by more than 10 °C in the YAG, however the peak temperature was not higher than 32.1 °C even at full power after prolonged use. Furthermore, no significant change in the spectrum was observed by comparing the spectra measured at the beginning of the experiment and after thermal equilibrium was reached. The sensitivity range of the thermal camera is between 8 μm to 13 μm, which overlaps with the transmission window of the Si crystal. As a result, the thermal camera perceives the Si crystal as semi-transparent, meaning that only the temperature of the mount itself is representative.

To determine the temperature of the Si plate, Dr. Roland Nagymihály performed a 3D thermal simulation in COMSOL Multiphysics [143]. The measured temperature distribution of the Si mount was used as a reference, the absorbed power was calculated from the multiphoton (3 and 4 photon) absorption coefficients of Si [144,145]. The thermal conductivity of Si is 163.3 W/(m·K), which was also obtained from literature [146]. The measured power loss after

the Si plate was compared with the theoretical values, and good agreement was found, which demonstrated the reliability of the heat source in our numerical model. Passive cooling of Si by the ambient air of the laboratory was approximated to account to a heat flux with a heat transfer coefficient of 5 W/(m^2·K). The loss in optical power served as the heat source in the thermal model, which consisted of the aluminum mount and the Si crystal plate, as shown in Fig. 55 (c). Cooling through the contact between the mount and plate amount was adjusted according to the resulting temperature distribution of the mount, which fit the measurement in case of a heat transfer coefficient of 470 W/(m^2·K). Based on this, the calculated peak temperature on the Si plate should be only a few degrees higher compared to the mount. Consequently, no active cooling was necessary for the nonlinear crystals.

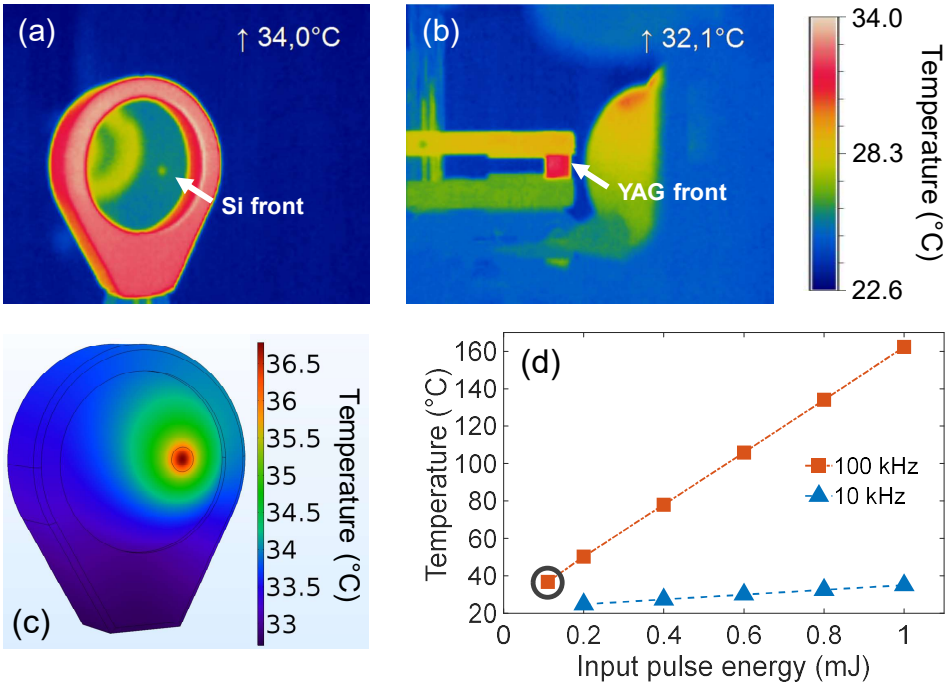

Fig. 55. Thermal camera images of the front surfaces of Si (a) and YAG (b) crystals in their mounts after reaching thermal equilibrium. The temperature in the upper right corner refers to the maximum temperature of the images. (c) The temperature distribution of Si and its mount determined by a 3D COMSOL Multiphysics simulation. (d) Simulation results for peak temperature in the Si plate at higher pulse energies at 100 and 10 kHz repetition rates. The measured data point is denoted by a gray circle. [139]

We have seen in Chapter II.6. that higher and higher pulse energy and average power mid-IR laser system are being built as technology matures. To investigate how the same post-compression method could be employed for future laser systems, upscaling simulations were performed by Dr. Roland Nagymihály with pulses up to 1 mJ input energy, conducted at 10 and 100 kHz repetition rates using the COMSOL model of the Si mount assembly. The peak intensity in the Si crystal was kept at a constant level by changing the beam diameter, similarly to how the optimal peak intensity for spectral broadening was achieved experimentally. The peak temperature values in the Si crystal in thermal equilibrium for different pulse energies at 10 and 100 kHz repetition rates can be seen in Fig. 55 (d). At 100 kHz, even with 200 µJ pulses (20 W average power) a peak temperature of 50 °C is predicted, and the peak temperature linearly increases with pulse energy reaching 162 °C at 1 mJ (100 W average power). This high temperature would cause multitude of issues, like thermal expansion of the plate and mount, thermal lensing, the overheated air, which would disturb the laser beam. In addition, high temperature would change the Si bandgap structure altering the nonlinear interaction. In such

cases, active cooling of the material can be employed to keep the Si at room temperature during operation. The highest peak temperature at 10 kHz repetition rate with 1 mJ pulses (10 W average power) was only 35 °C. No active cooling would be necessary in this case either.

III.3.6. Outline

In conclusion, I have demonstrated a thin-plate post-compression arrangement for a mid-IR laser with the highest average power, to the best of my knowledge. The 11 W average power of this laser was used for this experiment. The pulses were compressed from 50 fs to 23 fs (2.3 cycle), after which an average power of 6.8 W remained at the output. As the main goal for the post-compression was to provide a stable driving source for ultrafast applications in strong-field science and CEP sensitive time-resolved experiments, we placed great emphasis on the long-term stability of the laser parameters. The CEP, average power and output spectrum of the laser were monitored for eight hours continuously, revealing somewhat degraded performance compared to the OPCPA output, but long-term stability was still acceptable. This post-compressed beam proved to be very useful in practice as a successful commissioning user campaign was performed during the autumn of 2019. For more details and for the results see references [12,13].

Summary III. I have designed and built a thin-plate post-compression setup for the spectral broadening and compression of pulses from the MIR laser system. Overall, compression to 23 fs FWHM pulse duration was achieved from the 50 fs 100 kHz repetition rate mid-IR pulse train. I found that the combinations of YAG and Si materials are ideal for spectral broadening thanks to their linear and nonlinear optical properties. This was verified experimentally by using a 2 mm thick YAG and a 1 mm Si crystal plate, where intensities in the materials were fine-tuned by moving the plate positions with respect to the focusing mirror. Recompression to 23 fs pulse duration was achieved in a 3.3 mm thick CaF_2 bulk, proven by the measurement of two distinct diagnostic devices, SH-FROG and TIPTOE. Long-term pulse-to-pulse energy, power, spectrum and CEP stability of the output was monitored for 8 hours continuously, which proved that it can be utilized for long-term experiments.

IV. Summary

In this thesis multiple methods are presented for the improvement and diagnostics of the MIR laser, the few-cycle mid-IR OPCPA system of ELI-ALPS. CEP measuring devices do not measure the CEP shot-to-shot for 100 kHz repetition-rate laser systems (including the MIR laser), instead pulses are skipped periodically (undersampling) or multiple pulses are integrated together. The TOUCAN technique was developed to address this issue. A TOUCAN based measuring device capable of single-shot operation was employed for the delocalized CEP measurement of the MIR laser. Furthermore, a new SRI based method for the spectral phase shift characterization of optical elements was developed. This method is well-suited for ultrafast laser sources, and it is capable of dual-band operation. This method effectively doubles the recovered information compared to standard SRI techniques without increasing the required bandwidth of the spectrometer. Finally, a post-compression scheme was implemented for the MIR laser, preceded by detailed investigation to find the most suitable crystal materials for both spectral broadening and bulk compression. As a result, the pulses were compressed to half of their original duration, which was validated by two distinct temporal characterization methods. In short, the most important scientific results can be summarized in the following points:

I. I have developed an interferometric delocalized CEP measuring method, named TOUCAN, which is capable of single-shot measurements of few μJ energy pulses at higher repetition rates than ever before. The device was experimentally verified using the 100 kHz repetition rate MIR laser system. Shot-to-shot pulse energy change and temperature fluctuations as potential sources of measurement error were examined, and I have concluded that they have minimal effect on the accuracy of CEP measurements in the case of the examined laser. I have also shown that time jitter between the trigger and the detected photodetector signals significantly decreases the accuracy of the measurement. I have circumvented this issue by creating an additional interference in the detected signal and removed the effect of time jitter via post-processing. The analysis of the CEP noise showed overwhelmingly high frequency noise components, which proves that CEP measurement and stabilization at full repetition rate is necessary to further reduce CEP noise in the MIR laser system. [T1]

II. I have developed a technique called dual-band SRI to characterize the spectral phase shift of optical elements at the fundamental and SH frequency bands of an ultrafast laser source simultaneously from interferograms recorded exclusively at the SH frequency band. The technique was first examined by theoretical description and numerical simulation, and was then tested experimentally. I built a dual-band SRI device, and performed measurements using 9 μJ energy pulses from the MIR laser system. The spectral phase shift of well-known optical materials was measured, which verified both the technique and the device. Furthermore, I have proven that a single measured interferogram holds double the information necessary for the complete reconstruction of the spectral phase shift at both bands, by employing and comparing different evaluation methods. By using the wave theory description of dual-band SRI, I examined further extensions of the method to measure more than two frequency bands simultaneously. [T2]

III. I have designed and built a thin-plate post-compression setup for the spectral broadening and compression of pulses from the MIR laser system. Overall, compression to 23 fs FWHM pulse duration was achieved from the 50 fs 100 kHz repetition rate mid-IR pulse train. I found that the combinations of YAG and Si materials are ideal for spectral broadening thanks to their linear and nonlinear optical properties. This was verified experimentally by using a 2 mm thick YAG and a 1 mm Si crystal plate, where intensities in the materials were fine-tuned by moving the plate positions with respect to the focusing mirror. Recompression to 23 fs pulse duration was achieved in a 3.3 mm thick CaF_2 bulk, proven by the measurement of two distinct diagnostic devices, SH-FROG and TIPTOE. Long-term pulse-to-pulse energy, power, spectrum and CEP stability of the output was monitored for 8 hours continuously, which proved that it can be utilized for long-term experiments. [T3]

V. Magyar nyelvű összefoglaló

V.1. Bevezetés

A közép-infravörös lézerforrások jelentős fejlődésen mentek keresztül az elmúlt évtizedekben. E technológiai forradalmat a közép-infravörös források számos felhasználási lehetősége tüzelte, mint például erős-terek fizikája szilárd állapotú anyagokban, időbontott spektroszkópia vagy éppen a távérzékelés, hogy csak néhányat említsünk. Az egyik legígéretesebb alkalmazási terület az attoszekundumos folyamatok vizsgálata. Az attoszekundumos impulzusok keltése a néhány ciklusú lézerimpulzusokkal történő magasharmonikus-keltésen alapul. A keltés folyamata erősen nemlineáris, a maximális keltett fotonenergia a ponderomotoros erőtől függ, ami a lézer hullámhosszával négyzetesen skálázódik. Ennek köszönhetően nagy hullámhosszú lézerek szélesebb magasharmonikus spektrumot eredményeznek, ami még rövidebb, attoszekundumos impulzusok előállítását teszi elviekben lehetővé. Ugyanakkor a keltés hatásfoka drasztikusan csökken a növekvő hullámhosszal. Széles spektrumú, elegendően nagy teljesítményű magasharmonikusok keltéséhez néhány ciklusú, nagy energiájú, fázisstabil, közép-infravörös lézerrendszerekre van szükség.

Manapság a leggyakoribb szilárdtest-lézerek neodímium (Nb^{3+}), itterbium (Yb^{3+}) vagy titán (Ti^{3+}) dópoló anyagot használnak, és a közeli infravörös tartományban sugároznak. Femtoszekundumos közép-infravörös lézerek csak a századforduló környékén kezdtek megjelenni. A gyakran használt lézerkomponensek, mint a diszperzív tükrök, nagy reflexiójú bevonatok, akusztooptikai fénymodulátorok, stb., rosszabb paraméterekkel rendelkeznek a közeli infravörösben elérhető társaikhoz képest, jelentősen drágábbak, és csupán néhány cég gyártja őket világszerte. Továbbá, a közeli infravörös lézerek szilícium alapú detektorokat alkalmaznak, ami a felvezetőipar leggyakoribb alapanyaga. A szilícium viszont alkalmatlan közép-infravörös sugárzás detektálására, így helyette pl. InAsSb, vagy HgCdTe vegyes félvezetőből készült detektorokat szoktak használni. Ám ezek rosszabb paraméterekkel rendelkeznek és előállítási költségük is magasabb. Mivel a közép-infravörös detektorsoroknál vagy kameráknál az árkülönbség még jelentősebb, sok közép-infravörös lézerdiagnosztikai eszköz alternatív megoldásokat alkalmaz. A kutatásom célja a közép-infravörös diagnosztikai eszközök palettájának bővítése volt új, kevésbé költséges és egyszerű módszerek kifejlesztésével.

A III. fejezetben ismertetem a saját kutatásomat, azon belül három új, ultragyors közép-infravörös lézerekhez kifejlesztett módszert mutatok be. A kísérletek túlnyomó részénél az ELI-ALPS MIR lézerrendszerét használtam. E lézerrendszer közel 4 ciklusú lézerimpulzusokat generál 3,2 μm központi hullámhossznál 100 kHz ismétlési frekvenciával. A lézer átlagteljesítménye 14 W (140 μJ/impulzus), ami azt jelenti, hogy egy-egy impulzus csúcsteljesítménye 3,3 GW.

A disszertációmban bemutatott kísérletek az ELI-ALPS laboratóriumaiban (ELI-HU Non-profit Ltd.) végrehajtott kísérleteken alapulnak. A TOUCAN módszerhez az előzetes kísérletre a Bordeaux-i Egyetemen került sor, Eric Cormier felügyelete alatt. A Gwangju Institute of Science and Technology nevű intézményben fejlesztették ki a TIPTOE módszert, amely hasznos referenciamérést biztosított a posztkompresszált (utólagosan összenyomott) impulzusok időbeli karakterizációjához.

V.2. Tudományos előzmények

Közép-infravörös sugárzás:

A fény leírható transzverzális elektromágneses hullámonként, amelynek tulajdonságai a hullámegyenlet megoldásából számolhatók. Elsősorban a hullámhosszával vagy frekvenciájával jellemezhető, ami alapján több kategóriába csoportosítható. Az emberi szem nagyjából a 400–700 nm-es hullámhossztartományon érzékeny, amelyet ezért látható fénynek hívunk. Az ennél hosszabb hullámhosszú sugárzást nevezzük infravörösnek, amit tovább csoportosíthatunk közeli, rövid, közép-, és hosszú hullámhosszú infravörösre. A fenti csoportosítás alapja a fény-anyag kölcsönhatás mikroszkopikus mechanizmusainak hullámhosszfüggése. Ebből az elemi különbségből következik, hogy a közeli infravörösben működő optikák és detektorok a közép-infravörösben nem, illetve csak részben használhatók.

Diszperzió:

Polikromatikus fény esetén a hullámegyenlet megoldása megadható különböző frekvenciájú monokromatikus hullámok szuperpozíciójaként. Az impulzusüzemű lézereknél a szállított energia időben rövid impulzusokba tömörül össze, így nagyobb csúcsintenzitás érhető el, mint a folytonos üzemű lézereknél. Ezen impulzusok is felbonthatók spektrális komponensekre, amelyek együttesen az impulzus spektrumát adják. A diszperzió jelensége az impulzust alkotó monokromatikus hullámok sebessége közötti különbségből fakad, aminek következtében egy optikai impulzus időben megnyúlik, illetve megrövidül. Egy adott spektrumhoz tartozó legrövidebb impulzusidő (transzformáció-limitált impulzushossz) úgy érhető el, ha a teljes diszperzió kompenzálásra kerül. Ez a lézerimpulzusok nyújtásának és kompressziójának elve, amely lehetővé tette a csörpölt impulzuserősítési séma (Chirped Pulse Amplification, CPA) elterjedését.

Nemlineáris optika:

Ha ez elektromágneses térnek elég nagy az intenzitása, az anyagban indukált polarizáció már nem lineárisan függ az őt keltő elektromos térerősségtől. Ennek következménye, hogy az anyag és tér kölcsönhatása során új elektromágneses hullámkomponensek jönnek létre az eredeti hullámoktól eltérő frekvenciákkal. Ezek a folyamatok osztályozhatók aszerint, hogy hány hullám kölcsönhatásáról van szó. Három hullám keverésére példa a másodharmonikus-keltés (second harmonic generation, SHG) ahol a létrejövő lézerimpulzus az eredeti fundamentális lézerimpulzus frekvenciájának kétszeresénél jelenik meg. Belátható, hogy a másodharmonikus impulzus spektrális fázisa a fundamentális fázisának kétszerese egy konstans értékkel eltolva. Ez a tény fontos szerepet játszik az f-to-2f és a dual-band SRI módszereknél. Négy hullám keverésére példa az önfázis-moduláció (SPM), amelynek következtében az impulzus spektruma kiszélesedik, és az elérhető legrövidebb impulzusidő csökken. Ezen az elven működnek a posztkompressziós módszerek.

Interferometria:

Két koherens, azonos frekvenciájú és polarizációjú fényhullám-komponens interferenciája során keletkező eredő tér az alkotó hullámok amplitúdóinak fázishelyes szuperpozíciójaként adható meg. Általánosságban, az eredő teret időben és térben intenzitásmaximumok és -minimumok jellemezik, a hullámok közötti fáziskülönbség függvényében. Az

intenzitásspektrum egy közvetlenül mérhető mennyiség, ugyanakkor az amplitúdó és a spektrális fázis – és így a két hullám közötti fáziskülönbség – csak interferometrikus módszerrel mérhető. A spektrálisan bontott interferometria (spectrally resolved interferomerty, SRI) ezt az elvet alkalmazva optikai elemek diszperziójának mérését teszi lehetővé. Az interferogram felvételéhez spektrális mérés szükséges, ahol a nyert információ a koherens fényforrás spektrális tartományára korlátozódik.

Vivő-burkoló fázis:

Egy lézerimpulzus térerősségének időbeli alakja az impulzus burkolójának és a periodikusan oszcilláló vivőhullámnak a szorzataként írható le. A burkoló és a vivőhullám közötti fáziskülönbséget, ami impulzusról impulzusra változhat, vivő-burkoló fázisnak, röviden CEP-nek (carrier-envelope phase) nevezzük. Ha a lézerimpulzus kellően rövid (néhány optikai ciklus hosszúságú), akkor a CEP-érték drasztikusan befolyásolja az impulzus térerősségének időbeli eloszlását, következésképpen az extrém nemlineáris optikai folyamatok (ionizáció, visszaszóródás) kimenetelét. Emiatt e kísérleteknél nélkülözhetetlen a CEP-érték változásának nyomon követése, illetve az impulzusok CEP-stabilizálása. A CEP-érték változásának egylövéses mérésére számos módszert fejlesztettek ki az elmúlt két évtizedben. Az egylövéses CEP-mérések két csoportba sorolhatók aszerint, hogy az alkalmazott módszer nemlineáris interferometrián vagy ionizáción alapul. Az interferometrián alapuló módszerek előnye, hogy alacsony csúcsteljesítménynél is működnek, míg az ionizációs módszerek előnye, hogy nagy ismétlési frekvencián is lehet egylövéses méréseket végrehajtani velük.

V.3. Eredmények

Disszertációmban három olyan módszert mutattam be, amelyek célja a MIR lézerrendszer és a hozzákapcsolódó diagnosztikák fejlesztése. Az első technika a TOUCAN (**T**emporal dispersion based **O**ne-shot **U**ltrafast **C**arrier envelope phase **AN**alysis) módszer, amit a III.1 fejezetben mutattam be. A TOUCAN módszer a CEP egylövéses mérését teszi lehetővé a piacon elérhető termékek sebességénél gyorsabban. A piaci CEP mérő eszközök nagy ismétlési frekvencián (>10 kHz) vagy periodikusan kihagynak impulzusokat a mérés során, vagy több impulzus által közösen keltett válaszjelet mérnek. A 100 kHz-es 140 μJ-os MIR lézer is olyan rendszer, amelynek az egylövéses mérésére sem ionizációs, sem hagyományos interferometrián alapuló módszerek nem alkalmasak. Ezt az akadályt a TOUCAN módszeren alapuló eszköz kifejlesztésével sikerült leküzdeni, amellyel egylövéses CEP mérést végeztem a MIR lézerrendszer impulzusain. A mérés igazolásához a felvett adatokat egy párhuzamos CEP-méréssel vettettem össze, amely csökkentett ismétlési frekvencián, 10 kHz-en történt. Az összehasonlítás igazolta a TOUCAN-elvet, és az ez alapján készült eszköz megfelelő működését.

A III.2. fejezetben egy új, optikai elemek diszperziójának mérésére kifejlesztett SRI alapú módszert is bemutattam. A módszer segítségével a diszperzió egy interferogramból két spektrális tartományon párhuzamosan határozható meg, így a dual-band SRI nevet adtam neki. Ezt a két tartományt a felhasznált impulzusüzemű lézer emissziós spektruma határozza meg, a fundamentális tartomány az eredeti spektrális tartománya a lézernek, míg az SH tartomány a keltett másodharmonikus spektrumot fedi le. A Michelson interferométer alapú dual-band SRI elrendezésben a fundamentális és az SHG tartományokhoz tartozó interferenciák sűrűsége külön eltolóval állítható, ami lehetővé teszi a Fourier térben ezek azonosítását és

különválasztását. Mindezt szimulációval alátámasztottam, majd a mérőberendezést megépítve kísérletileg is igazoltam, jól ismert diszperziójú anyagok mérésével.

Végül a III.3. fejezetben a MIR lézerhez kifejlesztett vékonylemezes posztkompressziós elrendezést mutattam be. It soroltam fel azokat a szempontokat, amelyek alapján a kristályanyagok kiválasztása történt, mind a vékonylemezeknél a spektrális kiszélesítéshez, mind a tömbkompresszornál az impulzusok időbeli lerövidítéséhez. Legjobb tudomásom szerint ezt a módszert korábban még nem alkalmazták több mint 10 W átlagteljesítményű közép-infravörös lézernél. A módszer segítségével a közép-infravörös impulzusok hossza az eredeti közel felére csökkent. Mivel a módszert kifejezetten felhasználói kísérletekhez fejlesztették ki, a posztkompressziós elrendezésnél jelentős hangsúlyt fektettem a hosszú távú stabilitás vizsgálatára. A következő tézispontokban összefoglalom a legfontosabb tudományos eredményeimet:

I. Kifejlesztettem egy interferometrikus módszert a delokalizált CEP mérésére, amit TOUCAN módszernek neveztem el. A módszer képes néhány μJ energiájú impulzusok egylövéses mérésére, nagyobb ismétlési frekvenciával, mint bármely korábbi módszer. Az eszköz prototípusának tesztelése a 100 kHz ismétlési frekvencián üzemelő MIR lézerrel történt. Megvizsgáltam az impulzusok energiaváltozását és az optikai szál hőmérséklet-ingadozásait, mint lehetséges hibaforrásokat. Arra a következtetésre jutottam, hogy az adott lézer esetében ezek a jelenségek minimális hatással vannak a CEP mérés pontosságára. Megmutattam, hogy a trigger jel és a fotodetektor által érzékelt jel között megfigyelhető időbeli jitter jelentősen csökkenti a mérés pontosságát. Ezt a problémát úgy oldottam meg, hogy egy újabb interferenciajelet generáltam a detektált jelben, amelynek segítségével a jitter hatását a jelfeldolgozás után korrigáltam. A CEP zaj analízise megmutatta, hogy a zaj túlnyomórészt nagy frekvenciás komponensekből áll. Megállapítottam, hogy a MIR lézerrendszer CEP zajának további csökkentéséhez egy, a teljes ismétlési frekvencián működő, egylövéses CEP detektáló és stabilizáló rendszerre van szükség. [T1]

II. Kifejlesztettem az optikai elemek spektrális fázistolásának mérésére szolgáló, dual-band SRI-re keresztelt módszert, ami az ultragyors lézerforrás fundamentális és SH frekvenciatartományain párhuzamosan nyer ki fázisinformációt, kizárólag az SH frekvencia tartományon felvett interferogramokból. A módszert először egy hullámoptikai elméleti modellel és az ezen alapuló numerikus szimulációval vizsgáltam meg. Ezután a módszert kísérletileg demonstráltam a dual-band SRI elrendezéssel, a MIR lézerrendszerből származó 9 μJ energiájú impulzusok segítségével. Megmértem ismert optikai anyagok spektrális fázistolását, amivel igazoltam a módszert és az eszköz megfelelő működését. Továbbá bebizonyítottam, hogy egyetlen mért interferogram kétszer annyi információt hordoz, mint ammenyi a spektrális fázistolás teljes rekonstrukciójához szükséges mindkét frekvenciatartományon. Ezt különböző kiértékelési módszerek alkalmazásával és a kapott eredmények összehasonlításával igazoltam. A hullámoptikai modell alapján megvizsgáltam a dual-band SRI lehetséges továbbfejlesztési lehetőségeit, hogy több mint két frekvenciatartományt mérhessünk párhuzamosan. [T2]

III. Megterveztem és megépítettem egy vékonylemezes posztkompressziós elrendezést, hogy spektrálisan kiszélesítsem és időben kompresszáljam a MIR lézer impulzusait. Az 50 fs-os 100 kHz-es közép-infravörös lézerimpluzusokat 23 fs impulzusidőre sikerült rekompresszálni. Arra jutottam, hogy a YAG és a Si anyagból készült lemezek kombinációja ideális a spektrum szélesítésére a lineáris és nemlineáris optikai tulajdonságaiknak köszönhetően. Ezt kísérletileg

is bizonyítottam 2 mm vastag YAG és 1 mm vastag Si lemezzel, ahol az anyagokban lévő optikai intenzitást a lemezek fókuszáló tükörtől vett távolságának a változtatásával állítottam be. Az impulzusok összenyomása 23 fs-ra egy 3,3 mm vastag CaF_2 tömbben történt, amit két külön mérőeszközzel is bizonyítottam, az SH FROG-gal és a TIPTOE-val. Az impulzusok hosszú távú energia-, teljesítmény-, spektrum-, és CEP-stabilitását mértem 8 órán keresztül, ami bizonyította, hogy a rendszer kiválóan alkalmas felhasználói kísérletekre. [T3]

VI. Acknowledgement

In today's scientific world discoveries are rarely achieved by individuals, they are mostly the result of team efforts. The research my thesis is based upon was not an exception either, I could not have done it without the help and guidance of many talented individuals. It is difficult to express my gratitude to every single person who has helped me with my research, however in the following section I will try to do it justice.

First and foremost, I would like to thank my boss, supervisor, and mentor Bálint Kiss. He was the person who has guided me every step of the way, since I joined the MIR Group back in 2016. He gave me plenty of advice and provided answers to my countless questions.

Many thanks go to my advisor and supervisor Eric Cormier. Although he could not visit us as often as we have wished for, every time he showed up, he engulfed us with numerous ideas. Without his knowledge and experience this thesis would not have been possible.

I owe special thanks to all the current and former members of the MIR Group: Roland Flender, Szabolcs Tóth, Ludovít Haizer, who have helped me inside and outside the laboratory. Thank you all for all the insightful discussions, all the terrible jokes, and all the serious work we have performed together.

Furthermore, I am also very thankful to all my colleagues at ELI-ALPS, especially to Ádám Börzsönyi, Roland Nagymihály, and Tímea Tímár-Grósz, who gave their invaluable insights into my research, and helped me from the beginning, since I joined ELI.

Without a doubt, I am very grateful to my friends and family, who each in their own way supported and assisted me during this long and challenging task.

The work presented here could not have been concluded without the financial support of the ELI-ALPS project (GINOP-2.3.6-15-2015-00001), which is financed by the European Union and co-financed by the European Regional Development Fund.

VII. Own publications

VII.1. Publications related to the thesis

[T1] M. Kurucz, S. Toth, R. Flender, L. Haizer, B. Kiss, B. Persielle, E. Cormier, "Single-shot CEP drift measurement at arbitrary repetition rate based on dispersive Fourier transform", Optics Express 27(9), 13387-13399 (2019) DOI: 10.1364/OE.27.013387

[T2] M. Kurucz, R. Flender, T. Grosz, A. Borzsonyi, B. Kiss, "Simultaneous spectral phase shift characterization in two frequency bands", Optics Communication 500 127332 (2021). DOI: https://doi.org/10.1016/j.optcom.2021.127332

[T3] M. Kurucz, R. Flender, L. Haizer, R. S. Nagymihaly, W. Cho, K. T. Kim, S. Toth, E. Cormier, B. Kiss, "2.3-cycle mid-infrared pulses from hybrid thin-plate post-compression at 7 W average power", Optics Communication 472 126035 (2020) DOI: 10.1016/j.optcom.2020.126035

VII.2. Further scientific publications

[F1] S. Tóth, R. Flender, B. Kiss, M. Kurucz, A. Andrianov, L. Haizer, E. Cormier, K. Osvay, "Comparative study of an ultrafast, CEP-stable dual-channel mid-IR OPCPA system", Journal of the Optical Society of America B 36(12) 3538-3546 (2019). DOI: 10.1364/JOSAB.36.003538

[F2] R. Hollinger, D. Hoff, P. Wustelt, S. Skruszewicz, Y. Zhang, H. Kang, D. Würzler, T. Jungnickel, M. Dumergue, A. Nayak, R. Flender, L. Haizer, M. Kurucz, B. Kiss, S. Kühn, E. Cormier, C. Spielmann, G. G. Paulus, P. Tzallas, M. Kübel, "Carrier-envelope-phase measurement of few-cycle mid-infrared laser pulses using High Harmonic Generation in ZnO", Optics Express 28(5) 7314-7322 (2020). DOI: 10.1364/OE.383484

[F3] Y. Deng, Z. Zeng, P. Komm, Y. Zheng, W. Helml, X. Xie, Z. Filus, M. Dumergue, R. Flender, M. Kurucz, L. Haizer, B. Kiss, S. Kahaly, R. Li, G. Marcus, "Laser-induced inner-shell excitations through direct electron re-collision versus indirect collision", Optics Express 28(16) 23251-23265 (2020). DOI: 10.1364/OE.395927

[F4] C.T. Holló, K. Miháltz, M. Kurucz, A. Csorba, K. Kránitz, I. Kovács, Z.Z. Nagy, and G. Erdei. "Objective quantification and spatial mapping of cataract with a Shack-Hartmann wavefront sensor", Scientific Reports 10(1), 1-10 (2020). DOI: 10.1038/s41598-020-69321-3

[F5] C. Medina, D. Schomas, N. Rendler, M. Debatin, L. Ben Ltaief, Z. Filus, B. Farkas, R. Flender, L. Haizer, B. Kiss, M. Kurucz, B. Major, S. Toth, F. Stienkemeier, R. Moshammer, T. Pfeifer, S. R. Krishnan, A. Heidenreich, and M. Mudrich "Single-shot electron imaging of dopant-induced nanoplasmas", New Journal of Physics 23(5), 053011 (2021). DOI: 10.1088/1367-2630/abf7f9

[F6] F. Haniel, H. Schroeder, S. Kahaly, A. Nayak, M. Dumergue, S. Mondal, Z. Filus, R. Flender, M. Kurucz, L. Haizer, B. Kiss, D. Charalambidis, M. F Kling, P. Tzallas, and B. Bergues "Saturating Multiple Ionization in Intense Mid-Infrared Laser Fields", New Journal of Physics. 23 (2021) DOI: 10.1088/1367-2630/abf583

[F7] R. Flender, M. Kurucz, T. Grosz, A. Borzsonyi, U. Gimzevskis, A. Samalius, D. Hoff, and B. Kiss, "Dispersive mirror characterization and application for mid-infrared post-

compression", Journal of Optics 23(6), 065501 (2021). DOI: 10.1088/2040-8986/abf88e

[F8] M. Kübel, P. Wustelt, Y. Zhang, S. Skruszewicz, D. Hoff, D. Würzler, H. Kang, D. Zille, D. Adolph, G. G. Paulus, A. M. Sayler, M. Dumergue, A. Nayak, R. Flender, L. Haizer, M. Kurucz, B. Kiss, S. Kühn, B. Fetić, and D. B. Milošević, "High-Order Phase-Dependent Asymmetry in the Above-Threshold Ionization Plateau", Phys. Rev. Lett. 126(11), 113201 (2021). DOI: 10.1103/PhysRevLett.126.113201

VII.3. Conference presentations

(O) - oral presentation, (P) - poster presentation, **Bold*** - Presenting author.

[O1] **M. Kurucz***, Sz. Toth, R. Flender, L. Haizer, B. Kiss, B. Perseille, E. Cormier, "Dispersive Fourier transform based single-shot CEP drift measurement at arbitrary repetition rate", CLEO/Europe 2019, Munich, Germany, 23–27 June 2019. DOI: 10.1109/CLEOE-EQEC.2019.8871557

[O2] **Sz. Tóth***, R. S. Nagymihály, A. Andrianov, B. Kiss, R. Flender, M. Kurucz, L. Haizer, E. Cormier, K. Osvay, "Conceptual study of a 1 kHz 10 mJ-class mid-IR OPCPA system with thermal aspects", UFO, Bol, Croatia, 6–11 October 2019. URL: https://ultrafastoptics2019.engin.umich.edu/schedule/full-program/

[O3] **K. Osvay***, A. Borzsonyi, H. Cao, V. Chvykov, E. Cormier, R. Flender, P. Jojart, M. Kalashnikov, B. Kiss, M. Kurucz, N. Khodakovskiy, R. Lopez-Martens, R. S. Nagymihaly, V. Pajer, S. Toth, "Few cycle, phase controlled laser developments for ELI-ALPS", CLEO 2020, San Jose, California, USA, 11–15 May 2020. URL: www.cleoconference.org/

[O4] **A. Borzsonyi***, E. Cormier, R. Lopez-Martens, M. Kalashnikov, B. Kiss, P. Jojart, J. Csontos, S. Toth, N. Khodakovskiy, R. Nagymihaly, R. Flender, M. Kurucz, I. Seres, Z. Varallyay, K. Varju, G. Szabo, "Operation experiences and further developments of the few-cycle, high average power lasers of ELI-ALPS", ASSL, OSA Virtual Event, 13–16 October 2020, URL: https://www.osapublishing.org/conference.cfm?meetingid=1&yr=2020

[O5] **M. Kurucz***, R. Flender, L. Haizer, R. S. Nagymihaly, E. Cormier, B. Kiss, "Sub-two-cycle pulses in the mid-IR based on thin plate compression at high average power", HILAS, OSA Virtual Event, 16–20 November 2020. URL: https://www.osapublishing.org/conference.cfm?meetingid=119&yr=2020

[O6] **M. Kurucz***, S. Tóth, J. Csontos, B. Kiss, E. Cormier, "Every single-shot CEP drift detection for near-infrared lasers with modified TOUCAN method", HILAS, OSA Virtual Event, 16–20 November 2020. URL: https://www.osapublishing.org/conference.cfm?meetingid=119&yr=2020

[O7] **M. Kurucz***, R. Flender, T. Grosz, A. Borzsonyi, U. Gimzevskis, A. Samalius, D. Hoff, and B. Kiss "High resolution mid-IR spectrally resolved interferometry", SPIE Virtual Event, 17-23 April 2021. URL: https://spie.org/conferences and exhibitions/optics and optoelectronics/programme

[O8] **M. Kurucz***, S. Toth, J. Csontos, B. Kiss, and E. Cormier. "Every single-shot CEP drift detection for near-infrared lasers with a modified TOUCAN method", CLEO/Europe-EQEC, 21–25 June 2021. URL: https://www.cleoeurope.org/wp content/uploads/2021/06/cleo_2021_advance_programme.pdf

[P1] **M. Kurucz***, Á. Börzsönyi, m. Kovács, R. Nagymihály, K. Osvay, “Az SZTE TeWaTi femtoszekundumos lézerrendszer vivő-burkoló fáziscsúszásának mérése és stabilizálása,” Magyar Fizikus Vándorgyűlés, Szeged, Hungary, 24–27. August 2016. URL: http://titan.physx.u-szeged.hu/fizikus_vandorgyules_2016/node/6#poszterek

[P2] **M. Kurucz***, Sz. Tóth, R. Flender, L. Haizer, B. Kiss, B. Perseille, E. Cormier, “High-accuracy single-shot CEP noise measurement at arbitrary repetition rate”, UFO, Bol, Croatia, 6–11 October 2019. URL: https://ultrafastoptics2019.engin.umich.edu /schedule/full-program/

[P3] **M. Kurucz***, R. Flender, L. Haizer, B. Kiss, R. S. Nagymihaly, Sz. Tóth, E. Cormier, “Two-cycle pulses in the mid-IR based on hybrid thin plate compression at high average power”, ICEL, Prague, Czech Republic, 21–25. October 2019. URL: https://indico.eli-beams.eu/event/334/page/142-welcome

[P4] **M. Kurucz***, Sz. Tóth, R. Flender, L. Haizer, B. Kiss, B. Perseille, E. Cormier, “High-accuracy single-shot CEP noise measurement at arbitrary repetition rate”, ICEL, Prague, Czech Republic, 21–25 October 2019 URL: https://indico.eli-beams.eu/event/ 334/page/142-welcome

[P5] **M. Kurucz***, R. Flender, T. Grosz, A. Borzsonyi, U. Gimzevskis, A. Samalius, D. Hoff, and B. Kiss, “High resolution spectrally resolved interferometry in the mid IR”, CLEO/Europe-EQEC, 21–25 June 2021. URL: https://www.cleoeurope.org/ wp content/uploads/2021/06/cleo_2021_advance_programme.pdf

VIII. References

1. B. Wolter, M. G. Pullen, M. Baudisch, M. Sclafani, M. Hemmer, A. Senftleben, C. D. Schröter, J. Ullrich, R. Moshammer, and J. Biegert, "Strong-Field Physics with Mid-IR Fields," Phys. Rev. X **5**(2), 021034 (2015).
2. Z. Heiner, L. Wang, V. Petrov, and M. Mero, "Broadband vibrational sum-frequency generation spectrometer at 100 kHz in the 950-1750 cm−1 spectral range utilizing a LiGaS2 optical parametric amplifier," Opt. Express **27**(11), 15289–15297 (2019).
3. Q. Weng, "Thermal infrared remote sensing for urban climate and environmental studies: Methods, applications, and trends," ISPRS J. Photogramm. Remote Sens. **64**(4), 335–344 (2009).
4. R. I. Woodward, M. R. Majewski, D. D. Hudson, and S. D. Jackson, "Swept-wavelength mid-infrared fiber laser for real-time ammonia gas sensing," APL Photonics **4**(2), 020801 (2019).
5. N. A. Papadogiannis, B. Witzel, C. Kalpouzos, and D. Charalambidis, "Observation of Attosecond Light Localization in Higher Order Harmonic Generation," Phys Rev Lett **83**(21), 4289–4292 (1999).
6. M. Lewenstein, P. Balcou, M. Y. Ivanov, A. L’huillier, and P. B. Corkum, "Theory of high-harmonic generation by low-frequency laser fields," Phys. Rev. A **49**(3), 2117 (1994).
7. B. Shan and Z. Chang, "Dramatic extension of the high-order harmonic cutoff by using a long-wavelength driving field," Phys. Rev. A **65**(1), 011804 (2001).
8. A. D. Shiner, C. Trallero-Herrero, N. Kajumba, H.-C. Bandulet, D. Comtois, F. Légaré, M. Giguère, J. C. Kieffer, P. B. Corkum, and D. M. Villeneuve, "Wavelength scaling of high harmonic generation efficiency," Phys. Rev. Lett. **103**(7), 073902 (2009).
9. N. Thiré, R. Maksimenka, B. Kiss, C. Ferchaud, G. Gitzinger, T. Pinoteau, H. Jousselin, S. Jarosch, P. Bizouard, V. Di Pietro, E. Cormier, K. Osvay, and N. Forget, "Highly stable,

15 W, few-cycle, 65 mrad CEP-noise mid-IR OPCPA for statistical physics," Opt. Express **26**(21), 26907–26915 (2018).
10. Y. Deng, Z. Zeng, P. Komm, Y. Zheng, W. Helml, X. Xie, Z. Filus, M. Dumergue, R. Flender, and M. Kurucz, "Laser-induced inner-shell excitations through direct electron recollision versus indirect collision," Opt. Express **28**(16), 23251–23265 (2020).
11. C. Feng, J.-F. Hergott, P.-M. Paul, X. Chen, O. Tcherbakoff, M. Comte, O. Gobert, M. Reduzzi, F. Calegari, and C. Manzoni, "Complete analog control of the carrier-envelope-phase of a high-power laser amplifier," Opt. Express **21**(21), 25248–25256 (2013).
12. R. Hollinger, D. Hoff, P. Wustelt, S. Skruszewicz, Y. Zhang, H. Kang, D. Würzler, T. Jungnickel, M. Dumergue, A. Nayak, R. Flender, L. Haizer, M. Kurucz, B. Kiss, S. Kühn, E. Cormier, C. Spielmann, G. G. Paulus, P. Tzallas, and M. Kübel, "Carrier-envelope-phase measurement of few-cycle mid-infrared laser pulses using high harmonic generation in ZnO," Opt. Express **28**(5), 7314–7322 (2020).
13. M. Kübel, P. Wustelt, Y. Zhang, S. Skruszewicz, D. Hoff, D. Würzler, H. Kang, D. Zille, D. Adolph, G. G. Paulus, A. M. Sayler, M. Dumergue, A. Nayak, R. Flender, L. Haizer, M. Kurucz, B. Kiss, S. Kühn, B. Fetić, and D. B. Milošević, "High-Order Phase-Dependent Asymmetry in the Above-Threshold Ionization Plateau," Phys. Rev. Lett. **126**(11), 113201 (2021).
14. W. Herschel, "XIV. Experiments on the refrangibility of the invisible rays of the sun," Philos. Trans. R. Soc. Lond. (90), 284–292 (1800).
15. P. R. Griffiths and J. A. De Haseth, *Fourier Transform Infrared Spectrometry* (John Wiley & Sons, 2007), **171**.
16. B. D. Guenther, *Modern Optics, Chapter 1* (OUP Oxford, 2015).
17. J.-C. Diels and W. Rudolph, *Ultrashort Laser Pulse Phenomena* (Elsevier, 2006).
18. B. D. Guenther, *Modern Optics, Chapter 6* (OUP Oxford, 2015).
19. "Multimode and Pulsed Lasing," in *Laser Physics* (John Wiley & Sons, Ltd, 2010), pp. 229–268.
20. H. R. Telle, G. Steinmeyer, A. E. Dunlop, J. Stenger, D. H. Sutter, and U. Keller, "Carrier-envelope offset phase control: A novel concept for absolute optical frequency measurement and ultrashort pulse generation," Appl. Phys. B **69**(4), 327–332 (1999).
21. E. Hecht and A. Zajac, *Optics, Chapter 3*, 4th ed. (Addison-Wesley, 1987).
22. S. Kühn, M. Dumergue, S. Kahaly, S. Mondal, M. Füle, T. Csizmadia, B. Farkas, B. Major, Z. Várallyay, and E. Cormier, "The ELI-ALPS facility: the next generation of attosecond sources," J. Phys. B At. Mol. Opt. Phys. **50**(13), 132002 (2017).
23. A. Weiner, *Ultrafast Optics* (John Wiley & Sons, 2011), **72**.
24. M. Bass, *Handbook of Optics, Volume IV: Optical Properties of Materials, Nonlinear Optics, Quantum Optics, Chapter 5* (McGraw-Hill, 2009).
25. A. Rockett, *The Materials Science of Semiconductors, Chapter The Physics of Solids* (Springer Science & Business Media, 2007).
26. N. K. Hon, R. Soref, and B. Jalali, "The third-order nonlinear optical coefficients of Si, Ge, and Si1− x Ge x in the midwave and longwave infrared," J. Appl. Phys. **110**(1), 9 (2011).
27. D. Ehrt, "Phosphate and fluoride phosphate optical glasses—properties, structure and applications," Phys. Chem. Glas.-Eur. J. Glass Sci. Technol. Part B **56**(6), 217–234 (2015).
28. J. T. Kiehl and K. E. Trenberth, "Earth's annual global mean energy budget," Bull. Am. Meteorol. Soc. **78**(2), 197–208 (1997).
29. "SCHOTT Zemax catalog 2017-01-20b," http://www.schott.com.
30. P. A. Franken, A. E. Hill, C. W. Peters, and G. Weinreich, "Generation of Optical Harmonics," Phys Rev Lett **7**(4), 118–119 (1961).

31. S. Guha and L. P. Gonzalez, *Laser Beam Propagation in Nonlinear Optical Media, Chapter 2* (CRC Press, 2013).
32. R. W. Boyd, *Nonlinear Optics, Chapter 1* (Academic press, 2020).
33. D. F. Walls and G. J. Milburn, *Quantum Optics* (Springer Science & Business Media, 2007).
34. G. M. Gale, M. Cavallari, T. J. Driscoll, and F. Hache, "Sub-20-fs tunable pulses in the visible from an 82-MHz optical parametric oscillator," Opt. Lett. **20**(14), 1562–1564 (1995).
35. A. Shirakawa, I. Sakane, and T. Kobayashi, "Pulse-front-matched optical parametric amplification for sub-10-fs pulse generation tunable in the visible and near infrared," Opt. Lett. **23**(16), 1292–1294 (1998).
36. T. Kobayashi and A. Shirakawa, "Tunable visible and near-infrared pulse generator in a 5 fs regime," Appl. Phys. B **70**(1), S239–S246 (2000).
37. R. C. Powell, *Symmetry, Group Theory, and the Physical Properties of Crystals* (Springer, 2010), **172**.
38. R. L. Sutherland, *Handbook of Nonlinear Optics, Chapter 6* (CRC press, 2003).
39. M. Sheik-Bahae, J. Wang, and E. W. Van Stryland, "Nondegenerate optical Kerr effect in semiconductors," IEEE J. Quantum Electron. **30**(2), 249–255 (1994).
40. M. Sheik-Bahae, D. J. Hagan, and E. W. Van Stryland, "Dispersion and band-gap scaling of the electronic Kerr effect in solids associated with two-photon absorption," Phys. Rev. Lett. **65**(1), 96 (1990).
41. M. Sheik-Bahae, D. C. Hutchings, D. J. Hagan, and E. W. Van Stryland, *Dispersion of Bound Electronic Nonlinear Refraction in Solids. JQE* (QE-27, 1991).
42. A. Baltuška, T. Fuji, and T. Kobayashi, "Controlling the Carrier-Envelope Phase of Ultrashort Light Pulses with Optical Parametric Amplifiers," Phys. Rev. Lett. **88**(13), 133901 (2002).
43. M. Kakehata, H. Takada, Y. Kobayashi, K. Torizuka, Y. Fujihira, T. Homma, and H. Takahashi, "Single-shot measurement of carrier-envelope phase changes by spectral interferometry," Opt. Lett. **26**(18), 1436–1438 (2001).
44. R. Thomson, C. Leburn, and D. Reid, *Ultrafast Nonlinear Optics* (Springer, 2013).
45. C. Sáinz, P. Jourdian, R. Escalona, and J. Calatroni, "Real time interferometric measurements of dispersion curves," Opt. Commun. **110**(3), 381–390 (1994).
46. F. Koch, S. V. Chernikov, and J. R. Taylor, "Dispersion measurement in optical fibres over the entire spectral range from 1.1 μm to 1.7 μm," Opt. Commun. **175**(1), 209–213 (2000).
47. J. Jasapara, T. H. Her, R. Bise, R. Windeler, and D. J. DiGiovanni, "Group-velocity dispersion measurements in a photonic bandgap fiber," JOSA B **20**(8), 1611–1615 (2003).
48. L. Lepetit, G. Chériaux, and M. Joffre, "Linear techniques of phase measurement by femtosecond spectral interferometry for applications in spectroscopy," J. Opt. Soc. Am. B **12**(12), 2467–2474 (1995).
49. C. Dorrer, N. Belabas, J.-P. Likforman, and M. Joffre, "Spectral resolution and sampling issues in Fourier-transform spectral interferometry," J Opt Soc Am B **17**(10), 1795–1802 (2000).
50. R. Flender, M. Kurucz, T. Grosz, A. Borzsonyi, U. Gimzevskis, A. Samalius, D. Hoff, and B. Kiss, "Dispersive mirror characterization and application for mid-infrared post-compression," J. Opt. **23**(6), 065501 (2021).
51. A. Baltuška, Th. Udem, M. Uiberacker, M. Hentschel, E. Goulielmakis, Ch. Gohle, R. Holzwarth, V. S. Yakovlev, A. Scrinzi, T. W. Hänsch, and F. Krausz, "Attosecond control of electronic processes by intense light fields," Nature **421**, 611–615 (2003).
52. F. Krausz and M. Ivanov, "Attosecond physics," Rev Mod Phys **81**(1), 163–234 (2009).

53. G. Sansone, F. Calegari, and M. Nisoli, "Attosecond technology and science," IEEE J. Sel. Top. Quantum Electron. **18**(1), 507–519 (2011).
54. F. Calegari, G. Sansone, S. Stagira, C. Vozzi, and M. Nisoli, "Advances in attosecond science," J. Phys. B At. Mol. Opt. Phys. **49**(6), 062001 (2016).
55. F. Lépine, M. Y. Ivanov, and M. J. Vrakking, "Attosecond molecular dynamics: fact or fiction?," Nat. Photonics **8**(3), 195 (2014).
56. A. Mikkelsen, J. Schwenke, T. Fordell, G. Luo, K. Klünder, E. Hilner, N. Anttu, A. A. Zakharov, E. Lundgren, and J. Mauritsson, "Photoemission electron microscopy using extreme ultraviolet attosecond pulse trains," Rev. Sci. Instrum. **80**(12), 123703 (2009).
57. N. Tsatrafyllis, S. Kühn, M. Dumergue, P. Foldi, S. Kahaly, E. Cormier, I. A. Gonoskov, B. Kiss, K. Varju, S. Varro, and P. Tzallas, "Quantum Optical Signatures in a Strong Laser Pulse after Interaction with Semiconductors," Phys Rev Lett **122**(19), 193602 (2019).
58. M. Krebs, S. Hädrich, S. Demmler, J. Rothhardt, A. Zaïr, L. Chipperfield, J. Limpert, and A. Tünnermann, "Towards isolated attosecond pulses at megahertz repetition rates," Nat. Photonics **7**(7), 555 (2013).
59. M. Reduzzi, P. Carpeggiani, S. Kühn, F. Calegari, M. Nisoli, S. Stagira, C. Vozzi, P. Dombi, S. Kahaly, P. Tzallas, D. Charalambidis, K. Varju, K. Osvay, and G. Sansone, "Advances in high-order harmonic generation sources for time-resolved investigations," J. Electron Spectrosc. Relat. Phenom. **204**, 257–268 (2015).
60. F. Lücking, A. Assion, A. Apolonski, F. Krausz, and G. Steinmeyer, "Long-term carrier-envelope-phase-stable few-cycle pulses by use of the feed-forward method," Opt. Lett. **37**(11), 2076–2078 (2012).
61. S. Sartania, Z. Cheng, M. Lenzner, G. Tempea, C. Spielmann, F. Krausz, and K. Ferencz, "Generation of 0.1-TW 5-fs optical pulses at a 1-kHz repetition rate," Opt Lett **22**(20), 1562–1564 (1997).
62. A. Baltuska, M. Uiberacker, E. Goulielmakis, R. Kienberger, V. S. Yakovlev, T. Udem, T. W. Hansch, and F. Krausz, "Phase-controlled amplification of few-cycle laser pulses," IEEE J. Sel. Top. Quantum Electron. **9**(4), 972–989 (2003).
63. M. Mehendale, S. A. Mitchell, J.-P. Likforman, D. M. Villeneuve, and P. B. Corkum, "Method for single-shot measurement of the carrier envelope phase of a few-cycle laser pulse," Opt Lett **25**(22), 1672–1674 (2000).
64. E. Cormier and P. Lambropoulos, "Effect of the initial phase of the field in ionization by ultrashort laser pulses," Eur. Phys. J. - At. Mol. Opt. Plasma Phys. **2**(1), 15–20 (1998).
65. T. Wittmann, B. Horvath, W. Helml, M. G. Schätzel, X. Gu, A. L. Cavalieri, G. G. Paulus, and R. Kienberger, "Single-shot carrier–envelope phase measurement of few-cycle laser pulses," Nat. Phys. **5**, 357–362 (2009).
66. A. M. Sayler, T. Rathje, W. Müller, K. Rühle, R. Kienberger, and G. G. Paulus, "Precise, real-time, every-single-shot, carrier-envelope phase measurement of ultrashort laser pulses," Opt. Lett. **36**(1), 1–3 (2011).
67. D. Hoff, F. J. Furch, T. Witting, K. Rühle, D. Adolph, A. M. Sayler, M. J. J. Vrakking, G. G. Paulus, and C. P. Schulz, "Continuous every-single-shot carrier-envelope phase measurement and control at 100 kHz," Opt. Lett. **43**(16), 3850–3853 (2018).
68. D. A. Debrah, G. A. Stewart, G. Basnayake, J. W. Tisch, S. K. Lee, and W. Li, "Direct in-situ single-shot measurements of the absolute carrier-envelope phases of ultrashort pulses," Opt. Lett. **44**(14), 3582–3585 (2019).
69. M. Kubullek, Z. Wang, K. von der Brelje, D. Zimin, P. Rosenberger, J. Schötz, M. Neuhaus, S. Sederberg, A. Staudte, N. Karpowicz, M. F. Kling, and B. Bergues, "Single-shot carrier–envelope-phase measurement in ambient air," Optica **7**(1), 35–39 (2020).
70. C. W. Rudy, "Mid-IR Lasers: Power and pulse capability ramp up for mid-IR lasers," Laser Focus World **50**(5), 63–66 (2014).

71. J. Ma, Z. Qin, G. Xie, L. Qian, and D. Tang, "Review of mid-infrared mode-locked laser sources in the 2.0 μ m–3.5 μ m spectral region," Appl. Phys. Rev. **6**(2), 021317 (2019).
72. A. Godard, "Infrared (2–12 μm) solid-state laser sources: a review," Comptes Rendus Phys. **8**(10), 1100–1128 (2007).
73. J. Hillbrand, M. Beiser, A. M. Andrews, H. Detz, R. Weih, A. Schade, S. Höfling, G. Strasser, and B. Schwarz, "Picosecond pulses from a mid-infrared interband cascade laser," Optica **6**(10), 1334–1337 (2019).
74. X. Zhu, G. Zhu, C. Wei, L. V. Kotov, J. Wang, M. Tong, R. A. Norwood, and N. Peyghambarian, "Pulsed fluoride fiber lasers at 3 μm," JOSA B **34**(3), A15–A28 (2017).
75. Y. Wang, F. Jobin, S. Duval, V. Fortin, P. Laporta, M. Bernier, G. Galzerano, and R. Vallée, "Ultrafast Dy3+:fluoride fiber laser beyond 3 μm," Opt. Lett. **44**(2), 395–398 (2019).
76. I. T. Sorokina, "Cr2+-doped II–VI materials for lasers and nonlinear optics," Opt. Mater. **26**(4), 395–412 (2004).
77. Y. Wang, T. T. Fernandez, N. Coluccelli, A. Gambetta, P. Laporta, and G. Galzerano, "47-fs Kerr-lens mode-locked Cr: ZnSe laser with high spectral purity," Opt. Express **25**(21), 25193–25200 (2017).
78. M. N. Cizmeciyan, J. W. Kim, S. Bae, B. H. Hong, F. Rotermund, and A. Sennaroglu, "Graphene mode-locked femtosecond Cr: ZnSe laser at 2500 nm," Opt. Lett. **38**(3), 341–343 (2013).
79. S. B. Mirov, I. S. Moskalev, S. Vasilyev, V. Smolski, V. V. Fedorov, D. Martyshkin, J. Peppers, M. Mirov, A. Dergachev, and V. Gapontsev, "Frontiers of mid-IR lasers based on transition metal doped chalcogenides," IEEE J. Sel. Top. Quantum Electron. **24**(5), 1–29 (2018).
80. A. V. Pushkin, E. A. Migal, S. Tokita, Y. V. Korostelin, and F. V. Potemkin, "Femtosecond graphene mode-locked Fe: ZnSe laser at 4.4 μm," Opt. Lett. **45**(3), 738–741 (2020).
81. S. Tóth, R. Flender, B. Kiss, M. Kurucz, A. Andrianov, R. S. Nagymihaly, L. Haizer, E. Cormier, and K. Osvay, "Comparative study of an ultrafast, CEP-stable, dual-channel mid-IR OPCPA system," J. Opt. Soc. Am. B **36**(12), 3538–3546 (2019).
82. A. Vaupel, N. Bodnar, B. Webb, L. Shah, and M. C. Richardson, "Concepts, performance review, and prospects of table-top, few-cycle optical parametric chirped-pulse amplification," Opt. Eng. **53**(5), 051507 (2013).
83. K.-H. Hong, C.-J. Lai, J. P. Siqueira, P. Krogen, J. Moses, C.-L. Chang, G. J. Stein, L. E. Zapata, and F. X. Kärtner, "Multi-mJ, kHz, 2.1 μm optical parametric chirped-pulse amplifier and high-flux soft x-ray high-harmonic generation," Opt. Lett. **39**(11), 3145–3148 (2014).
84. F. Batysta, R. Antipenkov, J. Novák, J. T. Green, J. A. Naylon, J. Horáček, M. Horáček, Z. Hubka, R. Boge, T. Mazanec, B. Himmel, P. Bakule, and B. Rus, "Broadband OPCPA system with 11 mJ output at 1 kHz, compressible to 12 fs," Opt. Express **24**(16), 17843–17848 (2016).
85. S. Toth, T. Stanislauskas, I. Balciunas, R. Budriunas, J. Adamonis, R. Danilevicius, K. Viskontas, D. Lengvinas, G. Veitas, and D. Gadonas, "SYLOS lasers–the frontier of few-cycle, multi-TW, kHz lasers for ultrafast applications at extreme light infrastructure attosecond light pulse source," J. Phys. Photonics **2**(4), 045003 (2020).
86. D. Strickland and G. Mourou, "Compression of amplified chirped optical pulses," Opt. Commun. **56**(3), 219–221 (1985).
87. R. Riedel, J. Rothhardt, K. Beil, B. Gronloh, A. Klenke, H. Höppner, M. Schulz, U. Teubner, C. Kränkel, and J. Limpert, "Thermal properties of borate crystals for high power

optical parametric chirped-pulse amplification," Opt. Express **22**(15), 17607–17619 (2014).
88. B. W. Mayer, C. R. Phillips, L. Gallmann, and U. Keller, "Mid-infrared pulse generation via achromatic quasi-phase-matched OPCPA," Opt. Express **22**(17), 20798–20808 (2014).
89. M. Baudisch, B. Wolter, M. Pullen, M. Hemmer, and J. Biegert, "High power multi-color OPCPA source with simultaneous femtosecond deep-UV to mid-IR outputs," Opt. Lett. **41**(15), 3583–3586 (2016).
90. U. Elu, M. Baudisch, H. Pires, F. Tani, M. H. Frosz, F. Köttig, A. Ermolov, P. St.J. Russell, and J. Biegert, "High average power and single-cycle pulses from a mid-IR optical parametric chirped pulse amplifier," Optica **4**(9), 1024–1029 (2017).
91. G. Fan, T. Balčiūnas, T. Kanai, T. Flöry, G. Andriukaitis, B. E. Schmidt, F. Légaré, and A. Baltuška, "Hollow-core-waveguide compression of multi-millijoule CEP-stable 3.2 μm pulses," Optica **3**(12), 1308–1311 (2016).
92. P. Wang, Y. Li, W. Li, H. Su, B. Shao, S. Li, C. Wang, D. Wang, R. Zhao, Y. Peng, Y. Leng, R. Li, and Z. Xu, "2.6 mJ/100 Hz CEP-stable near-single-cycle 4 μm laser based on OPCPA and hollow-core fiber compression," Opt. Lett. **43**(9), 2197–2200 (2018).
93. K. Murari, G. J. Stein, H. Cankaya, B. Debord, F. Gérôme, G. Cirmi, O. D. Mücke, P. Li, A. Ruehl, I. Hartl, K.-H. Hong, F. Benabid, and F. X. Kärtner, "Kagome-fiber-based pulse compression of mid-infrared picosecond pulses from a Ho:YLF amplifier," Optica **3**(8), 816–822 (2016).
94. J. Schulte, T. Sartorius, J. Weitenberg, A. Vernaleken, and P. Russbueldt, "Nonlinear pulse compression in a multi-pass cell," Opt. Lett. **41**(19), 4511–4514 (2016).
95. G. Jargot, N. Daher, L. Lavenu, X. Delen, N. Forget, M. Hanna, and P. Georges, "Self-compression in a multipass cell," Opt. Lett. **43**(22), 5643–5646 (2018).
96. M. Hanna, X. Délen, L. Lavenu, F. Guichard, Y. Zaouter, F. Druon, and P. Georges, "Nonlinear temporal compression in multipass cells: theory," J. Opt. Soc. Am. B **34**(7), 1340–1347 (2017).
97. M. Ueffing, S. Reiger, M. Kaumanns, V. Pervak, M. Trubetskov, T. Nubbemeyer, and F. Krausz, "Nonlinear pulse compression in a gas-filled multipass cell," Opt. Lett. **43**(9), 2070–2073 (2018).
98. M. Hemmer, M. Baudisch, A. Thai, A. Couairon, and J. Biegert, "Self-compression to sub-3-cycle duration of mid-infrared optical pulses in dielectrics," Opt. Express **21**(23), 28095–28102 (2013).
99. V. Shumakova, P. Malevich, S. Ališauskas, A. Voronin, A. M. Zheltikov, D. Faccio, D. Kartashov, A. Baltuška, and A. Pugžlys, "Multi-millijoule few-cycle mid-infrared pulses through nonlinear self-compression in bulk," Nat. Commun. **7**, 12877 (2016).
100. F. Lu, P. Xia, Y. Matsumoto, T. Kanai, N. Ishii, and J. Itatani, "Generation of sub-two-cycle CEP-stable optical pulses at 3.5 μm from a KTA-based optical parametric amplifier with multiple-plate compression," Opt. Lett. **43**(11), 2720–2723 (2018).
101. A. Marcinkevičiūtė, N. Garejev, R. Šuminas, G. Tamošauskas, and A. Dubietis, "A compact, self-compression-based sub-3 optical cycle source in the 3-4 um spectral range," J. Opt. **19**(10), 105505 (2017).
102. J. Schulte, T. Sartorius, J. Weitenberg, A. Vernaleken, and P. Russbueldt, "Nonlinear pulse compression in a multi-pass cell," Opt. Lett. **41**(19), 4511–4514 (2016).
103. G. Jargot, N. Daher, L. Lavenu, X. Delen, N. Forget, M. Hanna, and P. Georges, "Self-compression in a multipass cell," Opt. Lett. **43**(22), 5643–5646 (2018).
104. P. Tournois, "Acousto-optic programmable dispersive filter for adaptive compensation of group delay time dispersion in laser systems," Opt. Commun. **140**(4), 245–249 (1997).

105. M. Baudisch, M. Hemmer, H. Pires, and J. Biegert, "Performance of MgO:PPLN, KTA, and KNbO3 for mid-wave infrared broadband parametric amplification at high average power," Opt. Lett. **39**(20), 5802–5805 (2014).
106. F. Lücking, V. Crozatier, N. Forget, A. Assion, and F. Krausz, "Approaching the limits of carrier-envelope phase stability in a millijoule-class amplifier," Opt. Lett. **39**(13), 3884–3887 (2014).
107. K. Zhao, H. Zhong, P. Yuan, G. Xie, J. Wang, J. Ma, and L. Qian, "Generation of 120 GW mid-infrared pulses from a widely tunable noncollinear optical parametric amplifier," Opt. Lett. **38**(13), 2159–2161 (2013).
108. A. V. Mitrofanov, A. A. Voronin, D. A. Sidorov-Biryukov, S. I. Mitryukovsky, A. B. Fedotov, E. E. Serebryannikov, D. V. Meshchankin, V. Shumakova, S. Ališauskas, and A. Pugžlys, "Subterawatt few-cycle mid-infrared pulses from a single filament," Optica **3**(3), 299–302 (2016).
109. M. Bridger, O. A. Naranjo-Montoya, A. Tarasevitch, and U. Bovensiepen, "Towards high power broad-band OPCPA at 3000 nm," Opt. Express **27**(22), 31330–31337 (2019).
110. P. Rigaud, A. Van de Walle, M. Hanna, N. Forget, F. Guichard, Y. Zaouter, K. Guesmi, F. Druon, and P. Georges, "Supercontinuum-seeded few-cycle mid-infrared OPCPA system," Opt. Express **24**(23), 26494–26502 (2016).
111. T. Kanai, Y. Lee, M. Seo, and D. E. Kim, "Supercontinuum-seeded, carrier-envelope, phase-stable, 4.5-W, 3.8-μm, 6-cycle, KTA optical parametric amplifier driven by a 1.4-ps Yb: YAG thin-disk amplifier for nonperturbative spectroscopy in solids," JOSA B **36**(9), 2407–2413 (2019).
112. M. Mero, Z. Heiner, V. Petrov, H. Rottke, F. Branchi, G. M. Thomas, and M. J. Vrakking, "43 W, 1.55 μm and 12.5 W, 3.1 μm dual-beam, sub-10 cycle, 100 kHz optical parametric chirped pulse amplifier," Opt. Lett. **43**(21), 5246–5249 (2018).
113. M. Bass, *Handbook of Optics: Volume Ii-Design, Fabrication, and Testing; Sources and Detectors; Radiometry and Photometry, Chapter 24* (McGraw-Hill Education, 2010).
114. "Pyrocam IIIHR Beam Profiling Camera," https://www.ophiropt.com/.
115. "Mozza Mid-IR spectrometer," https://fastlite.com/produits/mozza-mir-spectrometer/.
116. G. Gitzinger, V. Crozatier, R. Maksimenka, S. Grabielle, N. Forget, S. Alisauskas, A. Pugzlys, A. Baltuska, B. Monoszlai, C. Vicario, and C. P. Hauri, "Multi-octave acousto-optic spectrum analyzer for mid-infrared pulsed sources," in *CLEO: 2014*, OSA Technical Digest (Online) (Optical Society of America, 2014), p. STh1N.5.
117. Y. C. Tong, L. Y. Chan, and H. K. Tsang, "Fibre dispersion or pulse spectrum measurement using a sampling oscilloscope," Electron. Lett. **33**(11), 983–985 (1997).
118. K. Goda and B. Jalali, "Dispersive Fourier transformation for fast continuous single-shot measurements," Nat. Photonics **7**, 102–112 (2013).
119. "R&S®RTO2000 Oscilloscope User Manual," https://www.rohde-schwarz.com/webhelp/rto_html_usermanual_en/RTO_HTML_UserManual_en.htm.
120. M. Kurucz, S. Tóth, R. Flender, L. Haizer, B. Kiss, B. Persielle, and E. Cormier, "Single-shot CEP drift measurement at arbitrary repetition rate based on dispersive Fourier transform," Opt. Express **27**(9), 13387–13399 (2019).
121. T. Kato, Y. Koyano, and M. Nishimura, "Temperature dependence of chromatic dispersion in various types of optical fiber," Opt. Lett. **25**(16), 1156–1158 (2000).
122. R. G. Lyons, *Understanding Digital Signal Processing*, II (Prentice Hall PTR, 2004).
123. N. I. Fisher and A. J. Lee, "A correlation coefficient for circular data," Biometrika **70**(2), 327–332 (1983).
124. S. R. Jammalamadaka and A. Sengupta, *Topics in Circular Statistics* (World Scientific Pub Co Inc, 2001).

125. F. Lücking, "Carrier-envelope phase control for the advancement of attosecond pulse generation," Ludwig-Maximilians-Universität (2014).
126. R. Flender, K. Sarosi, E. Petracs, A. Borzsonyi, and V. Chikan, "Control of THz field waveform emitted from air plasma by chirping two-color laser pulses," Opt. Commun. **436**, 222–226 (2019).
127. J. Dai, N. Karpowicz, and X.-C. Zhang, "Coherent Polarization Control of Terahertz Waves Generated from Two-Color Laser-Induced Gas Plasma," Phys Rev Lett **103**(2), 023001 (2009).
128. E. Cormier and M. Lewenstein, "Optimizing the efficiency in high order harmonic generation optimization by two-color fields," Eur. Phys. J. - At. Mol. Opt. Plasma Phys. **12**(2), 227–233 (2000).
129. D. B. Milošević and W. Sandner, "Extreme-ultraviolet harmonic generation near 13 nm with a two-color elliptically polarized laser field," Opt. Lett. **25**(20), 1532–1534 (2000).
130. W. S. Rodney and I. H. Malitson, "Refraction and Dispersion of Thallium Bromide Iodide," J. Opt. Soc. Am. **46**(11), 956–961 (1956).
131. T. Grósz, M. Horváth, and A. P. Kovács, "Complete dispersion characterization of microstructured optical fibers from a single interferogram using the windowed Fourier-ridges algorithm," Opt. Express **25**(23), 28459–28468 (2017).
132. D. K. Gifford, B. J. Soller, M. S. Wolfe, and M. E. Froggatt, "Optical vector network analyzer for single-scan measurements of loss, group delay, and polarization mode dispersion," Appl. Opt. **44**(34), 7282–7286 (2005).
133. S. K. Debnath, M. P. Kothiyal, and S.-W. Kim, "Evaluation of spectral phase in spectrally resolved white-light interferometry: Comparative study of single-frame techniques," Opt. Lasers Eng. **47**(11), 1125–1130 (2009).
134. D. E. Zelmon, D. L. Small, and R. Page, "Refractive-index measurements of undoped yttrium aluminum garnet from 0.4 to 5.0 μm," Appl. Opt. **37**(21), 4933–4935 (1998).
135. H. H. Li, "Refractive index of alkaline earth halides and its wavelength and temperature derivatives," J. Phys. Chem. Ref. Data **9**(1), 161–290 (1980).
136. I. H. Malitson, "A Redetermination of Some Optical Properties of Calcium Fluoride," Appl. Opt. **2**(11), 1103–1107 (1963).
137. M. Hemmer, M. Baudisch, A. Thai, A. Couairon, and J. Biegert, "Self-compression to sub-3-cycle duration of mid-infrared optical pulses in dielectrics," Opt. Express **21**(23), 28095–28102 (2013).
138. A. Marcinkevičiūtė, N. Garejev, R. Šuminas, G. Tamošauskas, and A. Dubietis, "A compact, self-compression-based sub-3 optical cycle source in the 3-4 um spectral range," J. Opt. **19**(10), 105505 (2017).
139. M. Kurucz, R. Flender, L. Haizer, R. S. Nagymihaly, W. Cho, K. T. Kim, S. Toth, E. Cormier, and B. Kiss, "2.3-cycle mid-infrared pulses from hybrid thin-plate post-compression at 7 W average power," Opt. Commun. **472**, 126035 (2020).
140. R. Trebino, K. W. DeLong, D. N. Fittinghoff, J. N. Sweetser, M. A. Krumbügel, B. A. Richman, and D. J. Kane, "Measuring ultrashort laser pulses in the time-frequency domain using frequency-resolved optical gating," Rev. Sci. Instrum. **68**(9), 3277–3295 (1997).
141. S. B. Park, K. Kim, W. Cho, S. I. Hwang, I. Ivanov, C. H. Nam, and K. T. Kim, "Direct sampling of a light wave in air," Optica **5**(4), 402–408 (2018).
142. W. Cho, S. I. Hwang, C. H. Nam, M. R. Bionta, P. Lassonde, B. E. Schmidt, H. Ibrahim, F. Légaré, and K. T. Kim, "Temporal characterization of femtosecond laser pulses using tunneling ionization in the UV, visible, and mid-IR ranges," Sci. Rep. **9**(1), 16067 (2019).
143. "COMSOL Multiphysics," https://www.comsol.com/.

144. A. Marcinkevičiūtė, V. Jukna, R. Šuminas, N. Garejev, G. Tamošauskas, and A. Dubietis, "Femtosecond filamentation and supercontinuum generation in bulk silicon," Opt. Lett. **44**(6), 1343–1346 (2019).
145. R. K. W. Lau, M. R. E. Lamont, Y. Okawachi, and A. L. Gaeta, "Effects of multiphoton absorption on parametric comb generation in silicon microresonators," Opt. Lett. **40**(12), 2778–2781 (2015).
146. "Crystran Ltd," Crystran Ltd.